Mechanical Design and Analysis of Implantable Components for a Retinal Prosthesis

by

Joshua D. Moss

B.S., Biomedical Engineering (1997)

Case Western Reserve University

Submitted to the Department of Mechanical Engineering
in Partial Fulfillment of the Requirements for the Degree of

Master of Science in Mechanical Engineering

at the

Massachusetts Institute of Technology

June 1999

© 1999 Massachusetts Institute of Technology
All rights reserved

ARCHIVES
MASSACHUSETTS INSTITUTE OF TECHNOLOGY
JUL 1 2 1999
LIBRARIES

Signature of Author.....
Department of Mechanical Engineering
May 24, 1999

Certified By.....
John L. Wyatt, Jr.
Professor of Electrical Engineering and Computer Science
Thesis Supervisor

Certified By.....
Derek Rowell
Professor of Mechanical Engineering
Departmental Reader

Accepted By.....
Ain A. Sonin
Chairman, Department Committee on Graduate Students

Mechanical Design and Analysis of Implantable Components for a Retinal Prosthesis

by

Joshua D. Moss

Submitted to the Department of Mechanical Engineering
on May 24, 1999 in Partial Fulfillment of the
Requirements for the Degree of Master of Science in
Mechanical Engineering

ABSTRACT

The success of a retinal prosthesis in restoring vision to blind patients will be dependent on its long term viability when implanted in the eye. This thesis addresses mechanical aspects relating to the biocompatibility of the device and its ability to survive in a saline environment.

Chronic testing of a working prosthesis requires hermetic encapsulation of all implanted electronics; any direct contact with the fluid in the eye will damage the circuitry and render the device ineffectual. A metal housing, which has provided effective protection of other prostheses, would interfere with light transmission from the external source and is therefore impractical. Encapsulation of the electronics in transparent polymers is a potential alternative. Our current prosthesis design requires both a polyimide electrode array and a return wire to penetrate the protective capsule. Therefore, a technique for evaluating the hermetic encapsulation of these components was designed and tested. Simple, expendable models of the prosthesis were developed and used to test silicone as an encapsulant. In a 60 day soak test, all prosthesis models failed within three days, while completely encapsulated control models exhibited no current leakage. For the silicone application methods and implant materials currently being used, silicone is not an effective encapsulant.

The majority of the implanted electronics, including a photodiode array, will be supported in the front of the eye by an intraocular support structure. Early designs of this structure were based on the structure of commercially available intraocular lenses commonly used in cataract surgeries. Using stereolithography, a rapid prototyping technique, this structure was redesigned based on mechanical and surgical criteria. The existing haptic system was modified to improve stability, and arrangement of the photodiode array on the structure was optimized. In addition, the structure itself was simplified for fabrication from biocompatible materials. Stability of the entire structure relative to the eye and of the photodiode array relative to the structure was analyzed using finite element methods. The final design, when injection molded from silicone rubber, was tested surgically by implantation into animal eyes. The surgery was successful, and the basic design will be used in future tests.

Thesis Supervisor: John L. Wyatt, Jr.
Title: Professor of Electrical Engineering and Computer Science

Acknowledgements

I would like to acknowledge many more people than can possibly be listed here; the support that they have provided me has been invaluable. However, a select few deserve special recognition. Without them, completion of this thesis would not have been possible.

Thanks go first and foremost to my advisors, Prof. John Wyatt and Dr. Joseph Rizzo. Prof. Wyatt offered helpful insights on the encapsulation testing setup and very constructive feedback on this manuscript. He has also been a consistent source of motivation and encouragement regarding my plans, both for the thesis and my future. Dr. Rizzo suggested excellent ideas on all aspects of the research. Often when I hunted for a complicated solution to a problem, he would delicately propose a simpler, more practical approach, saving me time and frustration.

At Draper Laboratory, Michael Socha became a crucial brainstorming partner, a proficient "borrower" of necessary equipment, and a friend. His sense of humor is remarkably similar to my own, and he helped make Draper an enjoyable place to work.

Heather Gunter probably could have written this thesis herself after hearing every detail of every day, practically as they occurred. She suffered through my setbacks and celebrated my successes—voluntarily! She has irreparably improved my opinion of Canadians everywhere.

Lastly, I would like to thank my family for always believing in my abilities and always supporting my decisions. Nobody understands me better, and nobody is more loved, than they.

Joshua D. Moss
May 24, 1999

Table of Contents

Abstract 3

Acknowledgements 5

List of Figures 9

List of Tables 13

Nomenclature 15

Chapter 1 Introduction 17

1.1 Background 17

1.2 Thesis Motivation 17

1.3 Thesis Outline 18

Chapter 2 Hermetic Encapsulation Testing 21

2.1 Device Modeling 23

2.2 Test Apparatus Design 32

2.3 Results and Discussion 38

2.4 Conclusions and Future Directions 48

Chapter 3 Intraocular Support Structure 55

3.1 Previous Design Philosophy and Development 56

3.2 Iterative Design Philosophy and Development 60

3.3 Results and Discussion of Finite Element Analysis 65

3.4 Results and Discussion of Surgical Testing 80

3.5 Conclusions and Future Directions 84

Chapter 4 Summary and Conclusions 87

4.1 Hermetic Encapsulation Testing 87

4.2 Intraocular Support Structure 88

References 89

Appendix A: Test Model Fabrication Procedures 93

A.1 Silicone-Polyimide Interface Leakage Detection Component 93

A.2 Silicone-Platinum Interface Leakage Detection Component 96

A.3 Model 8 99

Appendix B: LabVIEW Data Acquisition Virtual Interface 103

Appendix C: Mooney-Rivlin Material Model for Rubber Elasticity 109

List of Figures

Figure 1: Prototype implant with photodiode array and polyimide strip electrode 21

Figure 2: Prototype implant after encapsulation 22

Figure 3: Simplified representation of implant and corresponding features of model ... 24

Figure 4: Simple circuit diagram for detection of fluid leakage 25

Figure 5: Model 5, with detailed views of leakage detection components 26

Figure 6: (top) Model 6, with detailed views of leakage detection components 28

Figure 6: (bottom) Model 6, showing Teflon-insulated wire looping up and out of fluid bath. Fluid leakage at the silicone-Teflon interface can thus be detected by the bare portion of the wire, encapsulated in the silicone brick ... 28

Figure 7: Model 7, with detailed views of leakage detection components 29

Figure 8: Model 8, with detailed views of leakage detection components 31

Figure 9: Photograph of single chamber encapsulation test with specimen in place 33

Figure 10: Schematic of an individual chamber in the multi-chamber test block 34

Figure 11: (top) Multi-chamber test block with portions removed to show detail 35

Figure 11: (bottom) Circuit diagram for the setup, not including details of LabVIEW control 35

Figure 12: Hermetic encapsulation test setup (Faraday cage open for test preparation) 36

Figure 13: Setup with Faraday cage closed for testing 36

Figure 14: Sealed, encapsulated diode in saline bath 38

Figure 15: (top) Plot of leakage current at the silicone-platinum interface of Model 5.1 39

Figure 15: (bottom) Plot of leakage current at the silicone-polyimide interface of Model 5.1 39

Figure 16: (top) Plot of leakage current at the silicone-platinum interface of Model 5.2. Data recorded during "business" and "non-business" hours are differentiated 40

Figure 16: (bottom) Plot of leakage current at the silicone-polyimide interface of Model 5.2. Data recorded during "business" and "non-business" hours are differentiated 40

Figure 17: (top) Plot of leakage current at the silicone-Teflon interface of models 6.1 through 6.3 42

Figure 17: (bottom) Plot of leakage current at the silicone-polyimide interface of models 6.1 through 6.3 42

Figure 18: (top) Plot of leakage current at the silicone-Teflon interface of models 6.4 and 6.5 43

Figure 18: (bottom) Plot of leakage current at the silicone-polyimide interface of models 6.4 and 6.5 43

Figure 19: (top) Plot of leakage current at the silicone-platinum interface of models 7.1 through 7.3 44

Figure 19: (bottom) Plot of leakage current at the silicone-polyimide interface of models 7.1 through 7.3 44

Figure 20: Control version of Model 8, with detailed views of leakage detection components 45

Figure 21: (top) Plot of leakage current at the silicone-platinum interface of models 8.1 through 8.4, as compared to leakage currents for fully encapsulated control specimens 47

Figure 21: (bottom) Plot of leakage current at the silicone-polyimide interface of models 8.1 through 8.4, as compared to leakage currents for fully encapsulated control specimens 47

Figure 22: Analysis of leakage failure for Models 5, 6, and 7 48

Figure 23: Analysis of leakage failure for Model 8 (8.1 through 8.4) and Model 8 controls (8.1C through 8.4C) 50

Figure 24: (top) Plot of leakage current at the epoxy-platinum interface of models 9.1 and 9.2 51

Figure 24: (bottom) Plot of leakage current at the epoxy-polyimide interface of models 9.1 and 9.2 51

Figure 25: Silicon test ribbon with improved leakage detection components for encapsulation with silicone 53

Figure 26: Initial design strategy for placement of implantable electronics 55

Figure 27: Simplified representation of IOL and its surgical placement in the eye 56

Figure 28: Commercial IOL modified to hold implantable electronics 57

Figure 29: Stereolithography rapid prototyping procedure 58

Figure 30: Early support structure design (IOS01) based on an intraocular lens 59

Figure 31: First set of iterative designs for intraocular support structure 61

Figure 32: Second set of iterative designs for intraocular support structure. The sloping top surface, a feature of these designs as well as IOS02 and IOS03, is most easily visualized at the exposed face of the haptic notch 62

Figure 33: Necessary location of support tray in relation to haptic notch and electrode array for ease of implantation 63

Figure 34: Third set of iterative designs for intraocular support structure 63

Figure 35: Final iterative design (IOS14) for fabrication from biocompatible material ... 64

Figure 36: (top) Simplified representation of intraocular support structure supported in eye by haptics 66

Figure 36: (bottom) Corresponding model used for dynamic analysis, consisting of a mass suspended by springs inside a moving sphere. *X-Y* is the fixed global coordinate system, and *x-y* is a local coordinate system attached to the sphere 66

Figure 37: Velocity profiles for which the differential equation of mass motion was solved. Each profile followed the same general parameters: maximum velocity and total time of motion 68

Figure 38: Ratio of maximum displacement (due to corresponding velocity profile in Figure 37) to static displacement (under load *ma*). Note 2× ratio for ramp ... 69

Figure 39: Simple beam under tip load modeled with 80 elements (force in Newtons) ... 70

Figure 40: Deflection of simple haptic compared with beam theory prediction 71

Figure 41: Schematic of hook-shaped haptic input model (represents the left haptic in the top portion of Figure 36; the point in contact with the inside edge of the eye is considered bound in all directions) 71

Figure 42: Hook-shaped haptic under tensile load modeled with 320 3-D elements 72

Figure 43: Finite element model of IOS14 support tray with silicon chip under gravity loading (individual elements not pictured) 74

Figure 44: Tray deflection results for 376 element model (scale in millimeters) 74

Figure 45: Finite element model of IOS05 support tray with silicon chip 75

Figure 46: Tray deflection results for 416 element model (scale in millimeters) 75

Figure 47: Y-displacement of the annulus under load on the left haptic notch (scale in meters) 76

Figure 48: Z-displacement of the annulus under load on the left haptic notch (scale in meters) 77

Figure 49: *Y*-direction stresses in 82 element annulus model under compression load (scale in N/m^2) 79

Figure 50: *Z*-direction stresses in 82 element annulus model under compression load (scale in N/m^2) 79

Figure 51: Intraocular support structure with no electronics resting on rabbit eye after phacoemulsification and removal of the lens 80

Figure 52: Intraocular support structure with no electronics successfully implanted in rabbit eye 81

Figure 53: Modified final design (IOS14a) for intraocular support structure 82

Figure 54: Finite element model of IOS14a support tray with silicon chip 83

Figure 55: Tray deflection results for 572 element model (scale in millimeters) 83

Figure B1: Page 0 of LabVIEW data acquisition virtual instrument (VI) 103

Figure B2: Page 1 of LabVIEW data acquisition virtual instrument (VI) 104

Figure B3: Page 2 of LabVIEW data acquisition virtual instrument (VI) 105

Figure B4: Page 3 of LabVIEW data acquisition virtual instrument (VI) 105

Figure B5: Page 4 of LabVIEW data acquisition virtual instrument (VI) 106

Figure B6: Page 5 of LabVIEW data acquisition virtual instrument (VI) 107

Figure B7: Front panel graphical interface for user control of data acquisition VI 107

Figure C1: Uniaxial tension of a linear elastic material 109

Figure C2: Illustration of strain energy for uniaxial tension of a linear elastic material ... 111

List of Tables

Table 1: Results of three-dimensional modeling of simple beam type haptic 70

Table 2: Results for three-dimensional modeling of hook-shaped haptic 72

Table 3: Results of two-dimensional modeling of annulus 78

Nomenclature

X_m — Position of the mass in the fixed global coordinate system

$\ddot{X}_m$ — Acceleration of the mass in the fixed global coordinate system

X_s — Position of the sphere in the fixed global coordinate system

$\ddot{X}_s$ — Acceleration of the sphere in the fixed global coordinate system

x_m — Position of the mass in a moving local coordinate system attached to the sphere

$\ddot{x}_m$ — Acceleration of the mass in a moving local coordinate system attached to the sphere

a — Constant acceleration of the mass

A — Constant acceleration of the sphere

k — Spring constant

l_i — Current length in the i-direction

l_{0i} — Original length in the i-direction

ε_{ij} — Strain in the i-direction with respect to the j-direction

λ_i — Stretch in the i-direction

A_i — Area of the surface to which the i-direction is perpendicular

F_i — Force in the i-direction

σ_{ij} — Stress on area A_i caused by a force in the j-direction

E — Elastic (Young's) modulus of a linear elastic material

W — Strain energy

I_1 — First invariant of the second order stretch tensor

I_2 — Second invariant of the second order stretch tensor

I_3 — Third invariant of the second order stretch tensor

C_{mn} — Higher-order Mooney-Rivlin material constant

ρ — Density

κ — Bulk modulus

ν — Poisson ratio

G — Small strain shear modulus of a rubber elastic material

Chapter 1
Introduction

1.1 Background

Many patients lose their sight due to selective loss of photoreceptors, the specialized cells in the retina that detect light; the remainder of the retina often does not degenerate for many more years. The goal of the Retinal Implant Project is to use electrical stimulation to bypass the lost photoreceptors. The retinal prosthesis could thus theoretically restore some vision to blind patients with certain diseases of the retina [1]. One such disease, retinitis pigmentosa, affects 1.6 million people worldwide and is the leading cause of inherited blindness [2]. Another significant disease is age-related macular degeneration (AMD). The leading cause of blindness in the Western world, AMD affects 700,000 Americans each year [3].

In the currently planned prosthesis design, an eyeglass-mounted CCD camera will collect visual scene data, and a modulated infrared laser will transmit the data to a small photodiode array that is implanted in the eye. The photodiode array and associated microcircuitry will then drive an array of small electrodes that are fabricated on a thin polyimide strip. With the strip resting against the retina, the electrodes will be in position to stimulate the intact retinal nerve cells and evoke a visual response. Hopefully, the patient will "see" the visual scene data transmitted to the photodiode array by the laser, facilitating simple tasks such as navigation down a street [1, 4, 5].

1.2 Thesis Motivation

Chronic testing of a completely implantable device requires hermetic encapsulation of all electronics that will be positioned in the eye. Other prostheses, such as cardiac pacemakers, cochlear implants, and neuromuscular stimulators, have been effectively protected by a metal or ceramic housing [6, 7, 8, 9]. However, these housings would interfere with light transmission from the external laser source to the photodiode array

and are therefore impractical. Encapsulation of the electronics in transparent polymers is a potential alternative; however, the prosthesis design requires both a polyimide electrode array and a return wire to penetrate the protective capsule. An effective encapsulant must bond well to these materials, as a poorly bonded interface would create a leakage path for fluid. Therefore, techniques for hermetically sealing the electronics must be methodically designed and tested. Design and implementation of a hermetic encapsulation test was the primary motivation for this thesis.

One of the guiding principles of retinal prosthesis design has been to minimize disruption of normal eye anatomy [1]. Originally, the photodiode array and other implanted microelectronics were to be supported on the retinal surface. However, this placement could induce surface scarring and other damage to the retina [10]. Therefore, the decision was made to move the active microelectronics to a platform just behind the iris. Early designs of this platform had several problems. One design was time-consuming and expensive to produce, and another had rigid components that could damage the eye. In addition, both designs obstructed the surgeon's line of sight to the retina when they were in place behind the iris. Therefore, the second goal of this thesis was to improve the design of the intraocular platform, making it an effective support structure for the electronics while not interfering with surgical implantation. The reduced retinal burden afforded by the prosthesis, as compared to the original design, may improve its biocompatibility.

1.3 Thesis Outline

This chapter has provided background on the Retinal Implant Project, including the ultimate goal of creating a retinal prosthesis as well as current plans for how such a prosthesis will be implemented. Also, the motivation for this thesis was discussed, citing two engineering issues important to the success of the prosthesis. Chapter 2 addresses hermetic encapsulation testing. Design of simple, inexpensive prosthesis models and a robust, sensitive test apparatus are described, and the results for rigorous tests on silicone rubber and early tests on a harder epoxy are shown. In addition, several potential future directions for continuation of this work are summarized. The focus of Chapter 3 is the design of an intraocular support structure. Previous designs are briefly explained, and the

iterative design technique made possible by rapid prototyping is illustrated. Results of both finite element analysis of the support structure and surgical analysis are also discussed in Chapter 3. Chapter 4 contains a summary of the thesis.

Chapter 2
Hermetic Encapsulation Testing

A prototype implant that contains many of the important components of the intended design is shown in Figure 1. In the prototype, the photodiode array is supported on a plastic ring, which will be discussed later in this thesis. Connected to the photodiode array are a thin polyimide strip and a gold wire. The strip is actually a layered structure, consisting of very fine metal wires sandwiched between two layers of polyimide. At one end, the metal wires are exposed and connected to the photodiode array. The other ends of the wires within the strip are exposed in a 5×5 array of electrodes, which would deliver current directly on the retinal surface.

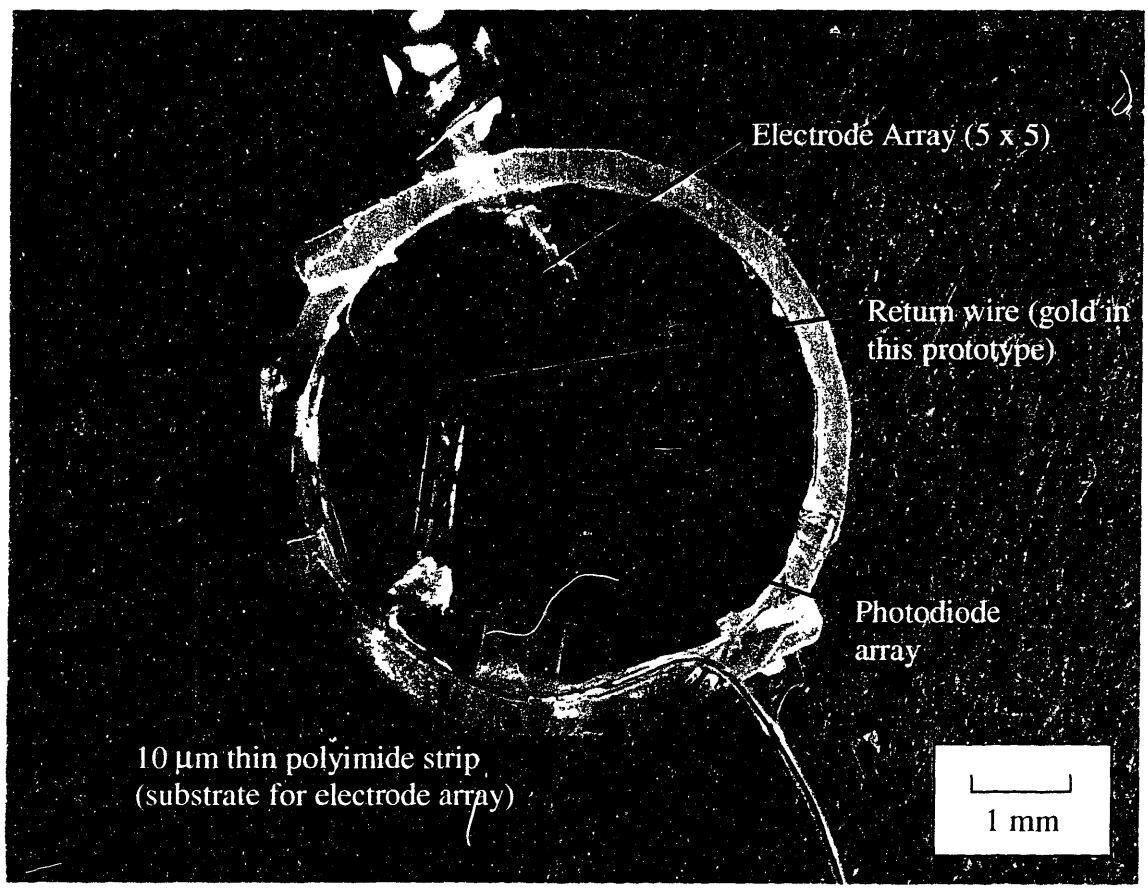

Figure 1: Prototype implant with photodiode array and polyimide strip electrode

Figure 1 gives the illusion that the polyimide strip is attached to the plastic ring near the electrode array end, but the strip is in fact free of the ring at all points. The gold wire is 0.001 inches in diameter and serves as a distant electrical return for the electrodes. It too is connected to the photodiode array and is then attached to the plastic ring for support. The wire can be any biocompatible metal such as gold, platinum, or iridium.

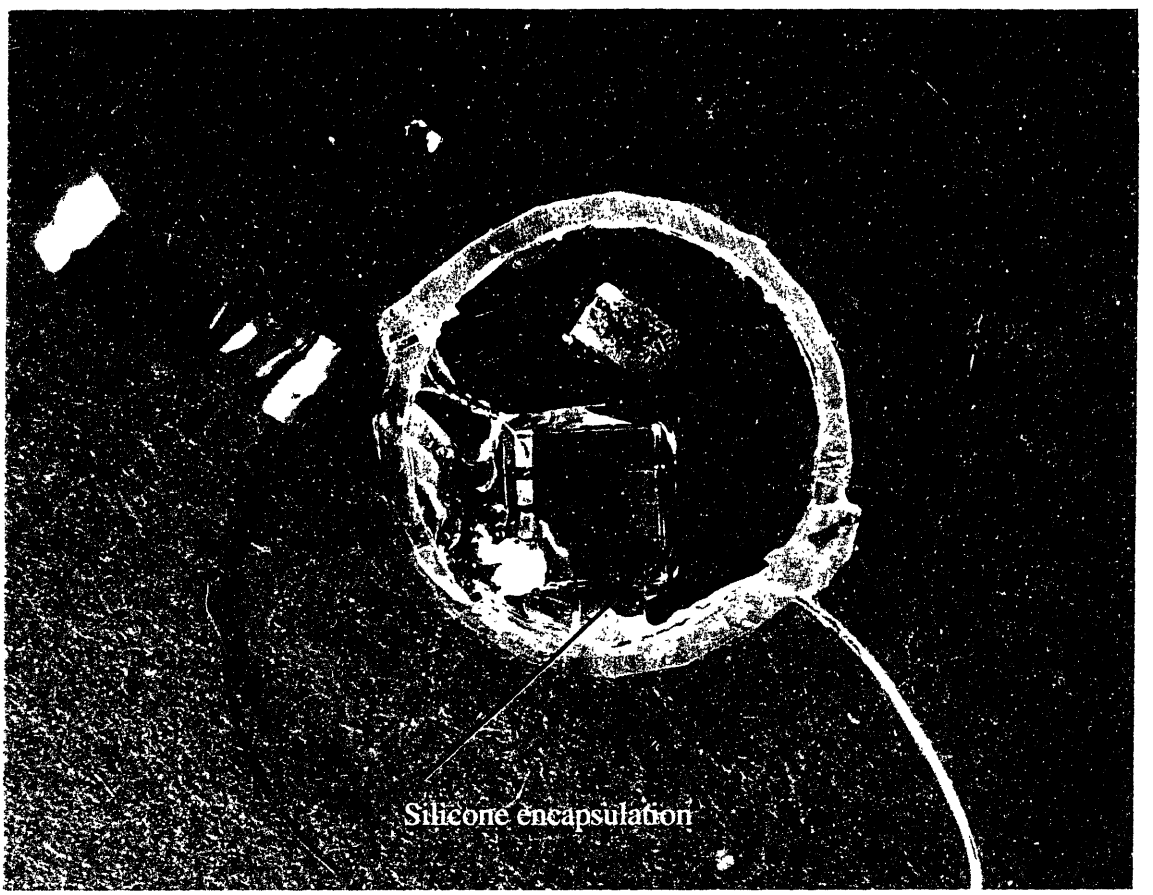

Figure 2: Prototype implant after encapsulation

Figure 2 is a photograph of the same prototype implant shown in Figure 1 after encapsulation. The photodiode array, as well as any other implantable electronic components in future prototypes, will not function if directly exposed to the fluids in the eye. As noted in Chapter 1, metal or ceramic housings would interfere with light transmission from the external laser and are therefore impractical. Studies have shown that silicone elastomers can protect implanted microcircuitry for prolonged periods [11, 12, 13]. In addition, these elastomers are relatively inexpensive and easy to apply. They were therefore a logical choice for initial encapsulation testing. The photodiode array in Figure 2 is completely encased in a

thin layer of clear silicone rubber. However, both the polyimide strip and the return wire penetrate the protective capsule, creating a hermetic sealing challenge not addressed in previous studies [11, 12]. To be effective, the silicone or another encapsulant must bond well to these structures, as a poorly bonded interface would create a leakage path for fluid.

There are two main tasks in developing an effective *in vitro* hermetic encapsulation test for this prototype: modeling the implant and designing a test apparatus. The first section of this chapter details the development of an accurate and cost effective implant model. The next section describes design of a sensitive, automated test apparatus. Results of comprehensive encapsulation tests with silicone rubber are discussed as well as preliminary results of tests using epoxy encapsulation

2.1 Device Modeling

Implant components such as the photodiode array and the polyimide structure are both time-consuming and expensive to produce. Therefore, an accurate model was necessary for timely and cost-effective testing of multiple specimens. Several design criteria were used to create these models:

- *Reproduction of implant material interfaces:* The models must contain the same potential leakage paths that were shown in Figure 2.
- *Reproduction of salient implant dimensions:* The thickness of encapsulant around the photodiode array will change the amount of time necessary for fluid to affect implant performance; models must have similar protection.
- *Reliable detection of failure risks:* The models must have features that allow detection of any fluid leakage that might damage the implant.
- *Quick, inexpensive, and repeatable fabrication:* Utilization of the models for encapsulation testing must be significantly more efficient than using actual implants.
- *Flexibility to modify both dimensions and materials*: Model design must be sufficiently flexible to allow testing of multiple encapsulants and configurations.

Figure 3 depicts the basic concepts used in designing the models, addressing all of the above criteria. The left portion of the figure is a simplified representation of the prototype implant surrounded by the fluid in the eye. The most significant features are the potential

fluid leakage paths to the photodiode array. The first path, indicated by red checkered arrows in the figure, relies upon the integrity of the bond at the silicone-polyimide interface to prevent leakage. The second path, indicated by solid blue arrows, relies upon the integrity of the bond between the silicone and the return wire; in this case, a silicone-platinum interface must be tested.

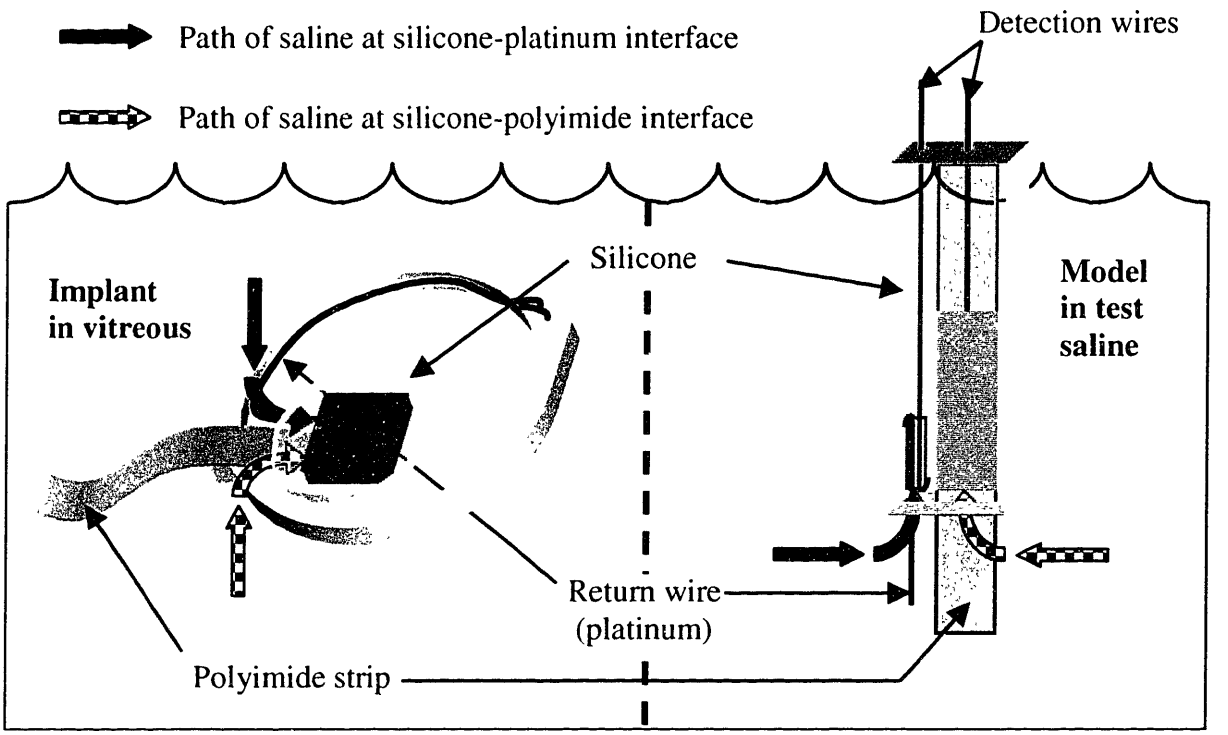

Figure 3: Simplified representation of implant and corresponding features of model

The model on the right side of Figure 3 shows a brick-like structure molded from silicone. Potential leakage paths identical to those shown in the prototype implant are created using solid strips of polyimide and platinum wire. Detection of fluid leakage at these paths is accomplished by wires which run from outside the model and surrounding fluid to specific points along the paths. The distances from these wires to the bottom edge of the silicone brick can be easily modified to simulate encapsulant thickness. Therefore, the wires represent the electrical contacts of the photodiode array. Current from the surrounding fluid to the contact wires can be measured as a precise indication of the amount of fluid leakage at both the silicone-polyimide and silicone-platinum interfaces; the simplified circuit is diagramed in Figure 4. In addition, any unlikely fluid leakage through the bulk silicone

material can be detected. The thickness of the encapsulant layer on various areas of the implant (see Figure 2) is reproduced by the overall dimensions of the brick..

As shown in the circuit diagram of Figure 4, current can be measured when a voltage is applied between the contact wire and the surrounding fluid. The fluid and the leakage path each represent a resistor in the circuit. It was expected that the resistance of the fluid would be very low, and the resistance of the leakage path would change with the amount of fluid leakage. Therefore, larger currents would indicate more extensive fluid leakage.

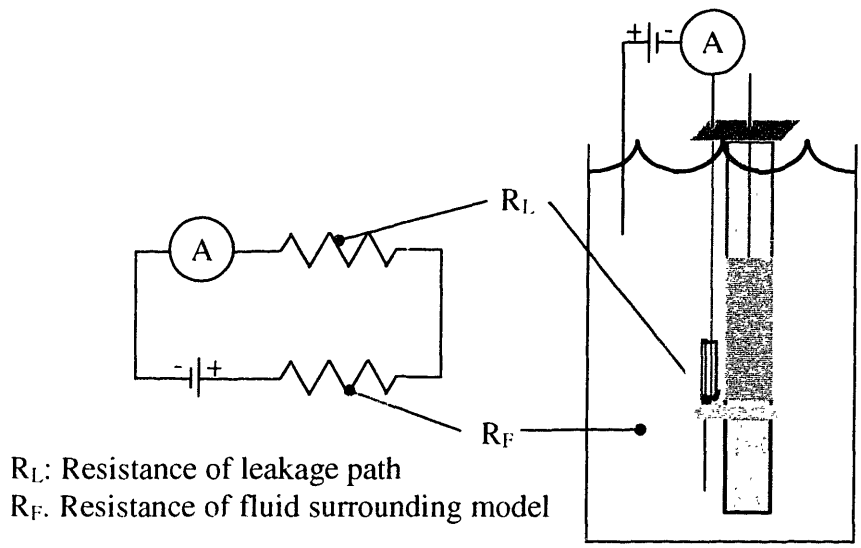

Figure 4: Simple circuit diagram for detection of fluid leakage

Reproduction of material interfaces and encapsulant thickness is a relatively trivial task requiring only a well machined mold and careful measurements during model fabrication. The most significant challenge in making the model an accurate representation of the implant is reliable detection of fluid leakage, which can occur anywhere along the potential leakage paths and, though less probable, through the bulk silicone material. The contact wires must carry current from the point of fluid penetration to current measuring devices but must not actually contact the test fluid. One of the earliest models developed over the course of this thesis is shown in Figure 5. It will be referred to as Model 5; previous models were similar but contained only a silicone-polyimide or a silicone-platinum interface rather than both.

Model 5 was fabricated such that any fluid leakage at the silicone-polyimide interface would create a short circuit between the surrounding fluid and a platinum wire. The wire rested flat against the polyimide, as shown on the right side of Figure 5, and it was affixed to the strip with dabs of silicone (NuSil CF18-2186, NuSil Technology, Carpinteria, CA). For leakage detection at the silicone-platinum interface, a bare wire was encapsulated alongside an insulated wire such that the wires were not in contact electrically, as shown on the left side of Figure 5. Fluid leakage along the platinum wire would create a short circuit between the surrounding fluid and the bare end of the insulated wire.

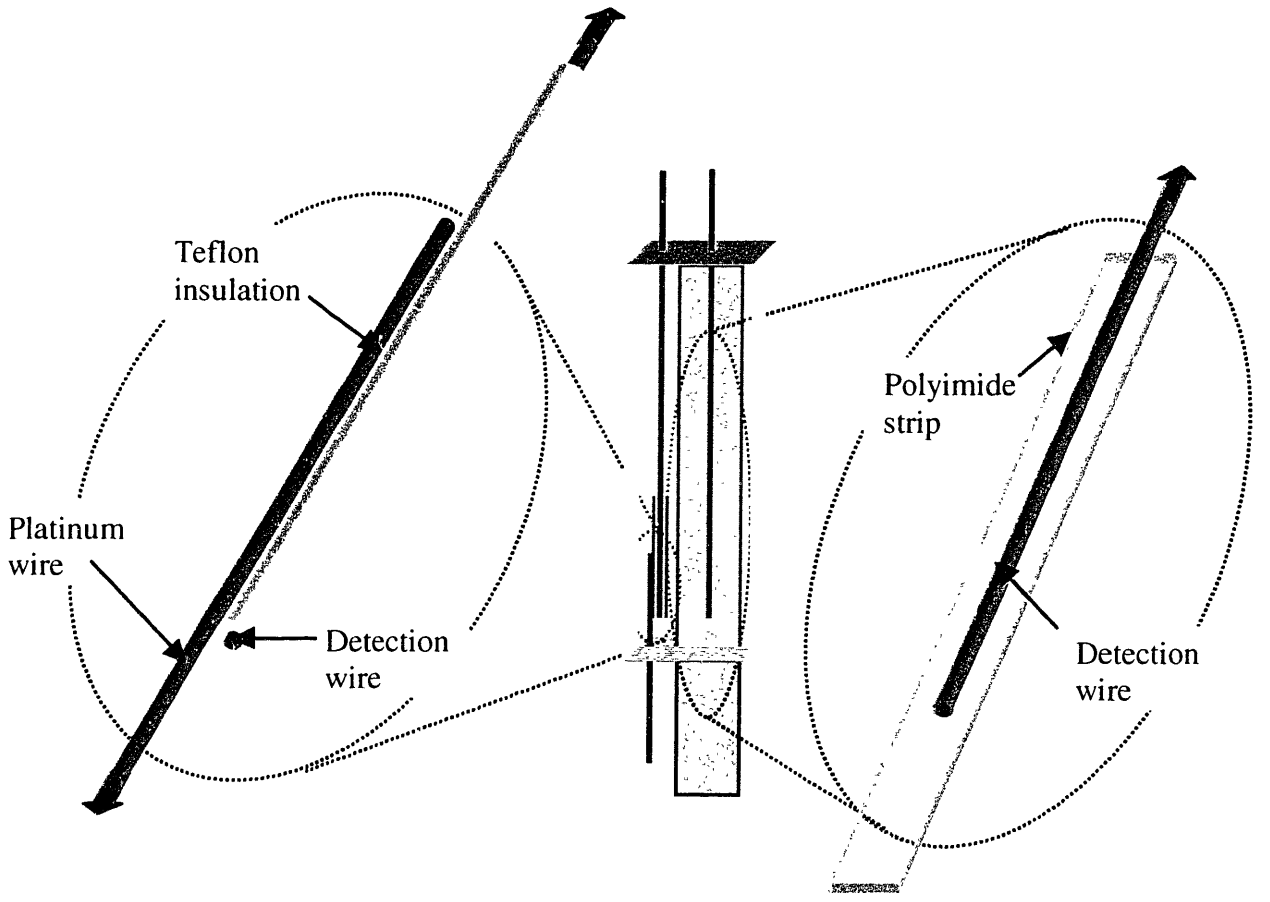

Figure 5: Model 5, with detailed views of leakage detection components

Model 5 exhibited somewhat unusual behavior. After fabrication, qualitative examination of the structure revealed non-optimal bonding between silicone and polyimide;

excess silicone could be scraped off the polyimide with little effort and no damage to the strip. In addition, bonding between silicone and platinum was poor. However, the quantitative results, which will be discussed in Section 2.3, showed no leakage at either interface for the entire length of the test: twelve days for one specimen, four weeks for another. These results raised questions regarding the reliability of leakage detection, especially at the platinum wire leakage path. Therefore, a new model was designed with an interface that would almost surely allow leakage and a more reliable configuration for leakage detection.

For Model 6 and subsequent models, NuSil MED4-4220 silicone was chosen because of its success in D. Edell's study [12]. In Model 6, the platinum wire representing the implant return wire (see Figure 3) was replaced with a partially insulated platinum wire. The portion of wire which penetrated the silicone encapsulation and entered the surrounding fluid was insulated with Teflon, as detailed in the top part of Figure 6. The bare portion of the wire, encapsulated in silicone, served as the detection component for this silicone-Teflon interface. The Teflon-insulated portion was looped up and out of the fluid bath to prevent a short circuit between the end of the wire and the fluid, as shown in the bottom part of Figure 6. Because the potential leakage path and the detection component were directly connected—they were two parts of the same wire—it was predicted that leakage detection would be more reliable. The interface between the silicone and the Teflon insulation was predicted to be very poorly bonded.

The results for Model 6 were less surprising than those for Model 5, and they will be discussed in greater detail in Section 2.3. In five specimens tested, four exhibited large leakage currents at the Teflon-insulated wire. It appeared possible that the very small portion of silicone separating the leakage path and detection wires in Model 5 may have prevented leakage detection. The reliability of leakage detection at the polyimide strip was therefore called into question; a very small portion of silicone could easily separate the detection wire from the polyimide during fabrication of the model. Indeed, no leakage was observed at the silicone-polyimide interface in four of the five specimens for 60 days.

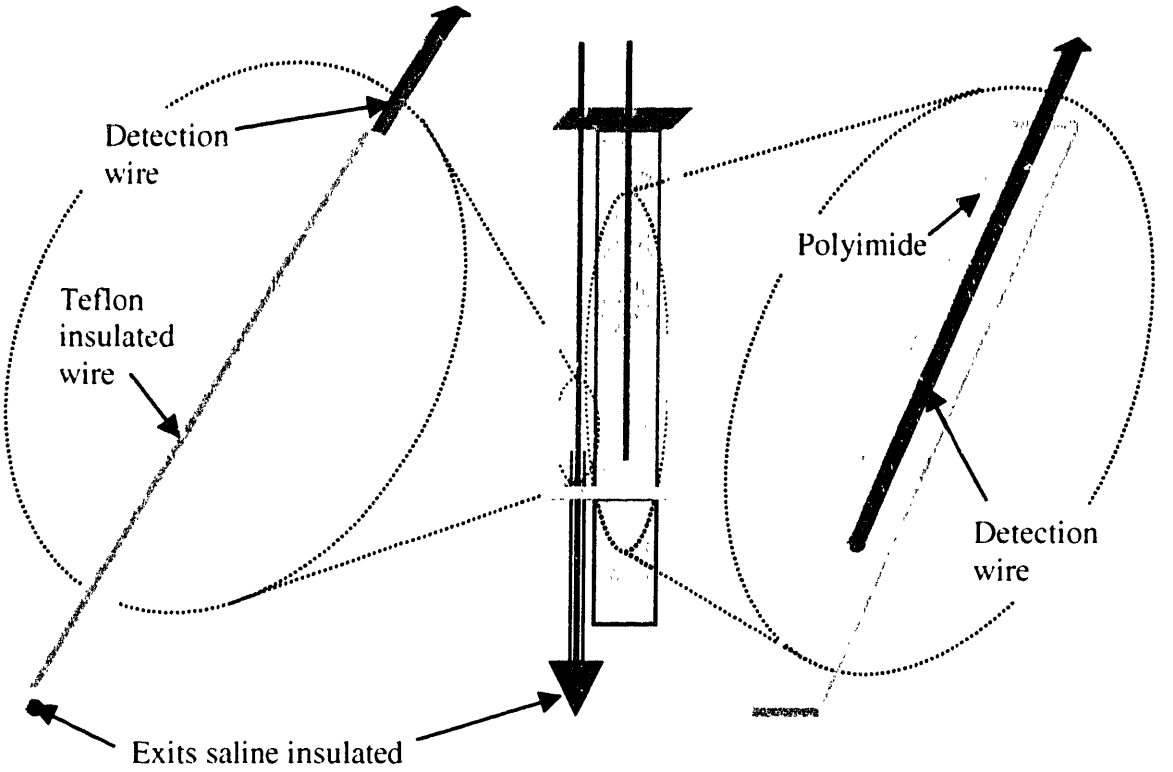

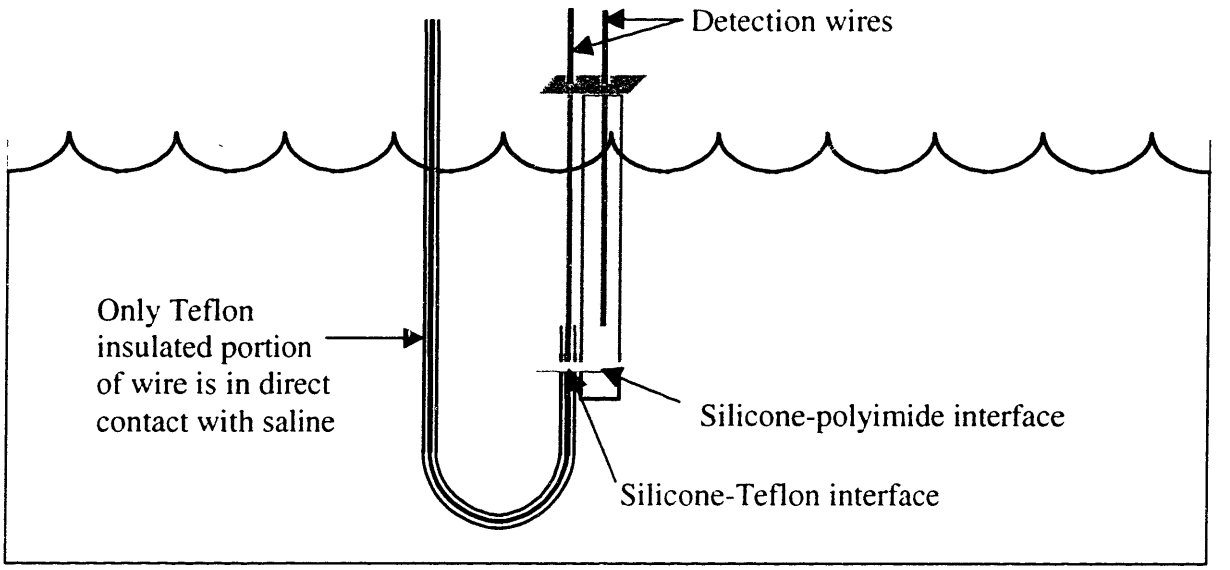

Figure 6: (top) Model 6, with detailed views of leakage detection components. (bottom) Model 6, showing Teflon-insulated wire looping up and out of fluid bath. Fluid leakage at the silicone-Teflon interface can thus be detected by the bare portion of the wire, encapsulated in the silicone brick.

In designing Model 7, two new problems had to be addressed. Model 6 results indicated that a Teflon insulated return wire could not be included in a silicone encapsulated implant; the silicone-Teflon interface was too susceptible to leakage. Therefore, a more reliable arrangement for detection of leakage at a bare platinum wire was necessary. In addition, a better detection arrangement for the polyimide strip was desirable; the arrangement used in Models 5 and 6 had not been proven ineffective, but opportunities for misleading results seemed possible. Detailed views of the detection components in Model 7 are diagramed in Figure 7.

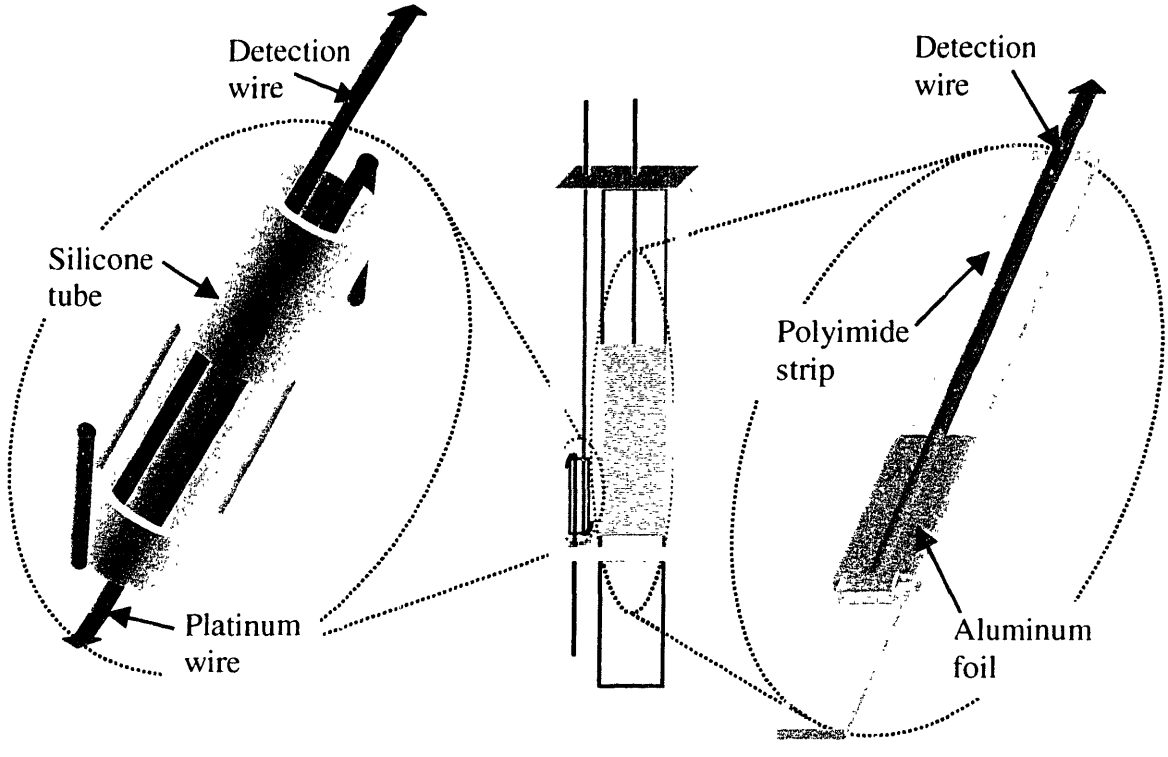

Figure 7: Model 7, with detailed views of leakage detection components

The right side of the figure shows how the polyimide structure was modified to improve leakage detection. A small piece of aluminum foil was affixed to the polyimide by wrapping it around the sides of the strip. Also, a slit was cut in the polyimide near the lower end, and part of the foil was inserted through it. The foil was flattened against the strip on both the top and bottom surfaces, and a detection wire was inserted between the aluminum

and the polyimide to carry current outside the silicone brick (see Appendix A.1). This arrangement had two major advantages over that used in Models 5 and 6. First, the possibility of silicone separating the polyimide and the detection structure during brick molding was greatly reduced; the aluminum could be pressed flat onto the polyimide and in fact went through the strip as if they were a single structure. Second, leakage anywhere along the entire width of the polyimide could be detected rather than leakage at one narrow point in the middle. Leakage at the silicone-polyimide interface was observed in all three Model 7 specimens within 18 days of submersion in fluid.

To detect leakage at the silicone-platinum interface, two wires were arranged inside a small silicone tube, as shown on the left side of Figure 7. The detection wire penetrates the brick at the top, without contacting the surrounding fluid. The other wire penetrates the brick at the bottom, creating the potential leakage path. The wires in the tube were less than 500 μm apart, but contact between them was prevented during fabrication. The ends of the tube were then sealed with NuSil MED4-4220 silicone before being encapsulated in the model, also made of NuSil MED4-4220. Therefore, the two wires were only separated by air, and excess silicone could not get between them during molding. The design was intended to enable detection of any fluid that leaked into the tube along the silicone-platinum interface, creating a short circuit between the two wires. Furthermore, a continuous fluid path from the surrounding fluid to the detection wire was necessary to create a short circuit in previous designs; in this design, only one droplet between the two wires in the tube—enough to damage the circuitry in an actual implant—was needed for detection. All three of the specimens created using the Model 7 design exhibited leakage at the silicone-platinum interface within one day of submersion.

The disparity in results from Models 5 and 6 with those from Model 7 raised concerns about false detection of leakage at the silicone-platinum interface. The results for the polyimide strip were not surprising based on the qualitative examination of the silicone-polyimide interface bond. However, the possibility of the two wires in the tube coming into physical contact during testing was real, considering their very close proximity. A small but significant modification was made to Model 7 to address this problem, and Model 8 is diagramed in Figure 8.

A small piece of filter paper was added to the silicone tube assembly in Model 8, as seen on the left side of Figure 8. The filter paper was intended to prevent physical contact

between the platinum wire and detection wire while still allowing fluid to create a short circuit between them.

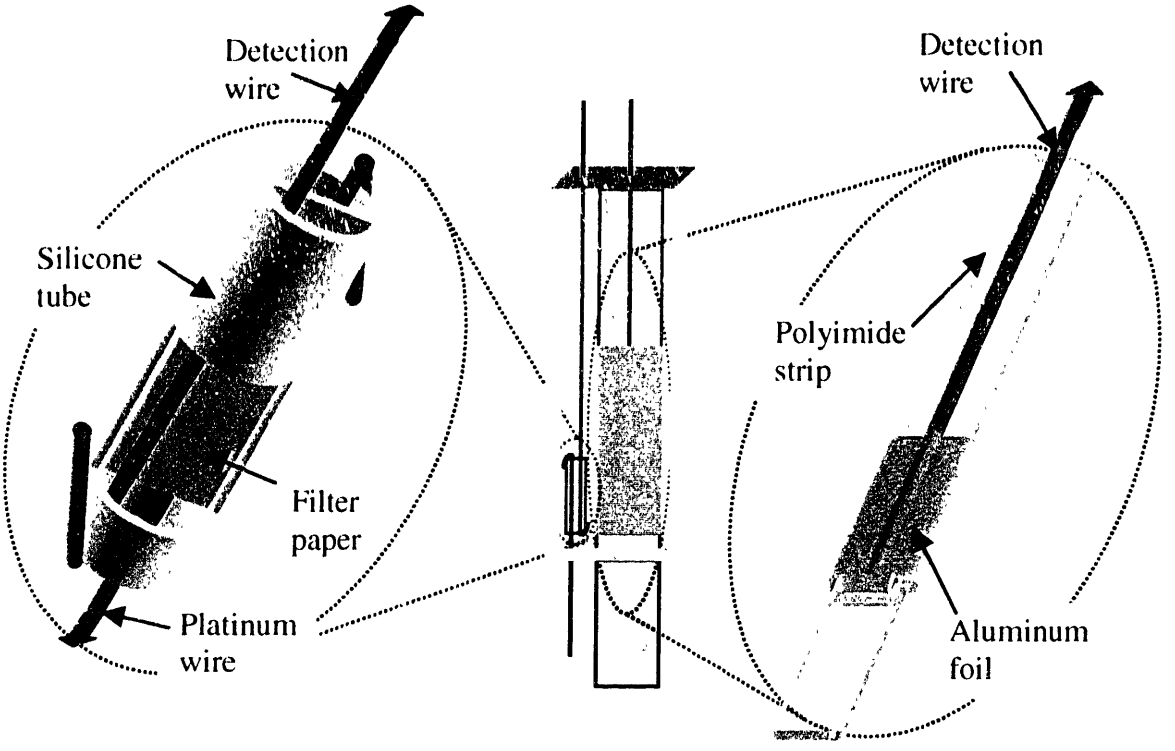

Figure 8: Model 8, with detailed views of leakage detection components

The results from all the models described in this section will be presented in greater detail in Section 2.3. In addition, future modifications to the models will be proposed in Section 2.4 and fabrication procedures are discussed in Appendix A.

2.2 Test Apparatus Design

After reliable models are fabricated, an apparatus capable of testing their survivability in the eye is necessary. The following design requirements were considered in the design of this apparatus:

- *Detection of very low currents:* The apparatus must be capable of differentiating between fluid leakage and non-leakage. A very small amount of fluid is enough to damage the implanted microelectronics, so even very small currents may represent deleterious leakage.
- *Simulation of physiologic conditions:* The *in vitro* test must provide conditions which approximate the environment of the eye.
- *Support of multiple models for indefinite periods of time:* Multiple models must be tested to yield reliable conclusions about the results. Also, the models must be tested for the equivalent amount of time that the prosthesis is intended to remain implanted (for initial tests, the goal was to prevent leakage for 60 days).
- *Ease of modification and expansion:* The apparatus should ideally be expandable to support models in future tests.

Low current measurement required sufficiently sensitive ammeters and a setup which was very stable and resistant to external disturbances. One key concern was shielding against electromagnetic fields carried by people moving around in the same room as the setup. Mechanical vibration that could potentially induce current in the wires was also considered. The equipment used was based primarily on previous encapsulation studies [11], the core devices being Keithley Model 617 Programmable Electrometers (Keithley Instruments, Inc., Cleveland, OH).

To simulate physiologic conditions, models were submerged in a sterile intraocular irrigating solution (Alcon Laboratories, Inc., Ft. Worth, TX). In early tests, this saline solution was kept at room temperature, but the final setup heated the saline to 37°C. Figure 9 is a photograph of a single chamber encapsulation test with a test specimen in place; this early apparatus was only used for Model 5. Initially, data was recorded by the electrometers themselves and then transferred manually to a spreadsheet for plotting. Eventually, however, LabVIEW software (National Instruments, Austin, TX) was added to control the electrometers and record the data. The addition of LabVIEW greatly decreased the

maintenance required, as data could be plotted whenever convenient rather than when the limited electrometer memory was full.

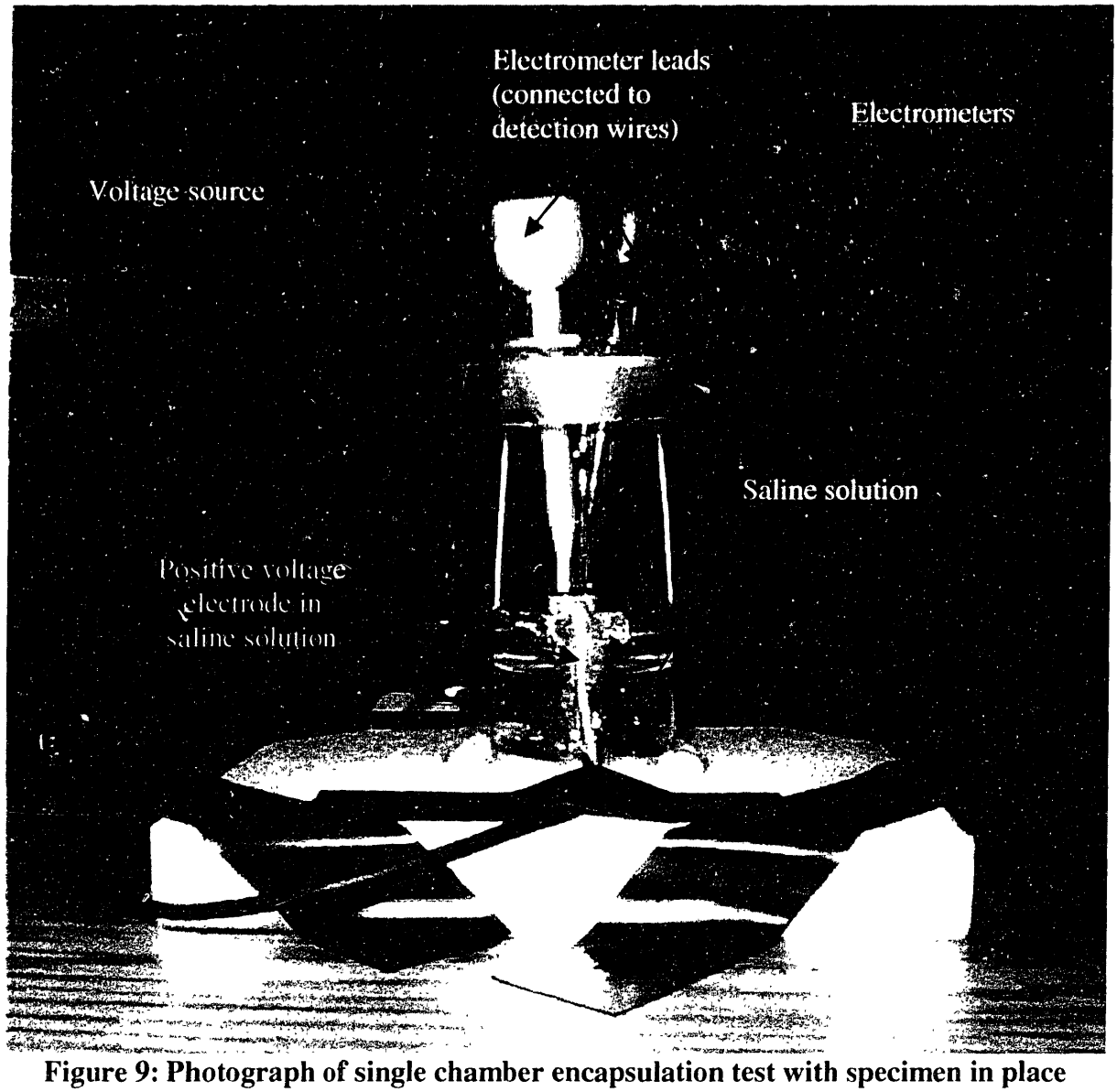

Figure 9: Photograph of single chamber encapsulation test with specimen in place

Once measurements in the single chamber were sufficiently low and stabilized, a multiple-model apparatus was constructed. The apparatus could support up to nine test specimens simultaneously in a 37°C saline environment. Measurements were still recorded by LabVIEW software, which controlled a Keithley Model 7001 Switch System and two electrometers. Figures 10 is a simplified schematic of an individual chamber. Each chamber included connections to the two electrometers as well as a styrofoam float. Test specimens

are inserted into a float and move up and down with it. The float was added to solve some of the difficulties of heating the saline. By covering most of the surface of the saline, it helps slow evaporation so that the saline does not need to be refilled as often. Also, as the saline evaporates, the float allows the test specimen to remain submerged. Earlier attempts at evaporation prevention by covering each chamber with a large cap proved unsuccessful; saline continued to evaporate, only to condense on top of the test specimen and create unstable measurements.

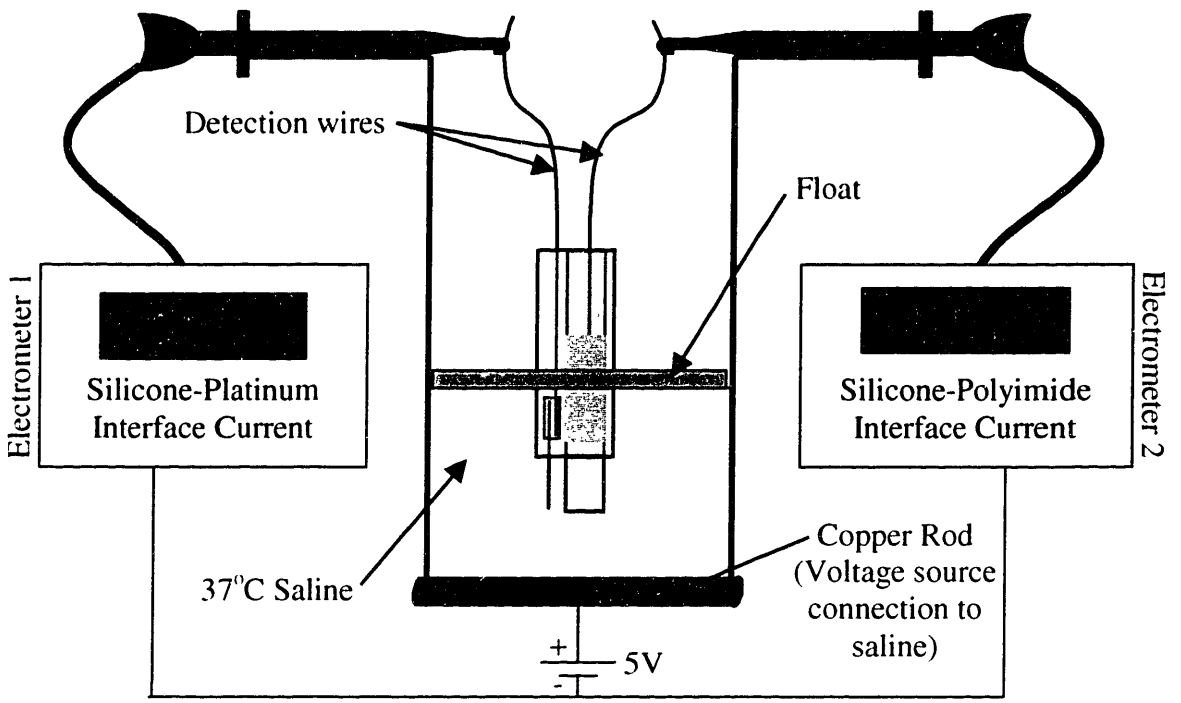

Figure 10: Schematic of an individual chamber in the multi-chamber test block

The top portion of Figure 11 shows the nine-chamber test block, each with a float and model in place. Parts of the block are cut away to show detail, and electrical connections for all but one chamber were removed for clarity. The copper rods that are exposed at the bottom of each chamber are all connected by a single wire to the voltage source. The electrical connections for each chamber are connected to the switch system, which is in turn connected to the two electrometers. The bottom portion of Figure 11 is a simplified circuit diagram of the nine-chamber setup.

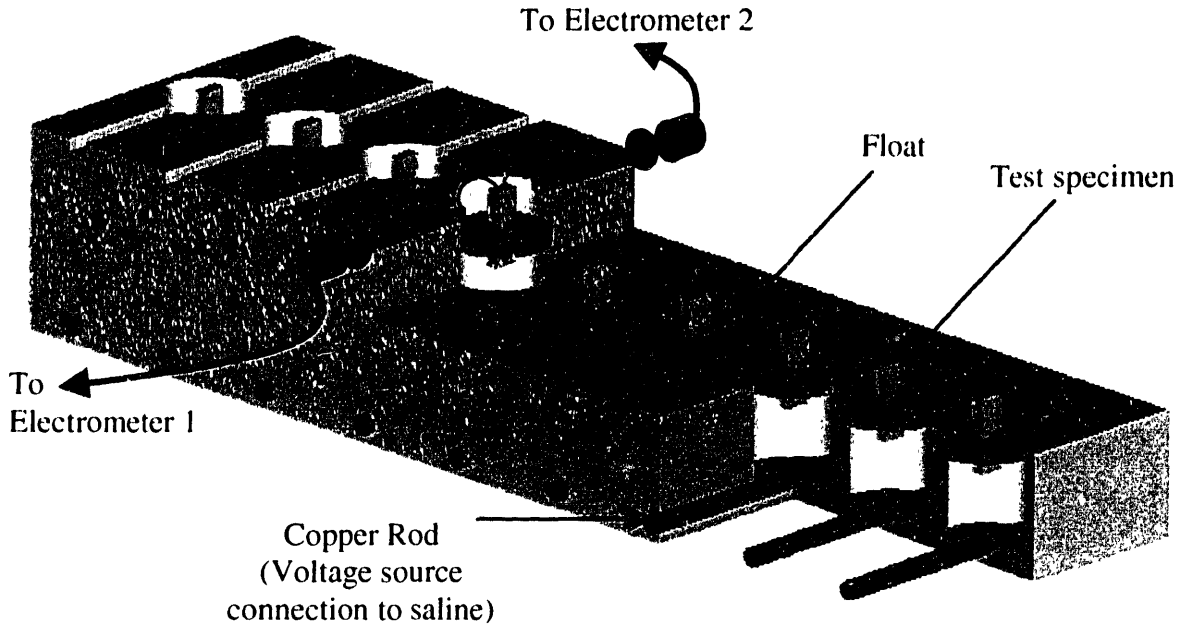

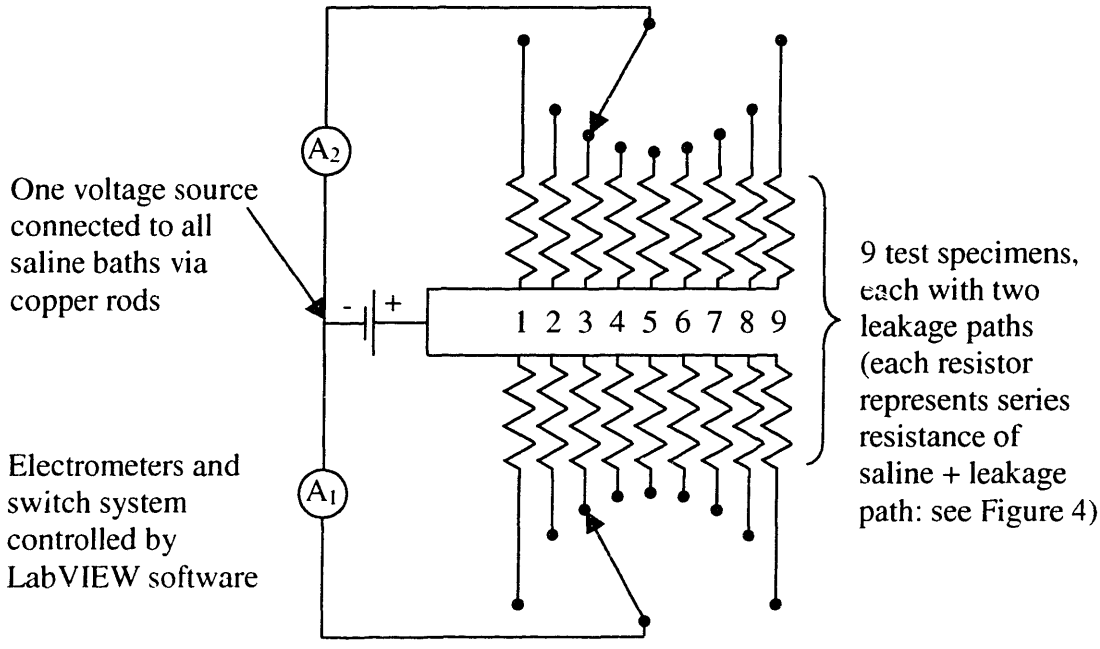

Figure 11: (top) Multi-chamber test block with portions removed to show detail. (bottom) Circuit diagram for the setup, not including details of LabVIEW control.

Electrical stability of the test apparatus is constantly being improved to produce more stable and conclusive results. A crude Faraday cage constructed from a large cardboard box and aluminum foil was added during one of the final tests, and it has recently been replaced by a more sophisticated aluminum chamber; the entire setup is pictured in Figures 12 and 13.

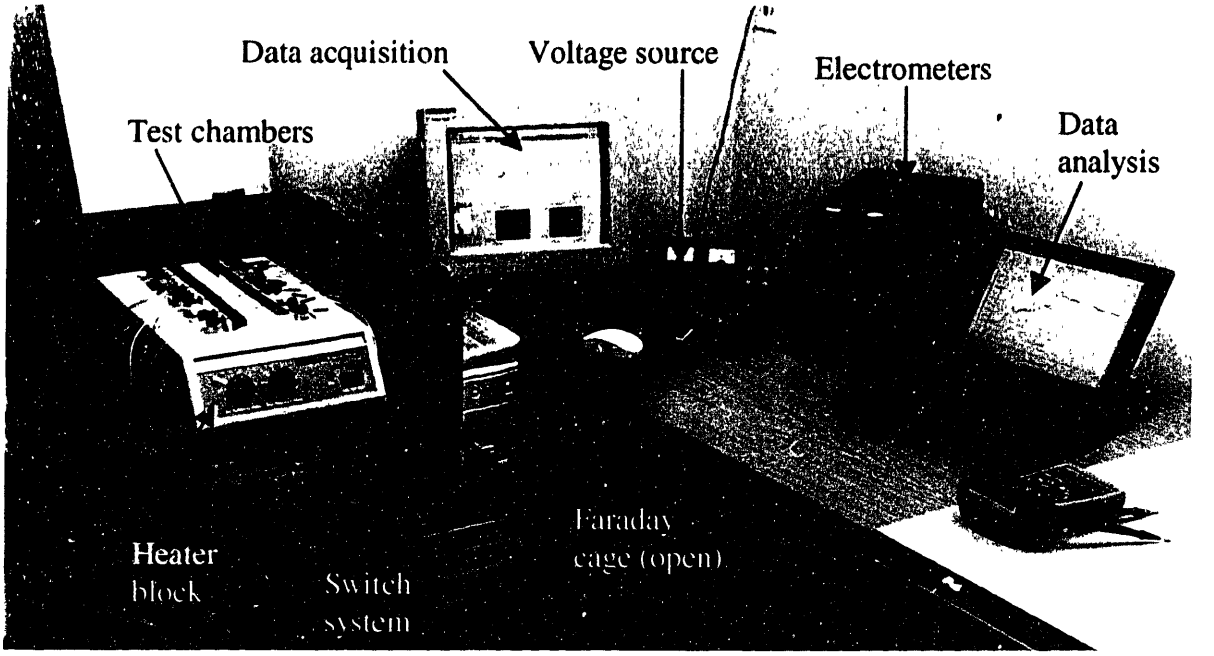

Figure 12: Hermetic encapsulation test setup (Faraday cage open for test preparation)

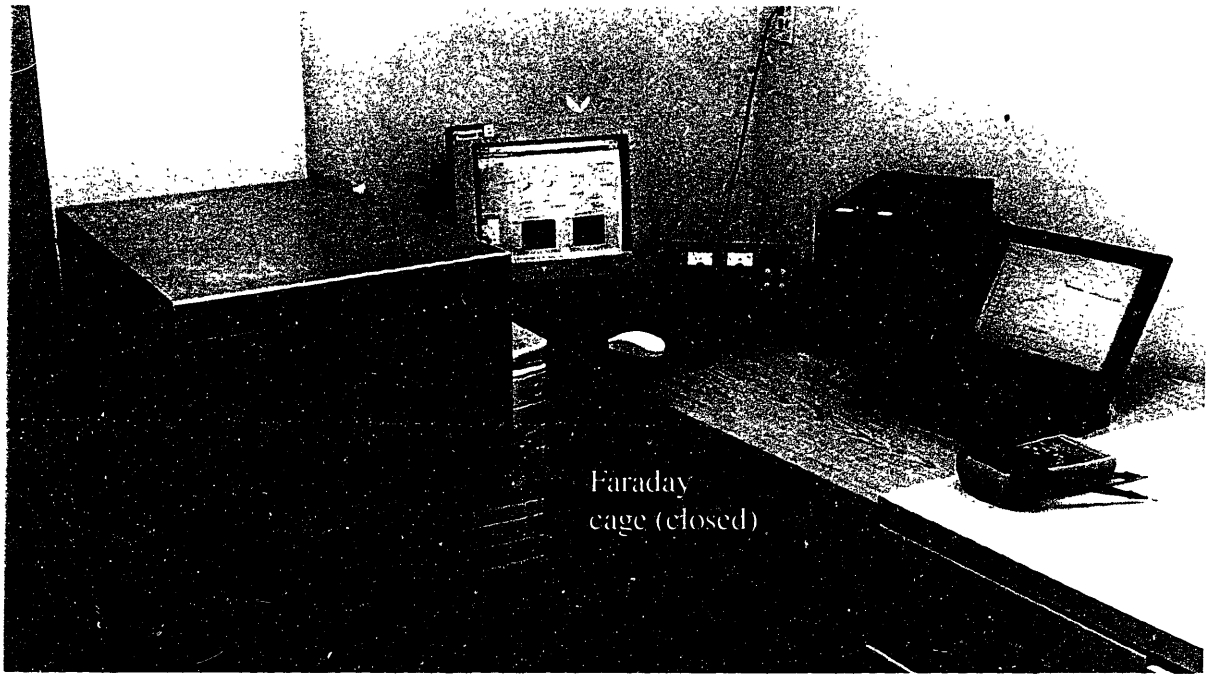

Figure 13: Setup with Faraday cage closed for testing

LabVIEW, shown running on the data acquisition computer in Figure 12, selects a chamber and closes the circuit between the two detection wires and the two electrometers. After a settling time of approximately two minutes, ten current readings are taken for each potential leakage path, and the average is recorded in a text file. This file is later transferred to a spreadsheet on a separate computer for analysis. Schematics of the LabVIEW program are included in Appendix B. To maintain saline temperature at 37°C, the test block was placed on a standard heater block (VWR Scientific Products, West Chester, PA), also shown in Figure 12.

In addition to shielding improvements, protection against saline evaporation is continually evolving and will soon include humidifying devices inside the Faraday cage. Other developments and future improvements will be discussed in Section 2.4.

2.3 Results and Discussion

To gain familiarity with the electronics and test setup, initial soak tests were done with a sealed, commercial diode that was completely encapsulated in silicone. The diode was backwards biased with 10 volts and the resultant current was measured; the results are shown in Figure 14. If the voltage was left on and continuous measurements were taken, current steadily increased to several times the original measurement. However, after the voltage was left off for several days, the current returned to the original value. In addition, if the voltage was only turned on to take individual or a short series of measurements, current remained at the original value. A subsequent test of the same diode while dry gave similar results, suggesting that the presence of a saline bath was not the cause of the current drift.

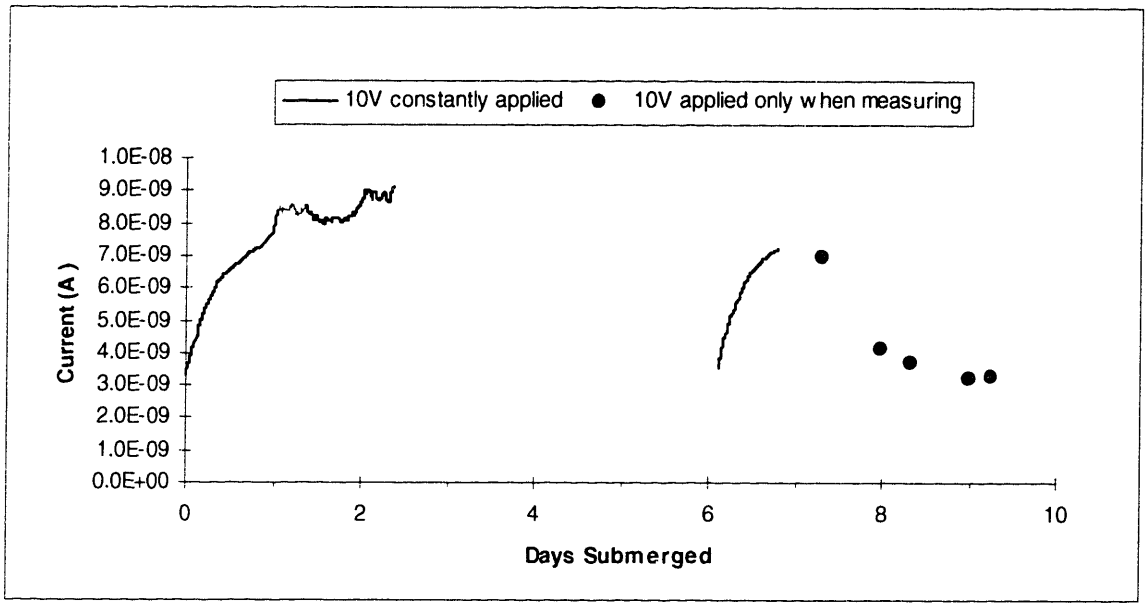

Figure 14: Sealed, encapsulated diode in saline bath

To eliminate this potentially complicated behavior, voltage was only applied to an individual test model while it was being monitored for saline leakage. The first design tested with both polyimide and return wire leakage paths was Model 5, of which two test specimens (5.1 and 5.2) were fabricated. Both were tested in the single chamber shown in Figure 9, though data was recorded manually for model 5.1 and with LabVIEW software for model 5.2. Neither test specimen was kept submerged for very long; model 5.1 was used to

increase familiarity with the operation of the electrometers and shielding techniques, and model 5.2 was used to detect errors in the LabVIEW program and improve data recording. The results for model 5.1 are shown in Figure 15, and the results for model 5.2 are shown in Figure 16.

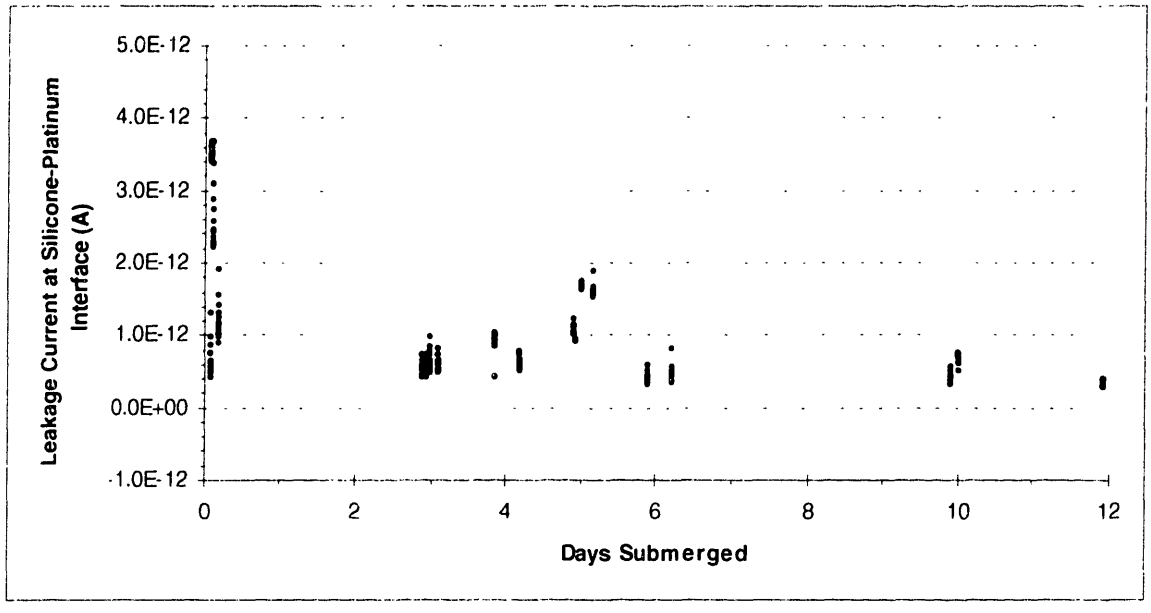

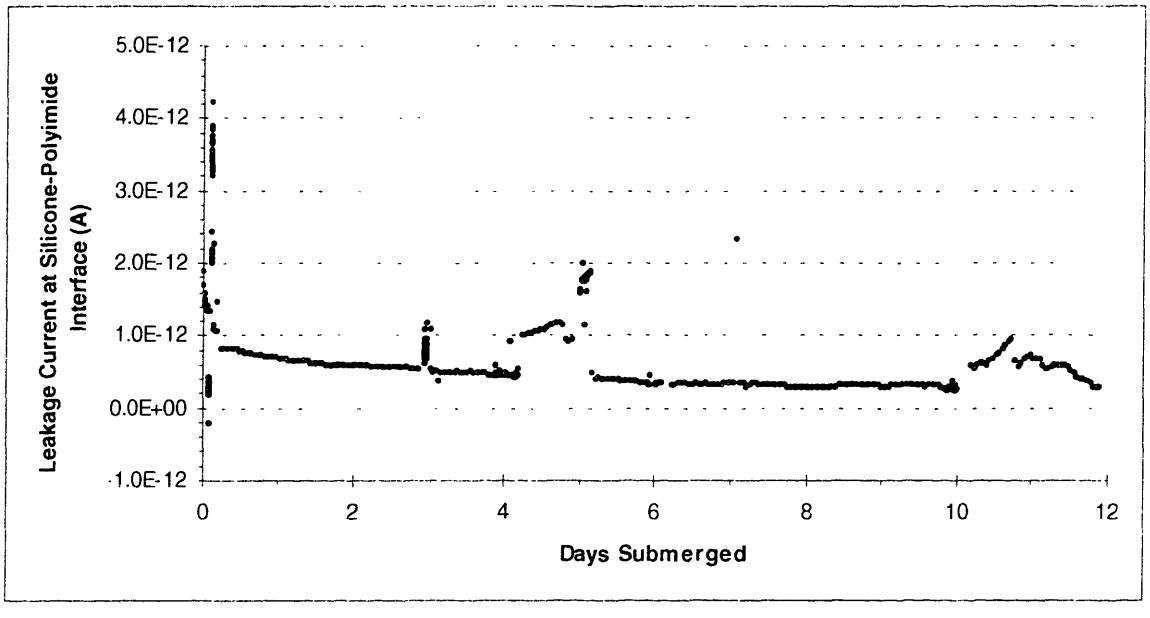

Figure 15: (top) Plot of leakage current at the silicone-platinum interface of Model 5.1. (bottom) Plot of leakage current at the silicone-polyimide interface of Model 5.1. The connection between the saline and the detection wires was an open circuit when no measurements were being made, and 10 volts were applied during recording.

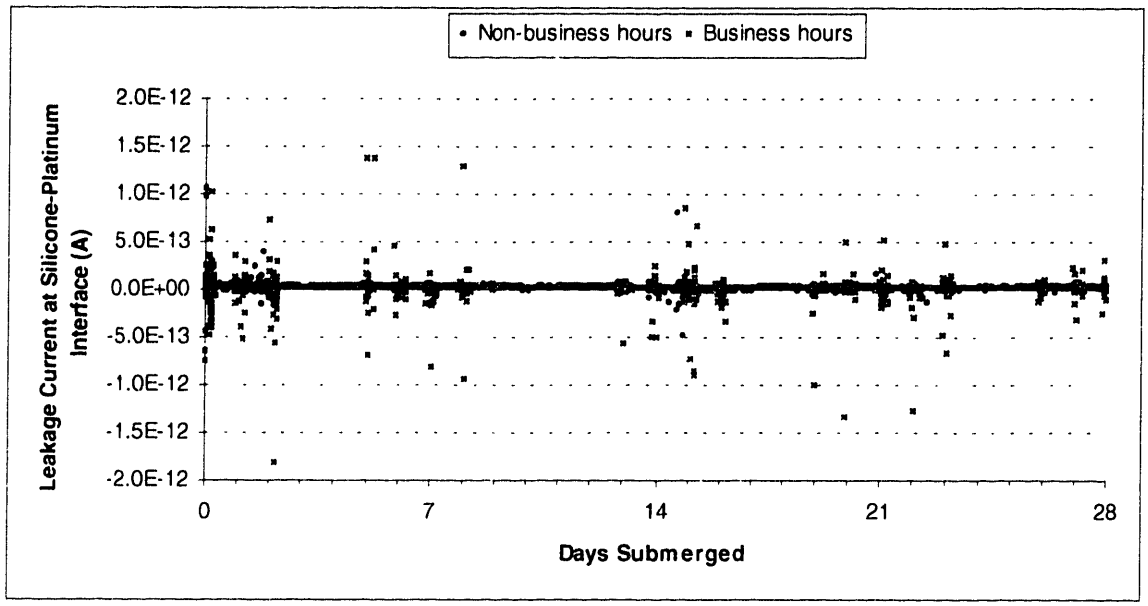

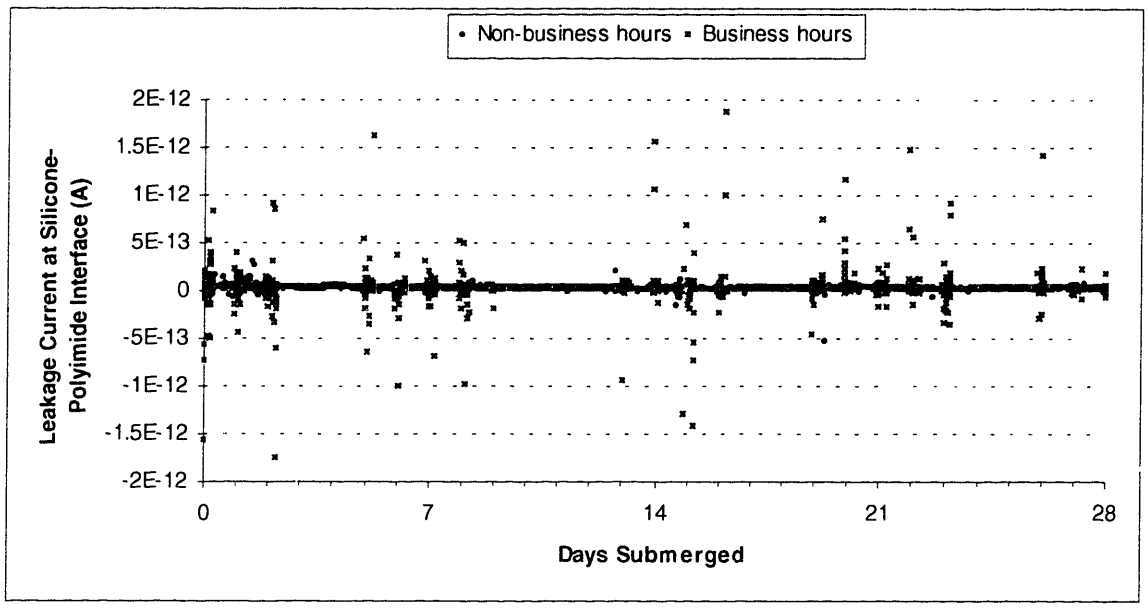

Figure 16: (top) Plot of leakage current at the silicone-platinum interface of Model 5.2. (bottom) Plot of leakage current at the silicone-polyimide interface of Model 5.2. The connection between the saline and the detection wires was an open circuit when no measurements were being made, and 1 volt was applied during recording. Data recorded during "business" and "non-business" hours are differentiated.

It should be noted that in the model 5.2 results, data recorded during traditional business hours are differentiated from data recorded during non-business hours to illustrate the effect of business hour activity on measurement stability.

The results from Model 5.1 show extremely high resistance to fluid leakage. Under 10 volts, currents never went above five picoamps at either leakage path and only once exceeded two picoamps after the first day. This latter current corresponds to a 5×10^{12} Ω resistance to leakage current. The results for Model 5.2 are similar; during non-business hours, when there were minimal external disturbances, leakage currents generally stayed below 0.1 picoamps. Under 1 volt, such currents correspond to a 1×10^{13} Ω resistance to leakage.

The multiple chamber test block shown in Figure 11 enabled simultaneous testing of up to nine test specimens. Five specimens of Model 6 (6.1 through 6.5) were tested in a staggered time frame; three were initially being tested and two more were added later, but each was tested for 60 days. Results for models 6.1 through 6.3 are shown in Figure 17, and results for models 6.4 and 6.5 are shown in Figure 18. An attempt was made during the test to prevent saline evaporation by covering the top of each chamber. The 13 day period during which the covers were in place is designated on the plots in Figure 17 by solid vertical lines. This same period was relatively earlier in the test for models 6.4 and 6.5 and is also designated on those plots in Figure 18. The covers were removed because of the adverse effect they had on the results; relatively stable measurements suddenly became unstable and jumpy after the covers were added. This effect can be observed especially well in the results for the silicone-polyimide interface. The apparent cause of destabilization was condensation of saline on the insides of the covers. The condensate would drip down onto the non-submerged portions of the models and the electronics, creating short-circuits and other problems. Relative stability resumed after the covers were removed. One unusual result to be noted in Figure 18 is the eventual drop in leakage currents at the silicone-Teflon interface around day 40. No explanation for this occurrence is obvious, but corrosion of electrical contacts may have played a role.

Other phenomena which affected the Model 6 results are also indicated by vertical lines on the plots in Figure 18. There was a short period of complete saline evaporation due to a delay in chamber refilling, and the resultant drop in leakage current is clearly seen around day 33. At day 45, the copper rods depicted in Figures 10 and 11 were installed; these rods replaced individual wires which contacted the saline bath, shown in Figure 9. Initially, all nine rods were connected to the voltage source via the large aluminum heating blocks which rested on either side of the test block. However, measurements became slightly

less stable with this configuration, and the copper rods were isolated from the aluminum blocks at day 49. Finally, voltage was increased from one volt to three volts at day 47 to help determine the extent of destabilization caused by the copper rods and aluminum blocks.

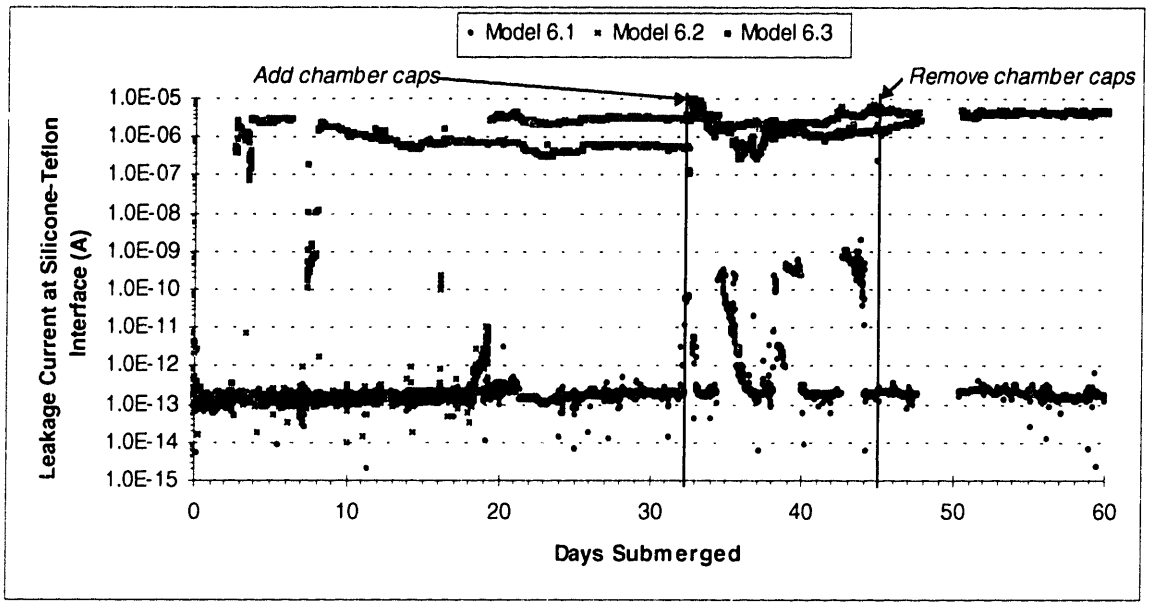

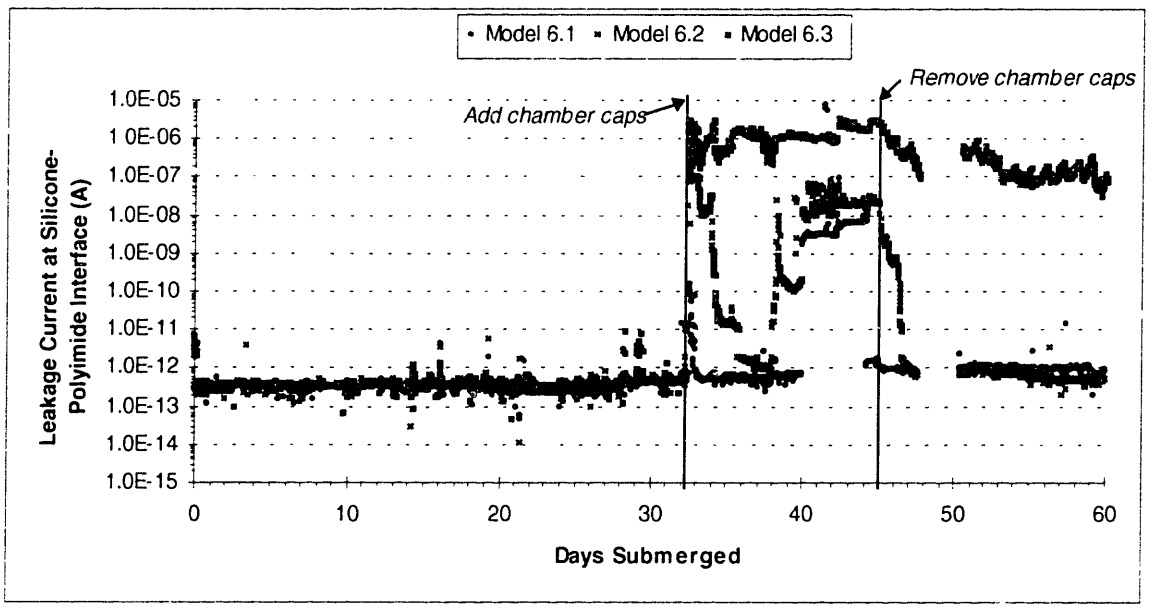

Figure 17: (top) Plot of leakage current at the silicone-Teflon interface of models 6.1 through 6.3. (bottom) Plot of leakage current at the silicone-polyimide interface of models 6.1 through 6.3. The connection between the saline and the detection wires was an open circuit when no measurements were being made, and 1 volt was applied during recording.

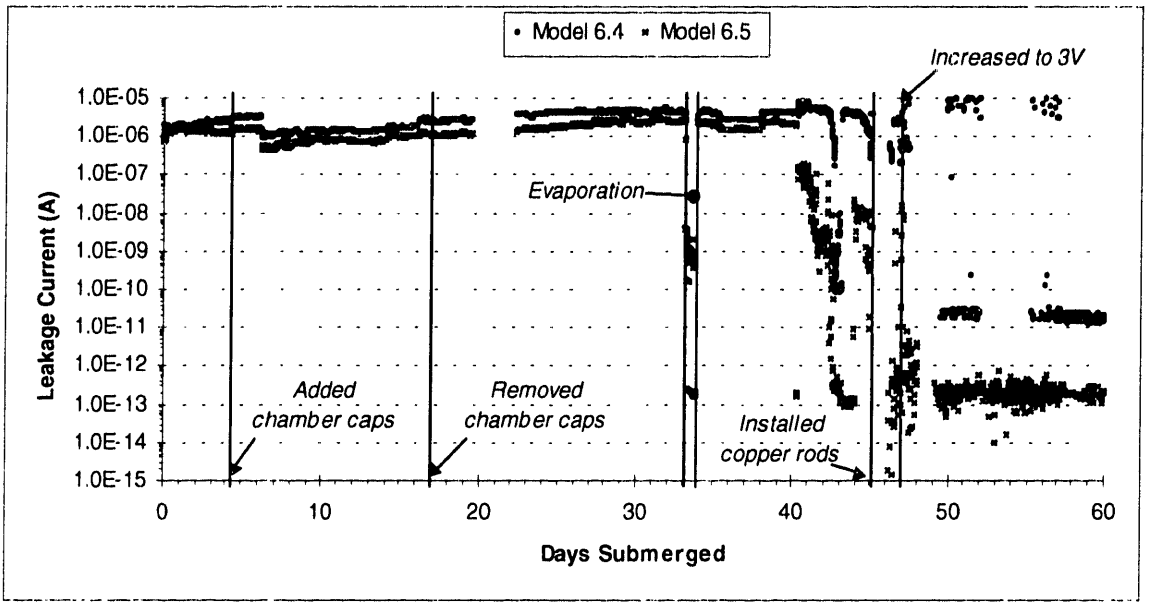

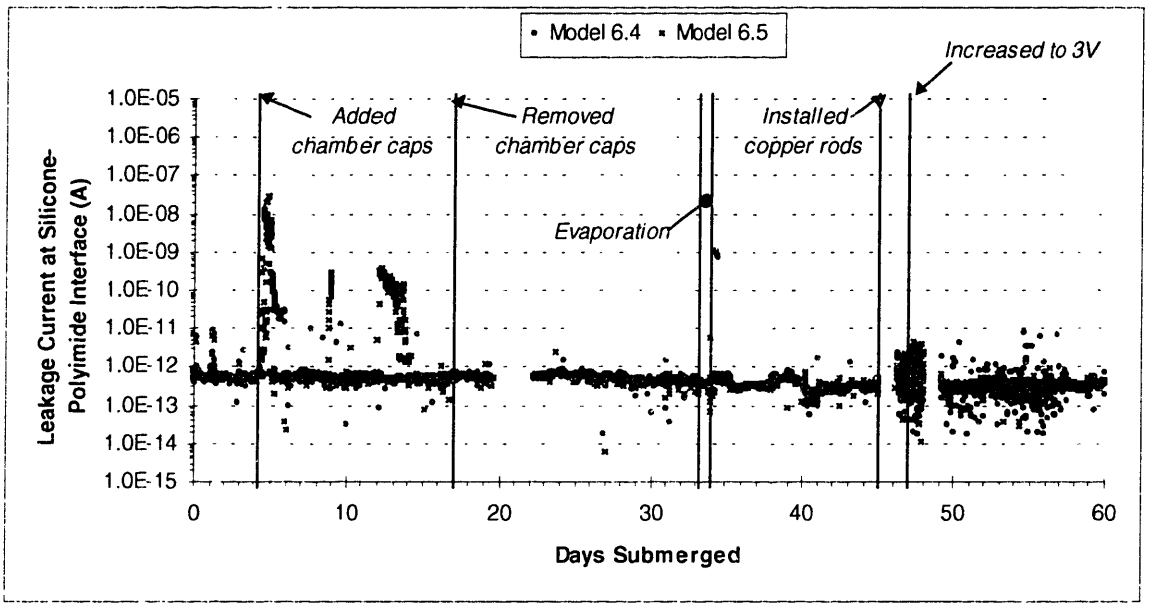

Figure 18: (top) Plot of leakage current at the silicone-Teflon interface of models 6.4 and 6.5. (bottom) Plot of leakage current at the silicone-polyimide interface of models 6.4 and 6.5. The connection between the saline and the detection wires was an open circuit when no measurements were being made; during recording, 1 volt was applied before day 47 and 3 volts were applied after day 47.

It can be seen in the bottom portion of Figure 18 that the range of low current measurements became larger after addition of the copper rods. However, the measurement range narrowed after day 49, when the rods were isolated from the aluminum blocks. Raising the voltage from 1 to 3 volts had no apparent effect.

Models 7.1 through 7.3 were added to the test apparatus partway through the Model 6 tests; these specimens were removed after 20 days due to fluid leakage, as shown in Figure 19.

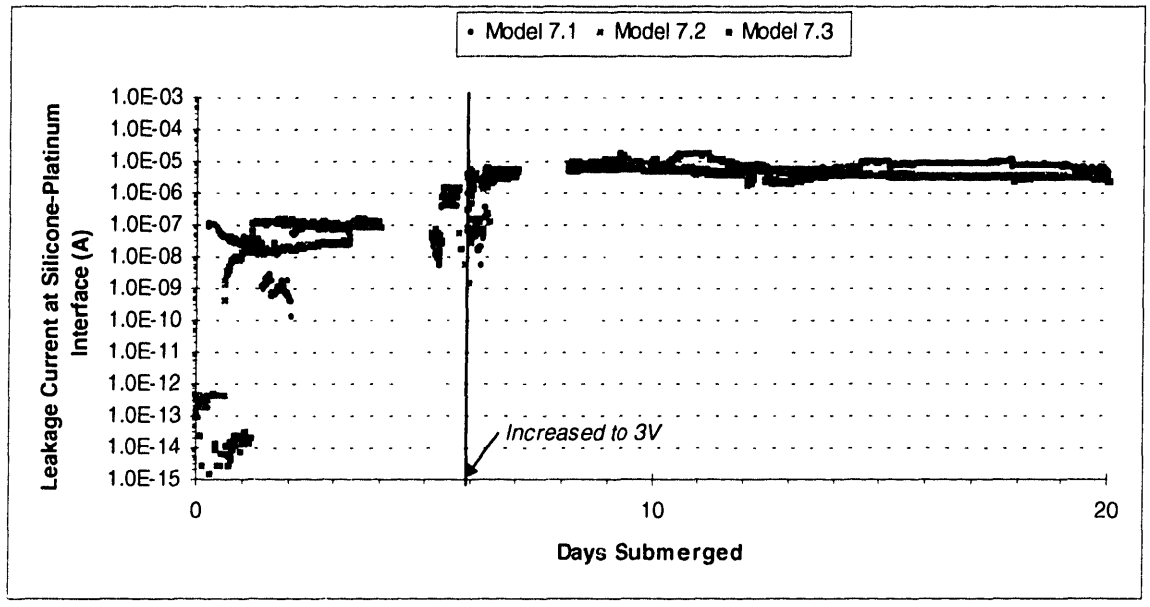

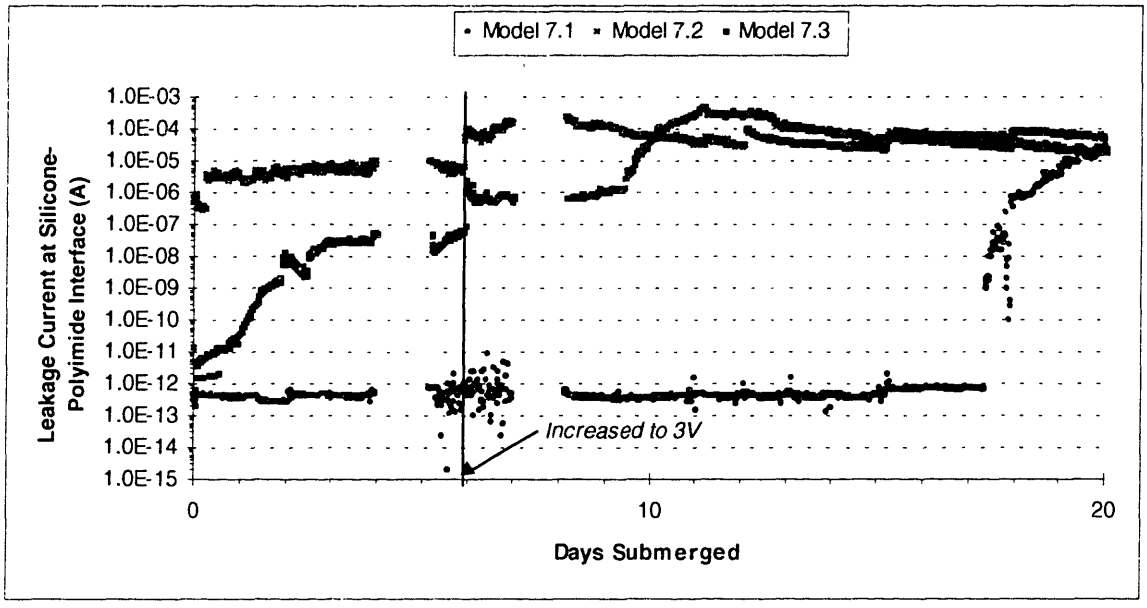

Figure 19: (top) Plot of leakage current at the silicone-platinum interface of models 7.1 through 7.3. (bottom) Plot of leakage current at the silicone-polyimide interface of models 7.1 through 7.3. The connection between the saline and the detection wires was an open circuit when no measurements were being made; during recording, 1 volt was applied before day 6 and 3 volts were applied after day 6.

Because the Model 7 tests overlapped the Model 6 tests, several of the noted phenomena are the same. However, the obviously high leakage currents were not as affected by destabilizing factors; only leakage at the silicone-polyimide interface of 7.1 remained low beyond the first few days.

Four specimens of Model 8 (8.1 through 8.4) were tested alongside four control specimens. The controls had the same features and dimensions as the regular test models, but there were no leakage paths created by polyimide or a return wire; these materials, and the corresponding detection wires, were completely encapsulated. Figure 20 shows a detailed view of the control configuration. It should be noted that all components are the same as those shown in Figure 8, but nothing penetrates the bottom surface of the silicone brick.

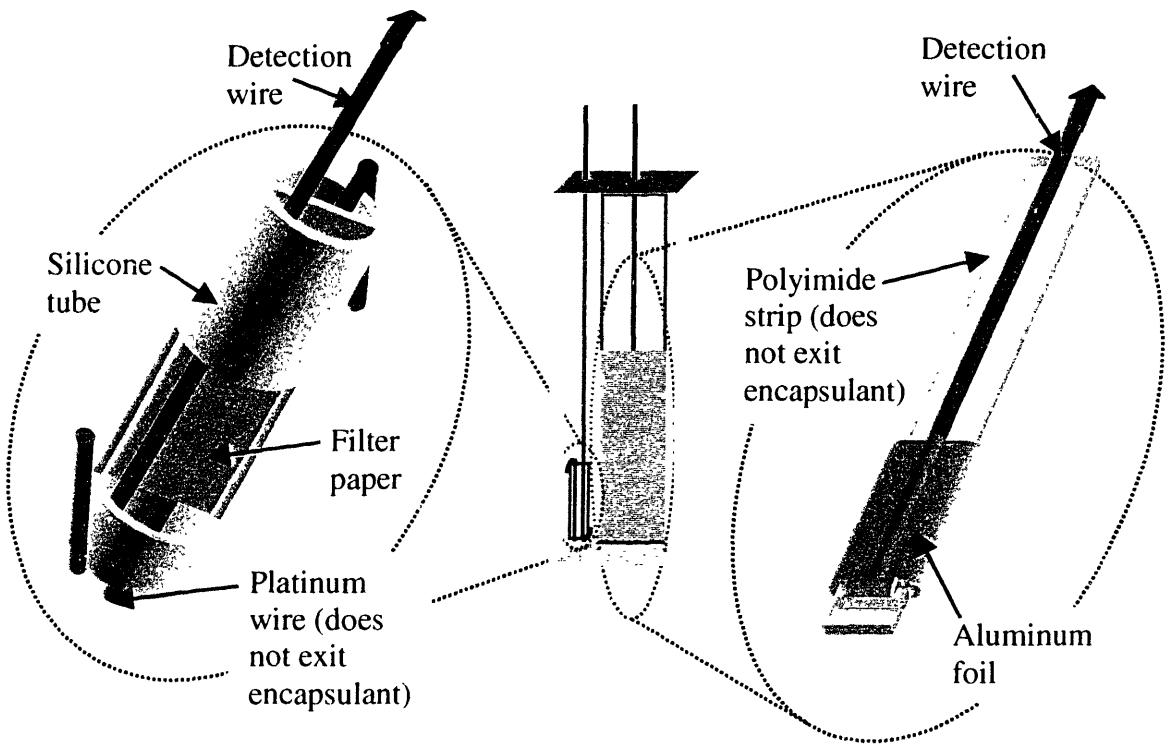

Figure 20: Control version of Model 8, with detailed views of leakage detection components

In addition to the four test specimens and four controls, a short-circuit control was included for the first several days. This control was simply bare detection components, with

no silicone protection, suspended in saline. The saline in the chamber for this control was allowed to evaporate and was then refilled several times to obtain baseline data for the open-circuit and short-circuit currents to be anticipated. The data for all nine chambers are shown in Figure 21. For clarity, the four test models are plotted with a single pattern, the four controls with a second pattern, and the short-circuit control with a third pattern.

It is clear from these plots that the leakage currents at all test model interfaces are higher than those for most of the control model interfaces. The silicone-platinum interface of one control model exhibited saline leakage; closer examination revealed a large air bubble in the silicone through which the detection wire passed. This air bubble may have contributed to the unexpected leakage. In addition, the silicone-platinum interface of another control model exhibited less stable measurements than most other specimens, though the reason is not yet known. When placed in another test chamber, the control model in question behaved the same way. Therefore, the unusual behavior was a property of the control specimen itself, not the test apparatus.

Significant events are again noted by vertical lines on the plots in Figure 21, including an early increase in voltage and the removal of two leaking test models to make room for new specimens. Also, a crude Faraday cage was added to the setup around day 40 in an effort to further shield the test from external disturbances. A small but noticeable increase in stability was achieved after the cage was installed. The effect is most easily seen in the silicone-polyimide control model data; the current measurement range narrows after addition of the cage, and conspicuous peaks in current coincide with times when the cage was opened to add more saline to the test chambers.

The leakage current plots reveal a great deal about the effectiveness of various detection mechanisms the usefulness of silicone as an encapsulant for this prosthesis design, and the evolution of the test apparatus. Further analysis of the data and new experiments planned for the next several months of work will be discussed in Section 2.4.

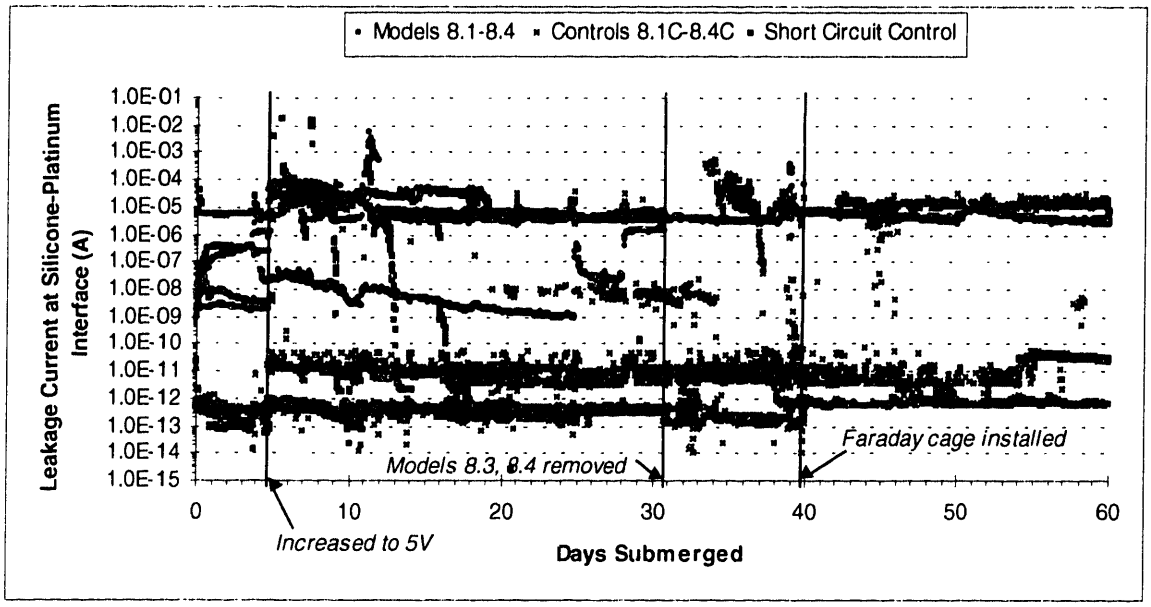

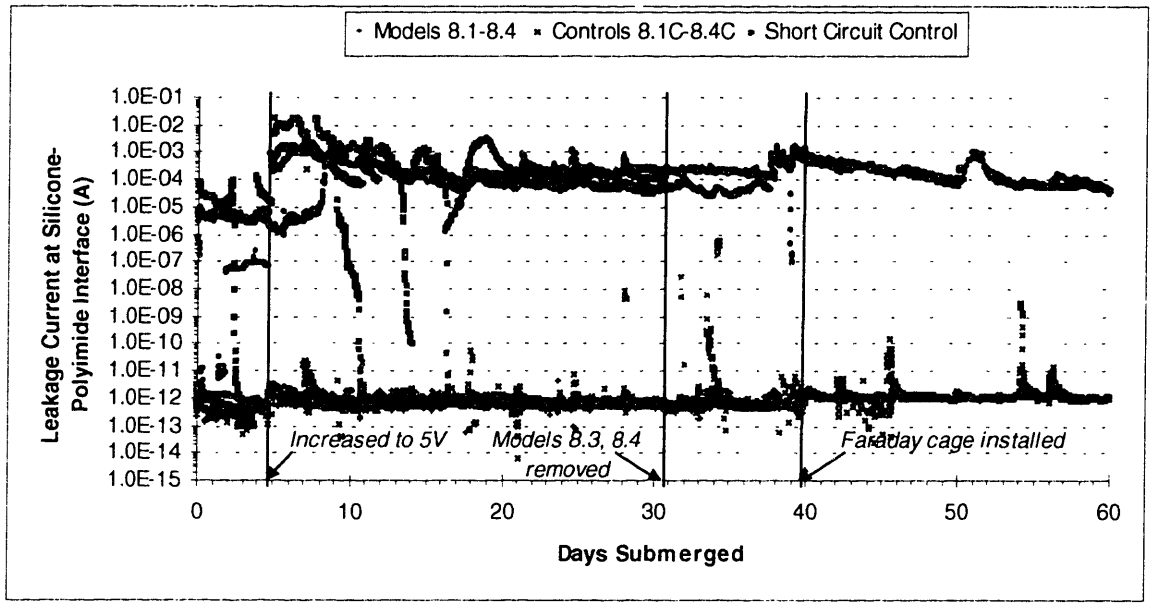

Figure 21: (top) Plot of leakage current at the silicone-platinum interface of models 8.1 through 8.4, as compared to leakage currents for fully encapsulated control specimens. (bottom) Plot of leakage current at the silicone-polyimide interface of models 8.1 through 8.4, as compared to leakage currents for fully encapsulated control specimens. The connection between the saline and the detection wires was an open circuit when no measurements were being made; during recording, 1 volt was applied before day 4 and 5 volts were applied after day 4. Two test models were removed after 30 days under soak.

2.4 Conclusions and Future Directions

Survival of the implanted electronics in the eye for 60 days will allow useful, *in vivo* testing of a complete, functioning implant in animals. Therefore, the current testing protocol is designed to check models for failure within 60 days of submersion in saline. In previous studies on insulating biomaterials, devices that exhibited less than 10^{10} Ω resistance to leakage current were considered to have failed [11]. However, in a more recent NIH Request for Proposal on insulating biomaterials, failure was defined as leakage currents greater than 5 picoamps at potentials of plus and minus 5 volts, corresponding to resistances less than 10^{12} Ω [14]. Using a combination of these criteria, the results presented in Section 2.3 are analyzed in Figures 22 and 23.

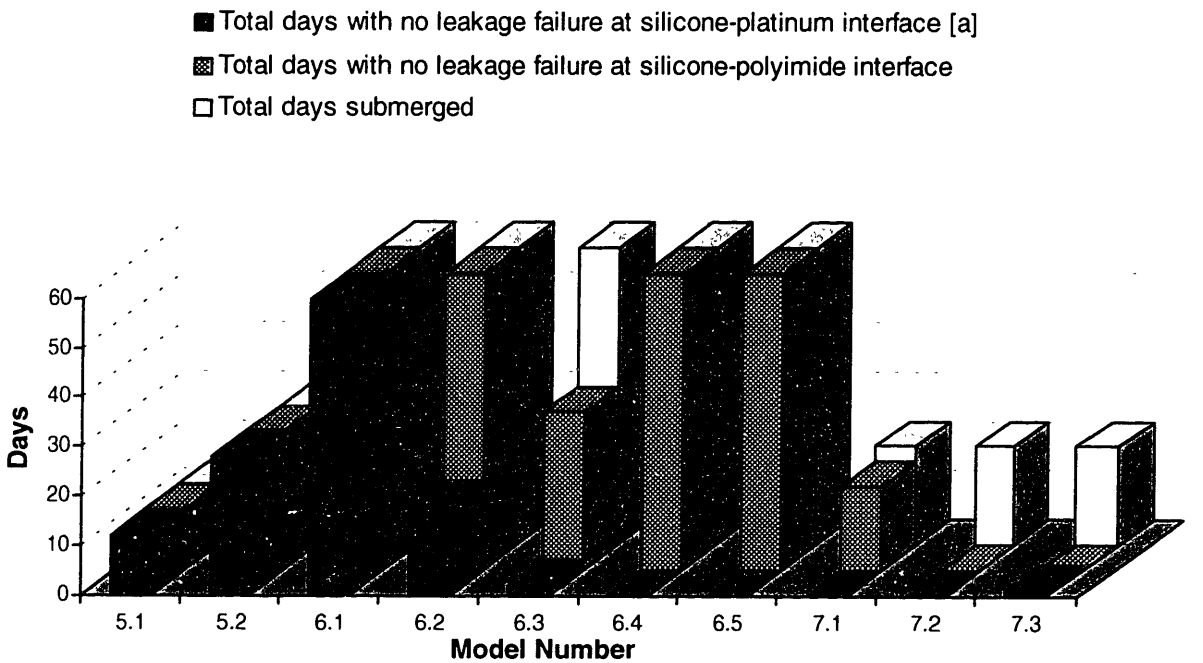

Note: [a] Models 6.1 through 6.5 had a Teflon insulated wire, and thus a silicone-Teflon interface.

Figure 22: Analysis of leakage failure for Models 5, 6, and 7

Figure 22 summarizes the results for Models 5, 6, and 7; as discussed in Section 2.1, these designs were all steps in the development of Model 8. Both the silicone-polyimide and the silicone-platinum interfaces of models 5.1 and 5.2 exhibited no leakage failure for as long as they were tested in saline. However, qualitative examination of the two specimens revealed poor bonding at both interfaces, making the test results questionable. Models 6.1

through 6.5 were tested with a silicone-Teflon interface that had a more reliable configuration for leakage detection and that was more likely to exhibit leakage. As shown by the five columns for Model 6 in Figure 22, leakage failure at this interface was indeed observed. All but one specimen exhibited saline leakage at the silicone-Teflon interface within 18 days. However, only one specimen, model 6.3, exhibited leakage failure at the silicone-polyimide interface, and it occurred quite suddenly at day 32. The results shown in Figure 17 reveal that day 32 is exactly when covers were added to the test chambers. As discussed in Section 2.3, the covers allowed evaporating saline to condense on top of the models, severely affecting measurements. Most currents resumed at pre-cover levels after the covers were removed, but model 6.3 remained affected. It is not known whether this high current was due to actual leakage failure or another problem with the model.

The results for polyimide were still questionable, and Model 7 was designed to allow more reliable leakage detection at both the polyimide and a bare platinum wire. As shown in Figure 22, leakage currents were very high at almost all interfaces in the Model 7 specimens from the first day of testing. Models 7.1 through 7.3 were only tested for 20 days, having quickly exhibited saline leakage and then used to further improve the LabVIEW setup.

Based on the results and designs of these 10 specimens, Model 8 specimens and controls were fabricated and tested. The results shown in Figure 21 are summarized in Figure 23. In analyzing the data, the majority of leakage failures corresponded to resistances well below 10^{10} Ω, and the majority of non-failures corresponded to resistances well above 10^{12} Ω. However, the results for the silicone-platinum interface of control 8.1C were relatively unstable, and its leakage resistance hovered around the 10^{12} Ω level throughout the test. Relative to the leakage levels of the test models, however, this control was still deemed non-leaky. As discussed in Section 2.3, another control model exhibited leakage at the silicone-platinum interface, but this anomalous result was most likely due to imperfect encapsulation during fabrication of that particular model.

No more than a brief comparison of the control model results on the right half of Figure 23 with the test model results on the left half is necessary to draw conclusions about silicone rubber as an encapsulant. Clearly, silicone can protect circuitry from a saline bath when that circuitry is completely encapsulated, confirming results from prior studies [11]. However, the silicone does not bond well enough to either platinum wire or polyimide to create a leak-proof seal where those materials penetrate the protective capsule.

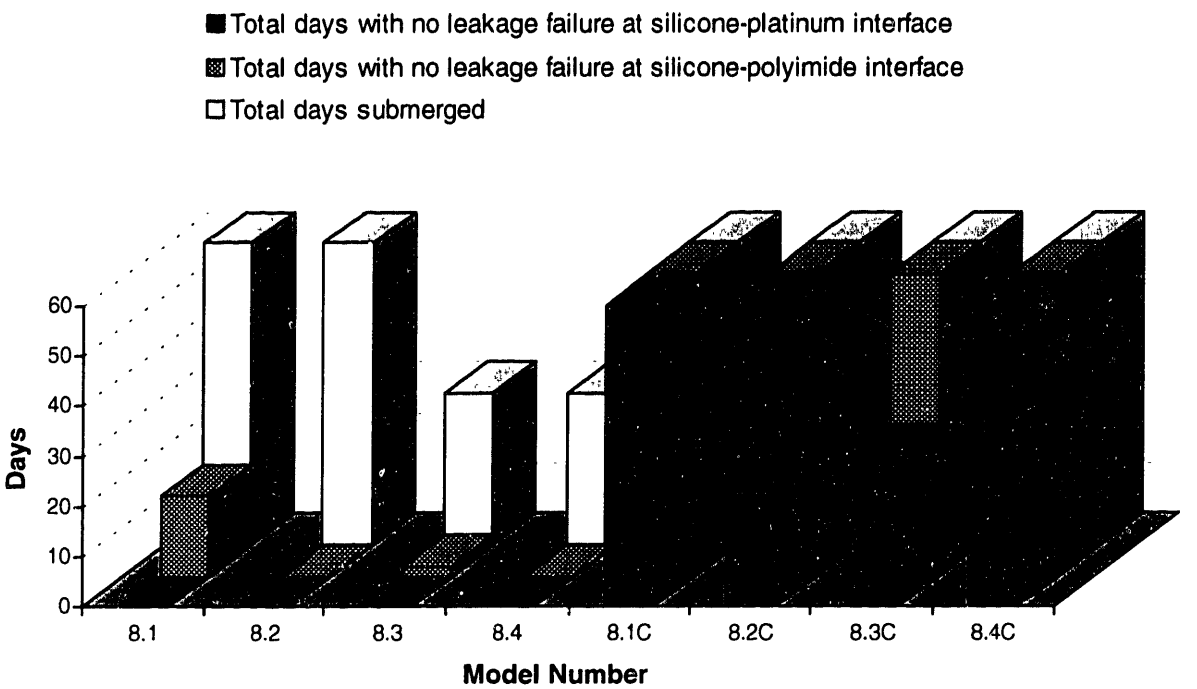

Figure 23: Analysis of leakage failure for Model 8 (8.1 through 8.4) and Model 8 controls (8.1C through 8.4C)

This particular implant configuration, first presented in Figure 2 and modeled in Figure 3, did not survive the minimum 60 days *in vitro* and will therefore not be useful for *in vivo* tests. However, a reliable, effective testing protocol and apparatus have been established, and alternate encapsulation techniques can be evaluated in the coming months. There are several approaches to improving hermetic sealing at the vulnerable electrode array and return wire feedthroughs. First, new encapsulating materials that bond more effectively to polyimide and platinum and meet the other requirements for this implant can be tested. Alternatively, materials with which the silicone will exhibit improved bonding can be used in place of polyimide and platinum. Combinations of these two techniques are also possible. In addition, a non-polymer encapsulation method, while potentially difficult and expensive, may prove the most effective.

Studies have shown that certain epoxies may be effective encapsulants, and there are many medical grade, optically transparent epoxies available [15]. Testing such materials requires minimal modification to the model fabrication procedures developed in this thesis, so preliminary samples have already been put under soak. Model 9 is essentially the same as Model 8, but a commercially available epoxy (2-Ton Clear Epoxy, Devcon, Danvers, MA)

was used as the encapsulant. Two specimens, models 9.1 and 9.2, replaced the two model 8 specimens which were removed partway through the most recent tests The results are shown in Figure 24.

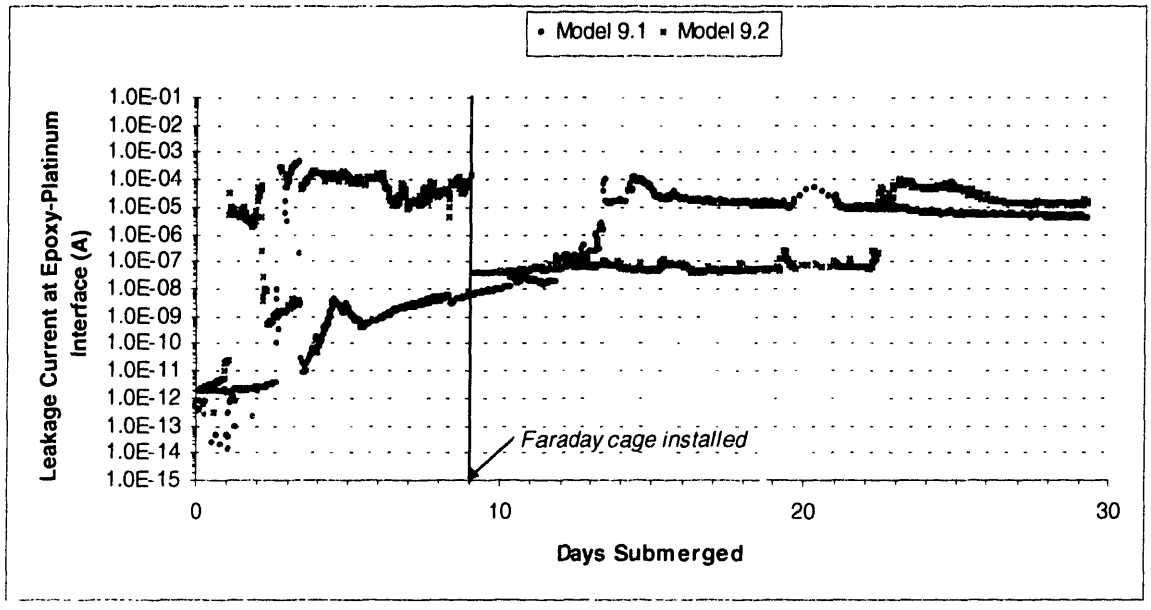

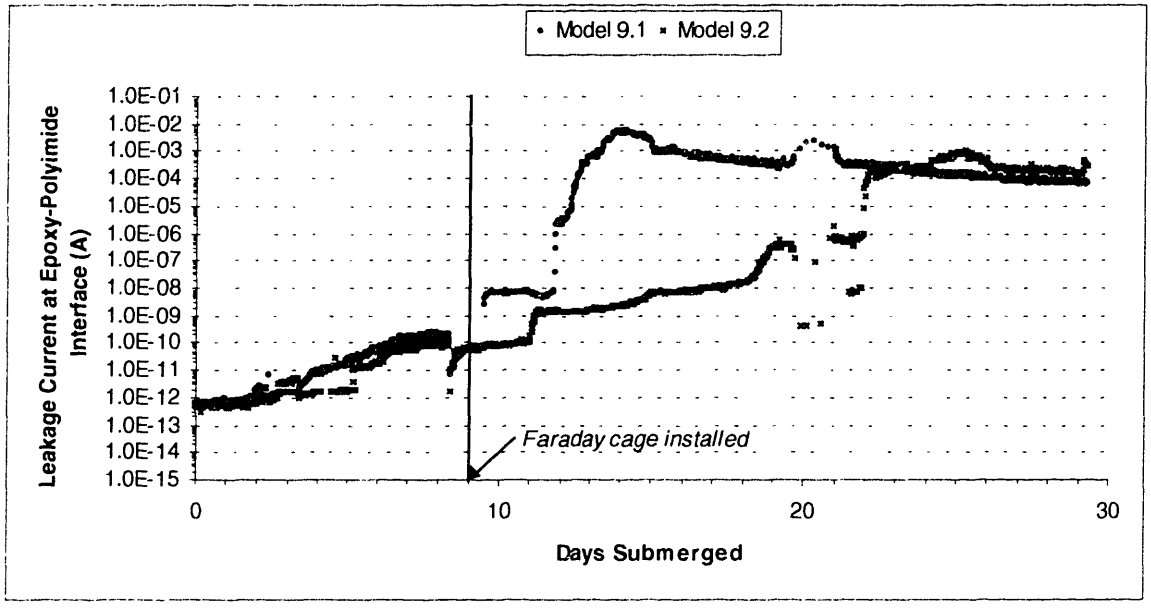

Figure 24: (top) Plot of leakage current at the epoxy-platinum interface of models 9.1 and 9.2. (bottom) Plot of leakage current at the epoxy-polyimide interface of models 9.1 and 9.2. The connection between the saline and the detection wires was an open circuit when no measurements were being made, and 5 volts were applied during recording.

While analyzing the results in Figure 24, it is important to note that models 9.1 and 9.2 were fabricated quickly; less care was paid to removing air bubbles from the epoxy material before molding the models than was exercised during silicone model fabrication. The results may therefore not fully reflect the potential effectiveness of epoxy as an encapsulant.

Leakage failure was observed at the epoxy-platinum interface between two and three days after submersion in saline. Failure was also observed at the epoxy-polyimide interface; by the 10^{12} Ω criteria, this failure occurred around day 4, and by the 10^{10} Ω criteria, it occurred around day 11. However, it is the trend of the leakage current data, not the day of failure, that is more relevant in these results. In most of the silicone encapsulant data, failure occurred relatively quickly and created a step-like pattern in the leakage current data. However, leakage failure occurred more gradually with the epoxy encapsulant, suggesting that at least some bond existed and was then progressively broken down. Eventually, leakage current levels steadily increased to the same extremes observed in some of the silicone encapsulation data, but not before a relatively longer period of submersion had passed. This behavior is a definite improvement over that of the silicone models and prompts further investigation of more sophisticated epoxies.

Previous studies have been undertaken with other polymers as encapsulants, including vapor deposition polymers and certain combinations of multiple polymers [16, 17]. These techniques are either more expensive or more bulky than epoxy encapsulation, but are still possibilities should other methods fail. In addition, it may be interesting to test polyimide itself as an encapsulant for relatively short periods [18]. It seems reasonable to assume that a more effective bond to the polyimide strip would be achieved, although leakage through the polymer itself would be a concern. Also, a novel glue that is able to bond polyimide to the retina may make an effective encapsulant [19].

Previous studies have also shown that silicone bonds very effectively to silicon, partially explaining its effectiveness in completely encapsulating etched circuit boards [11, 12, 20]. Indeed, an early qualitative study with the silicone used throughout this thesis and a clean piece of a silicon wafer revealed very strong bonding. Currently, the polyimide is being used because our research group has extensive experience working with it in microfabrication, but it should be possible to fabricate the electrode array on a very thin silicon ribbon. Currently, silicon ribbons are being produced at the Cornell University

Nanofabrication Laboratory specifically for use in our hermetic encapsulation test models. Leakage detection components will be fabricated directly on the silicon ribbons, as shown in Figure 25. By eliminating the possibility of any gap between the silicon and detection wires, these components will be even more reliable than those used in Model 8. Also, a complete path from the saline bath to the wires will not be necessary to increase leakage currents, but merely enough fluid to create a short circuit between two fingers of the interlocking design. Similar options are available for improving the return wire; other metals may bond to silicone more effectively than platinum. Specifically, metals which form oxides, such as chromium, have been shown to bond much better with silicone than noble metals like platinum [20].

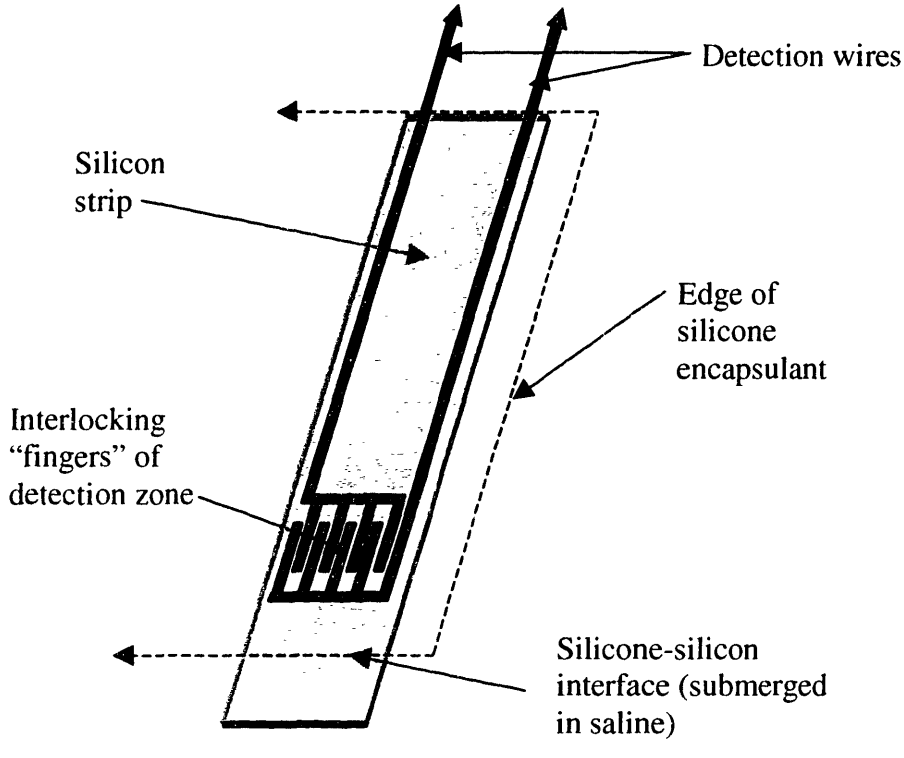

Figure 25: Silicon test ribbon with improved leakage detection components for encapsulation with silicone

Use of a non-polymer encapsulant is also possible. An ongoing NIH funded study at the University of Michigan is currently investigating glass packages with feedthroughs for hermetic encapsulation [21]. A glass capsule is electrostatically sealed to the silicon substrate that the electronics occupy, and feedthroughs are built onto the substrate itself. The package design requirements include optical and RF transparency and volumes of 10 to 100

cubic millimeters; the implant design being studied in this thesis requires approximately 5 cubic millimeters. Using accelerated testing procedures, the Michigan team has had success protecting electronics for the equivalent of several hundred years. A more complex and expensive process would be necessary to implement such encapsulation, but the results could be highly effective.

In addition to the necessary encapsulation improvements, several improvements can be made to the test apparatus. Currently, it requires maintenance about twice per week, and it can support up to nine test models for unlimited periods of submersion. However, even less maintenance would be necessary if saline evaporation can be slowed or stopped altogether. Sealing the test models in the test chambers with airtight covers may be one solution, though leaking models would not be as readily exchanged for new specimens. Also, the switch system being used can support an additional ten sets of inputs, so the entire apparatus can be easily expanded to support more models. Such an expansion will be necessary when more extended, statistical tests are being run. Another possible improvement would be to increase the current saline temperature from 37°C for accelerated testing; increasing the temperature by only several dozen degrees Celsius is enough to increase the equivalent test time by dozens of years. This technique was employed extensively in previous biomaterials studies, and it will be useful when more extended tests are warranted [20, 21, 22, 23]. The test can be further improved by recording current measurements over a wider range of voltages during each test. These ranges, including negative voltages, can be used to further verify the calculated resistance to current leakage. Finally, the copper rods that connect the voltage source to the saline must be replaced with a material less vulnerable to corrosion, such as platinum. When saline evaporation is slowed such that the saline is not being regularly replaced, excessive corrosion could affect the conductivity of the fluid bath and distort the results.

Chapter 3
Intraocular Support Structure

The circuitry that drives the electrode array on or near the retina will comprise the majority of implanted retinal prosthesis components. In the early stages of the project, this circuitry was intended to rest on the retina itself along with the array, as shown in Figure 26 [4].

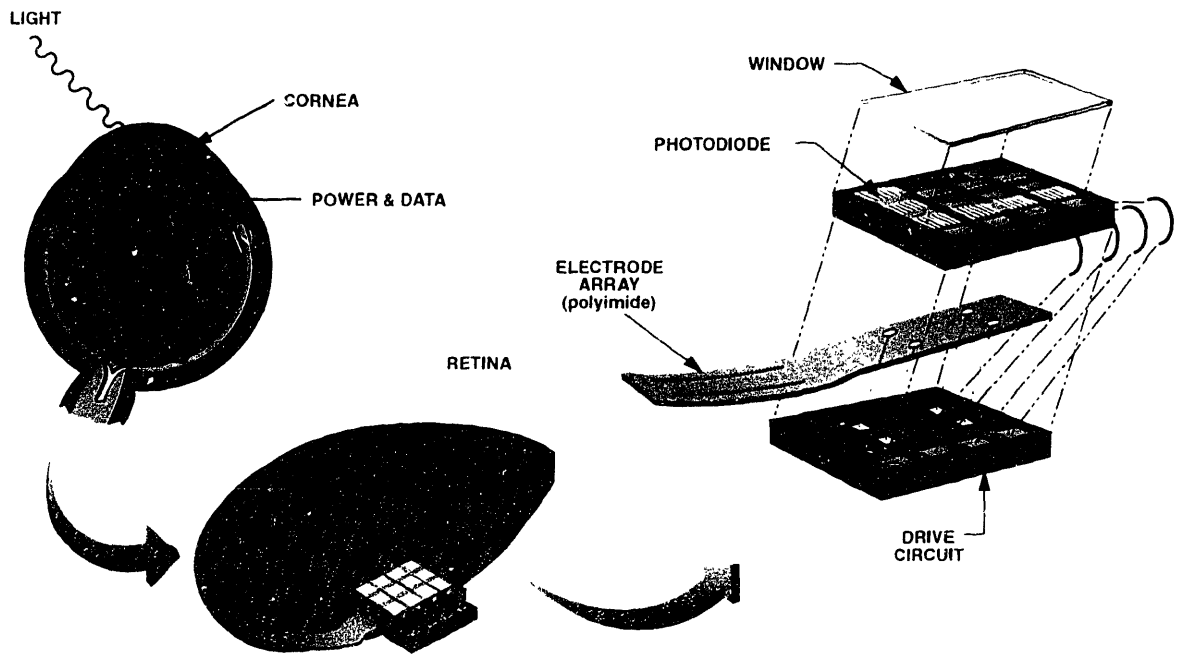

Figure 26: Initial design strategy for placement of implantable electronics

This design prompted concern about the potential mechanical burden on the retina, and plans were made to move the electronics to the front of the eye. A long-term implant is the ultimate goal, and minimizing contact with the retina is an important step towards achieving the necessary biocompatibility.

3.1 Previous Design Philosophy and Development

Moving the electronics to the front of the eye not only decreases the retinal burden, but also makes communication with the photodiode array a more straightforward task and eases limitations on weight. However, without the retina to support the electronics, another anatomical or artificial support structure was required. A modified commercially available intraocular lens (IOL) appeared to be an ideal solution. An IOL is normally used in cataract surgeries, where the natural lens is removed and replaced with a plastic lens. It is implanted through a small incision in the sclera near the cornea, and it is then pushed through the pupil and behind the iris. The IOL is supported behind the iris by two haptics, which are thin, curved pieces of polypropylene or other material. The haptics act as springs that hold the lens in a natural tissue plane just behind the iris and aligned with the pupil. A schematic of its placement in the eye is shown in Figure 27.

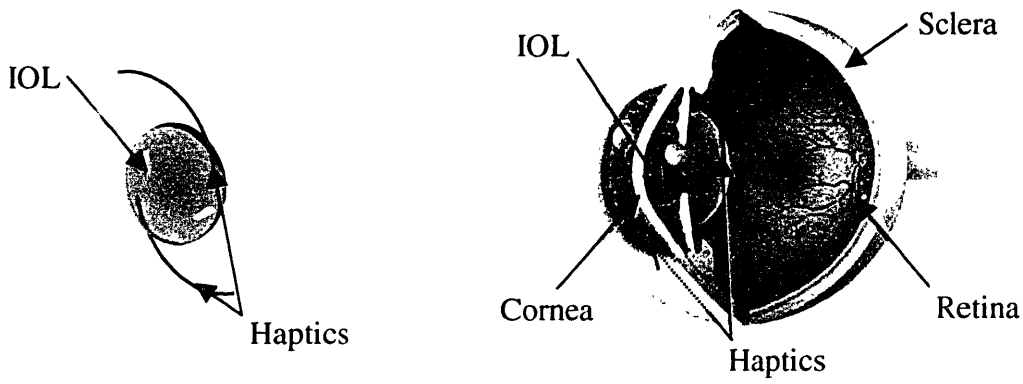

Figure 27: Simplified representation of IOL and its surgical placement in the eye

The earliest use of an IOL for a support structure involved cutting a compartment for the electronics into the lens itself; one such structure, built by Terry Herndon at MIT Lincoln Laboratory, is shown in Figure 28.

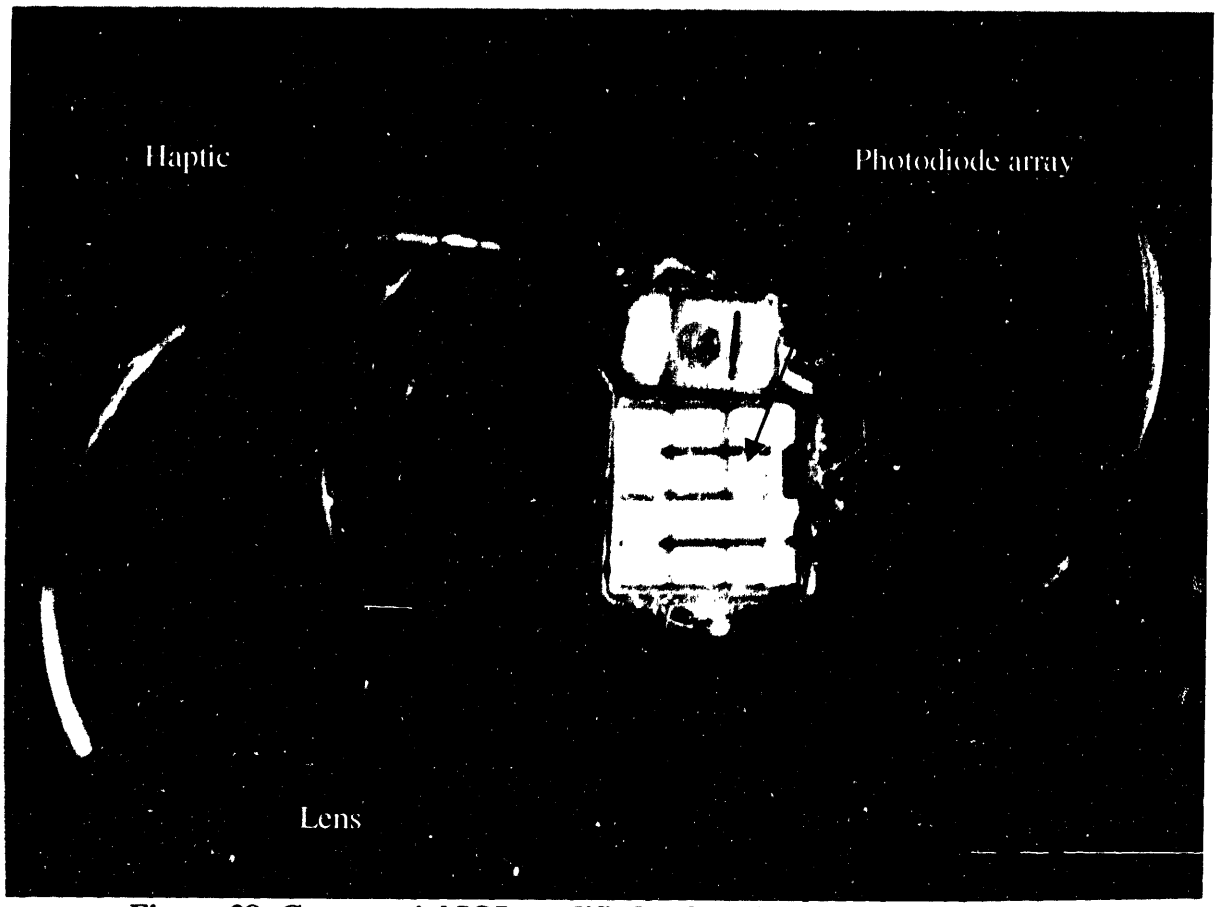

Figure 28: Commercial IOL modified to hold implantable electronics

This technique was expensive and time consuming, requiring otherwise useful IOLs and delicate machining. In addition, once the structure was in place, visualization of the retina was difficult for the surgeon. When the eye was filled with air during one portion of the implant procedure, water vapor would condense on the back of the IOL. Also, the photodiode array covered a significant portion of the lens area, further blocking the line of sight from outside the eye through the pupil.

The next step was therefore to recreate the commercial IOLs inexpensively, removing unnecessary portions of the lens before producing them. The rapid prototyping facilities at the Charles Stark Draper Laboratory, specifically stereolithography, were chosen for this task. In this technique, computer-assisted design descriptions are fed to a SLA-250/40 stereolithography machine (3D Systems, Valencia, CA). Liquid photopolymer resin (Ciba-Geigy SL5170 photocurable epoxy) is then cured by a focused, controllable ultraviolet (325 nm) helium-cadmium laser beam to form successive layers of the part. The technique is diagramed in Figure 29.

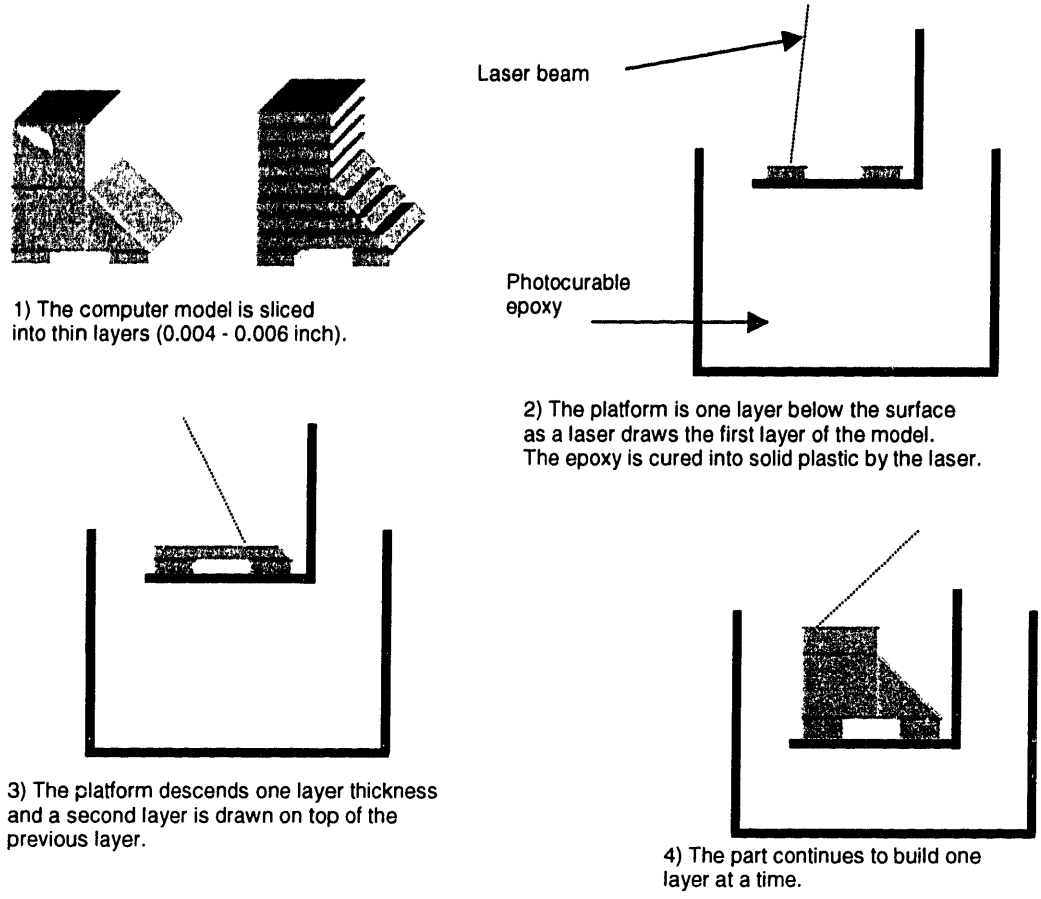

Figure 29: Stereolithography rapid prototyping procedure

With this procedure, prototype support structures could be inexpensively fabricated in minutes. In an early design using this procedure, a commercial IOL was measured and drawn as accurately as possible in Pro/Engineer, a computer design package (Parametric Technology Corporation, Waltham, MA). Portions of the lens not necessary for supporting the implantable electronics were then removed from the drawing, shown in Figure 30. This model, designated Intraocular Support 1 (IOS01), was the prototype in use when design and analysis work for this thesis began.

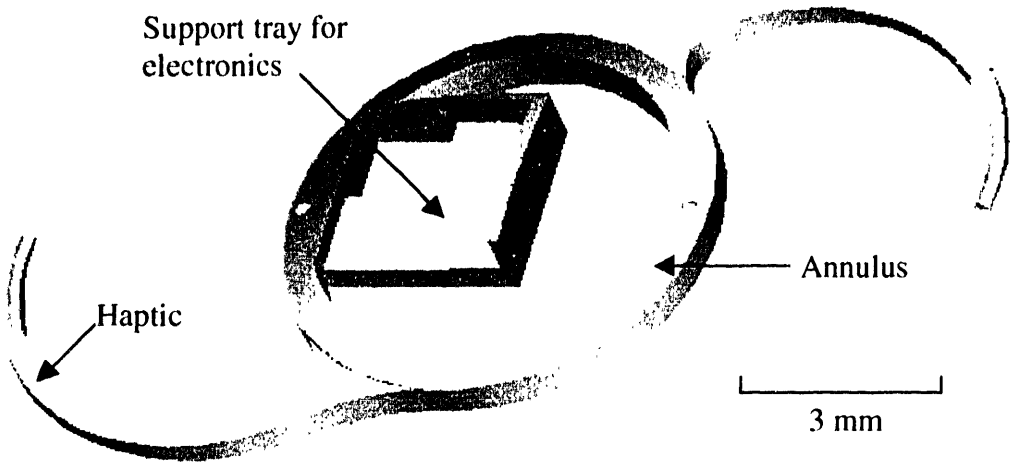

Figure 30: Early support structure design (IOS01) based on an intraocular lens

There were several problems with this initial design. First, the open area inside the annulus was still not sufficient to allow adequate visualization of the retina. Also, the resolution limitations of the stereolithography apparatus (SLA) prevented it from producing extremely small structures, such as the low wall around the perimeter of the support tray. This particular problem also necessitated the rather thick haptic structures, which were not flexible enough for the delicate implant procedure. Therefore, this portion of the thesis work was devoted to modifying the design philosophy and producing a more ideal support structure.

3.2 Iterative Design Philosophy and Development

Through discussions with Dr. J. Rizzo, a set of design requirements for the support structure was developed.

- *Stable support of the implantable electronics behind the pupil:* The laser carrying power and information must have an unobstructed path to the implanted photodiode array, which must in turn maintain a fixed, predictable location.
- *Adequate window for visualization of the retina:* The surgeon must safely manipulate the electrode array near the retina while the support structure is in place. The structure cannot block more than about 25 percent of the pupil area, or it will compromise the surgeon's ability to see the retina and electrode array.
- *Biocompatibility:* The photocurable epoxy used by the SLA is not biocompatible. Therefore, simple structures that can be easily fabricated from biocompatible materials are necessary.
- *Ease of implantation:* The structure must not be significantly more difficult to implant than the intraocular lens used for cataract surgeries.

Using these criteria, the support structure prototypes were designed and rapidly produced in an iterative fashion. Once each issue was properly addressed, plans for the final structure were drawn.

The first iterations consisted of several modifications to the precise drawings previously produced. First, the bulky SLA haptic structures were removed and replaced with simple notches. As discussed in the previous section, SLA fabrication of more delicate haptics was prevented by the resolution limitations of the apparatus; however, notches could be used as support bases for more conventional polypropylene haptics, added after the structure was fabricated. The notches were positioned such that when haptics were installed, the structure could be rotated (clockwise) while in the eye; this arrangement followed the surgeon's preference and made the implantation process more like that of an IOL. In addition, the diameter of the annulus was increased to create a larger window for visualization of the retina. These modifications are seen in design IOS02, shown in Figure 31. To facilitate manufacturing with biocompatible materials, the electronics tray was drastically simplified, as seen in design IOS03.

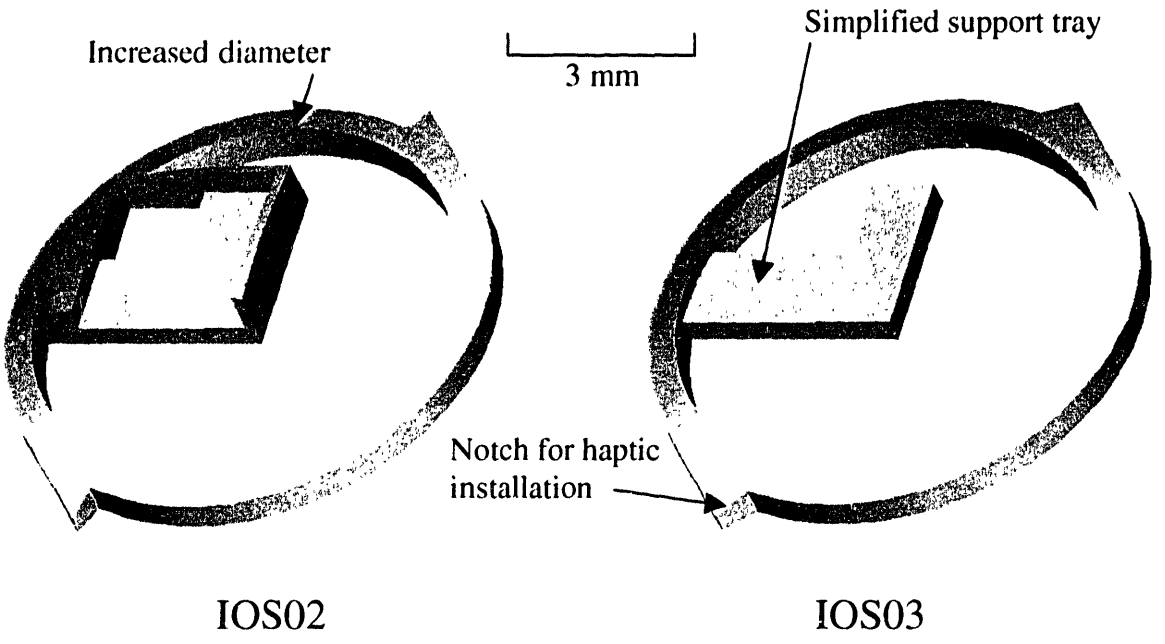

Figure 31: First set of iterative designs for intraocular support structure

These designs were prototyped with the SLA and analyzed for conformity with the design requirements. Design IOS03 was clearly better, but the electronics tray did not adequately support the photodiode array, and the surgeon felt that the open area was still slightly too small. Therefore, designs IOS04 and IOS05 included larger inner diameters and electronics trays which more accurately matched the dimensions of the photodiode array. Both designs, shown in Figure 32, had trays that would leave no part of the photodiode array unsupported. The inner diameter was increased to create more open area inside the ring structure. The main difference between the two designs was the configuration of the electronics tray; one was attached to the ring with two thin support arms and one was attached with one wider arm. In this case, the SLA became a very powerful tool for quickly putting prototypes in the surgeon's hands. Both structures had approximately the same amount of open area, but the one-arm tray design was preferred for its larger portions of continuous open area.

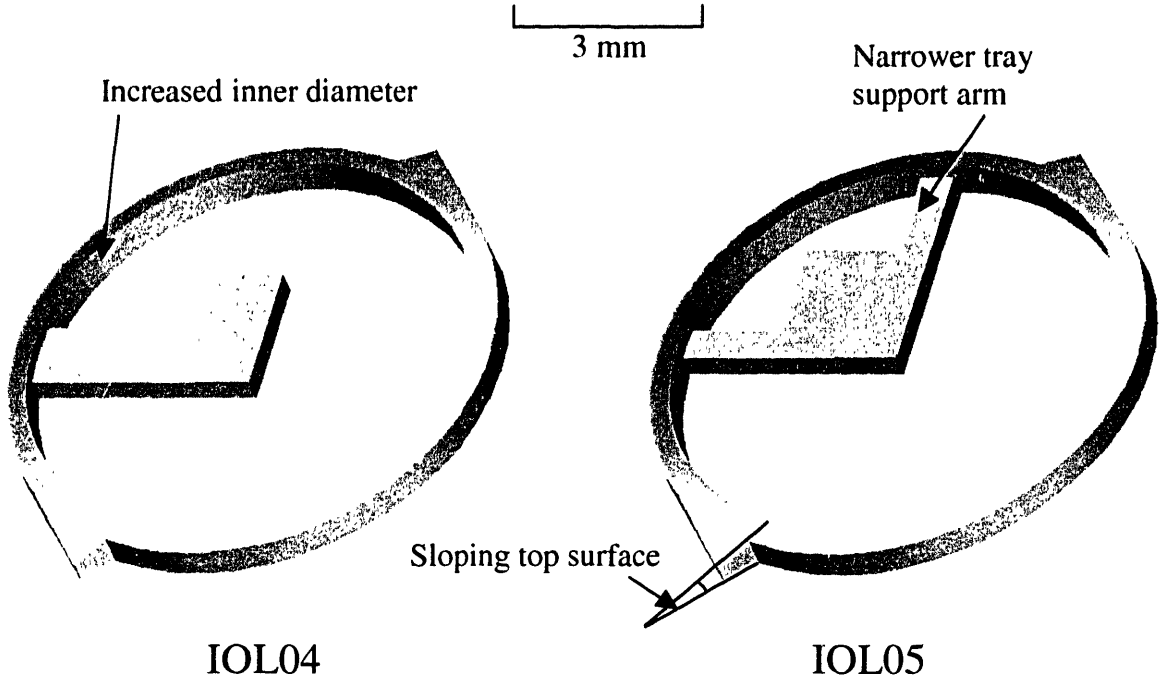

Figure 32: Second set of iterative designs for intraocular support structure. The sloping top surface, a feature of these designs as well as IOS02 and IOS03, is most easily visualized at the exposed face of the haptic notch.

More tray shapes were drawn and rejected in designs IOS06 through IOS08, not pictured. At this stage of design iterations, several new problems became apparent. First, the sloping top surface of the annulus could not be accurately reproduced by the SLA, resulting in a more step-like reduction in annulus thickness from inner to outer edge. This effect made drilling holes in the notches for haptics very difficult and was likely to create later manufacturing problems. Therefore, the slope was reduced in the next set of iterations and eliminated entirely in the final plans. In addition, the structures were being used in animal surgeries for the first time, revealing tray placement requirements that were not previously considered. The electrode array must attach to the ring near one of the haptics; after the electrode array is put in the eye, the support structure can then follow haptic-first in the same way that an IOL is implanted. The necessary configuration is shown in Figure 33. Therefore, the electronics tray was moved to allow proper attachment and configuration of the electrode array. The next set of design iterations, which includes these modifications, is shown in Figure 34.

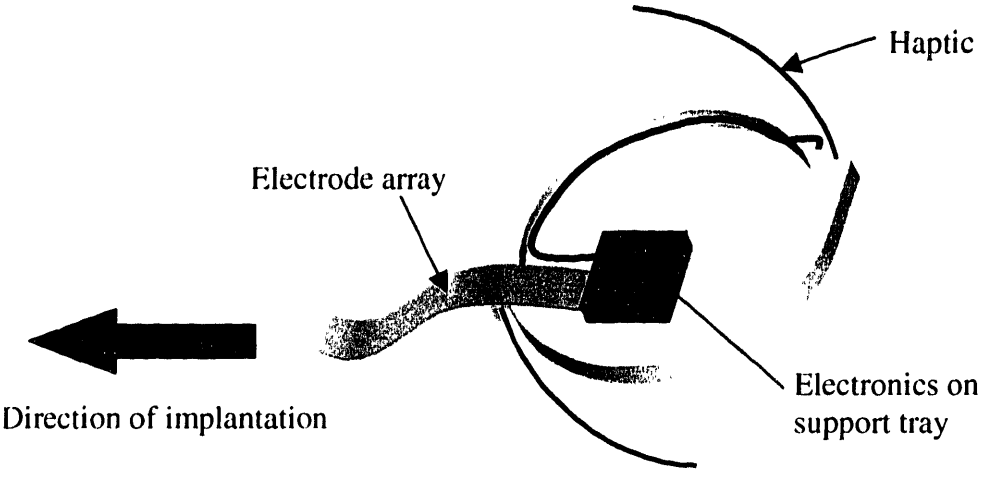

Figure 33: Necessary location of support tray in relation to haptic notch and electrode array for ease of implantation

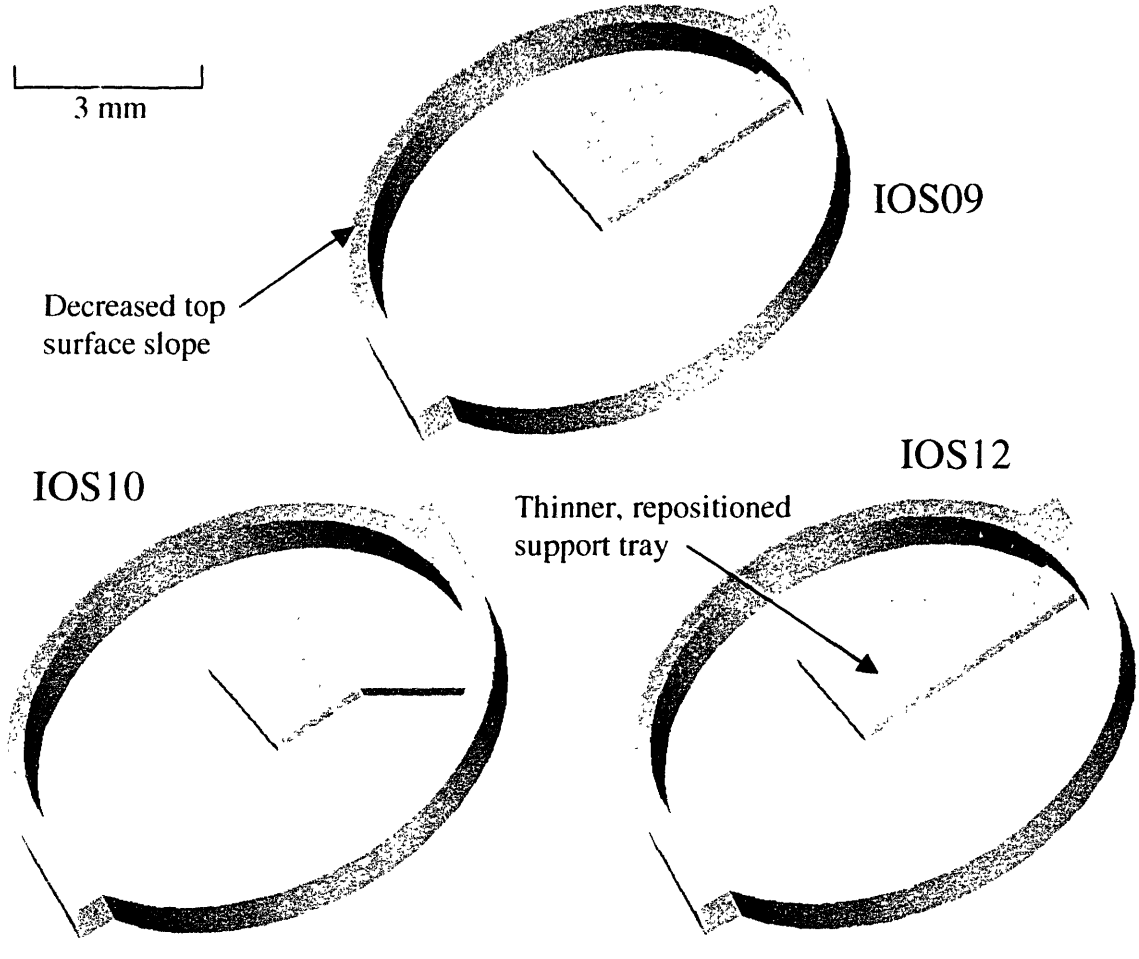

Figure 34: Third set of iterative designs for intraocular support structure

Another modification visible in designs IOS09 through IOS12 is a significantly thinner support tray. This configuration allows the photodiode array to sit lower with respect to the rest of the ring structure, maintaining a more constant profile for ease of implantation. The thinner support tray does not make fabrication from biocompatible materials more difficult, but it could threaten the stability of the tray. Potential tray deflection away from the plane of the ring was analyzed with finite element methods, discussed in Section 3.3.

At this stage of iterations, all design requirements were met from the surgical perspective. The structure could still be implanted like an IOL, and there was sufficient open space to allow visualization of the retina and electrode array. In addition, the design had achieved enough simplicity to enable fabrication from biocompatible materials at relatively low cost. Therefore, the support structure was redrawn without any remnants of the original IOS01 plans, and a biocompatible model was prepared for both finite element and surgical analysis. The final drawing for design IOS14 is shown in Figure 35.

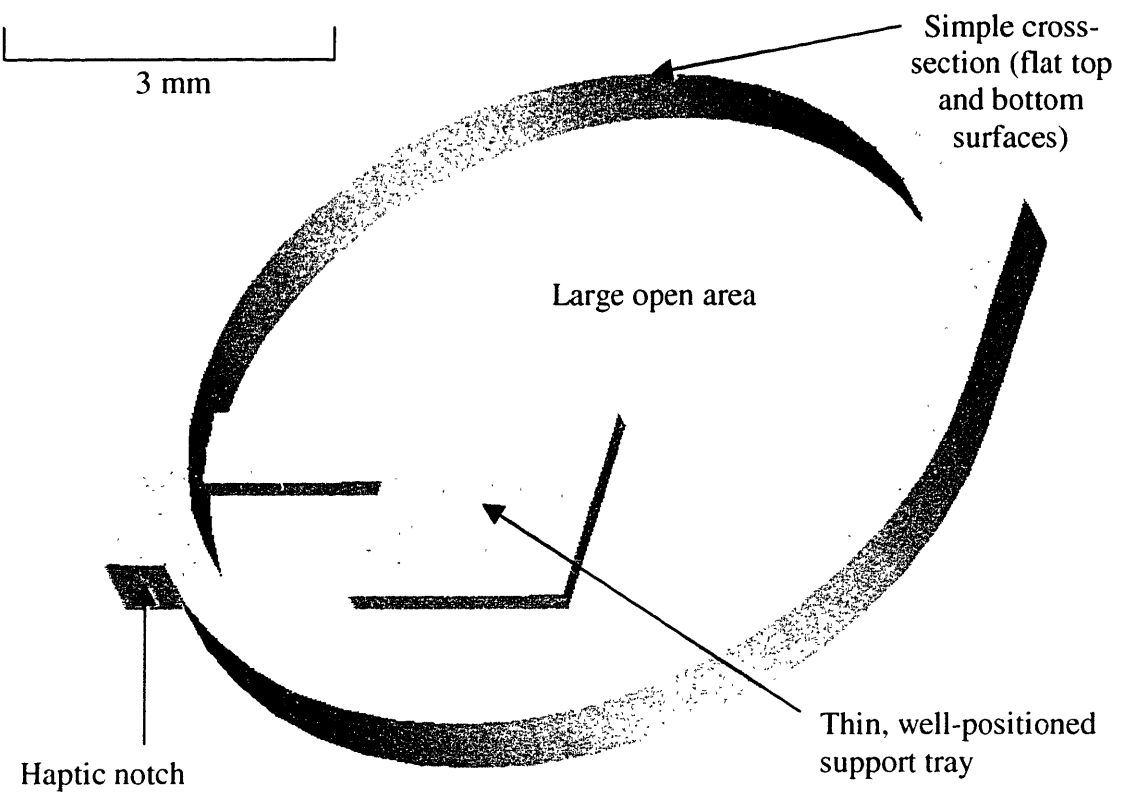

Figure 35: Final iterative design (IOS14) for fabrication from biocompatible material

3.3 Results and Discussion of Finite Element Analysis

Several features of design IOS14 were analyzed with finite element software (ADINA R&D, Inc., Watertown, MA) to help determine its conformity with the remaining design requirement: stable support of the electronics in the eye. One such feature was potential movement of the entire structure relative to the pupil during eye movement: too much movement of the structure could dislodge it from its position directly behind the pupil, disrupting communication with the external laser or damaging the polyimide strip. Although a normal IOL is stable in a moving eye, the weight and configuration of IOS14 could cause problems. Another feature analyzed was potential deflection of the support tray under the weight of a photodiode array or pulling on the electrode array. Again, SLA prototypes did not exhibit this problem, but analysis of other materials was necessary before fabrication of a biocompatible structure. In addition, ease of implantation was addressed, as a support structure fabricated from biocompatible material was likely to behave differently from one made of hard SLA epoxy.

The most significant obstacle to accurate finite element modeling was determination of suitable material constants. The material chosen for initial fabrication was NuSil MED-4940 silicone rubber, as it is easy to mold and is biocompatible. It is also harder than the silicone used in the encapsulation test models, making it more suitable for a support structure. E. Arruda and M. Boyce performed large strain analysis on a commercially available silicone rubber with properties similar to similar to the NuSil silicone [24, 25, 26]. The results of their analysis were curve fitted by Z. Guoxing and W. Shoumei, who determined constants for a constitutive equation of their own derivation. They also showed that these constants could be combined into the first seven constants of a higher-order Mooney-Rivlin material model [27]. Therefore, these seven constants were used to model the rubber using the appropriate dialogs in ADINA. A more detailed explanation of the Mooney-Rivlin material model and the seven constants used is given in Appendix C. The haptics are polypropylene, which was modeled as a linear elastic, isotropic material with a Young's modulus of 1.2 GPa and Poisson ratio of 0.42 [28].

To analyze the stability of the support structure once it is inside the eye, displacement of the structure due to eye movement was calculated. Acceleration of the eye will cause complex motion of the implant, but only the maximum displacement is of interest. The top

portion of Figure 36 shows a simplified representation of the implant. It was assumed that any displacement would be the result of flexion of the thin haptics, not the relatively thick annulus. Therefore, a simple mass-spring model was used to determine a static loading force that, when applied directly to the structure, would produce displacement comparable to the maximum displacement caused by eye acceleration. The static loading condition was then applied to a finite element model of the haptics, and the resultant deflection was analyzed. The mass-spring model is illustrated in the bottom portion of Figure 36; the rigid mass represents the annulus, and the springs represent the haptics.

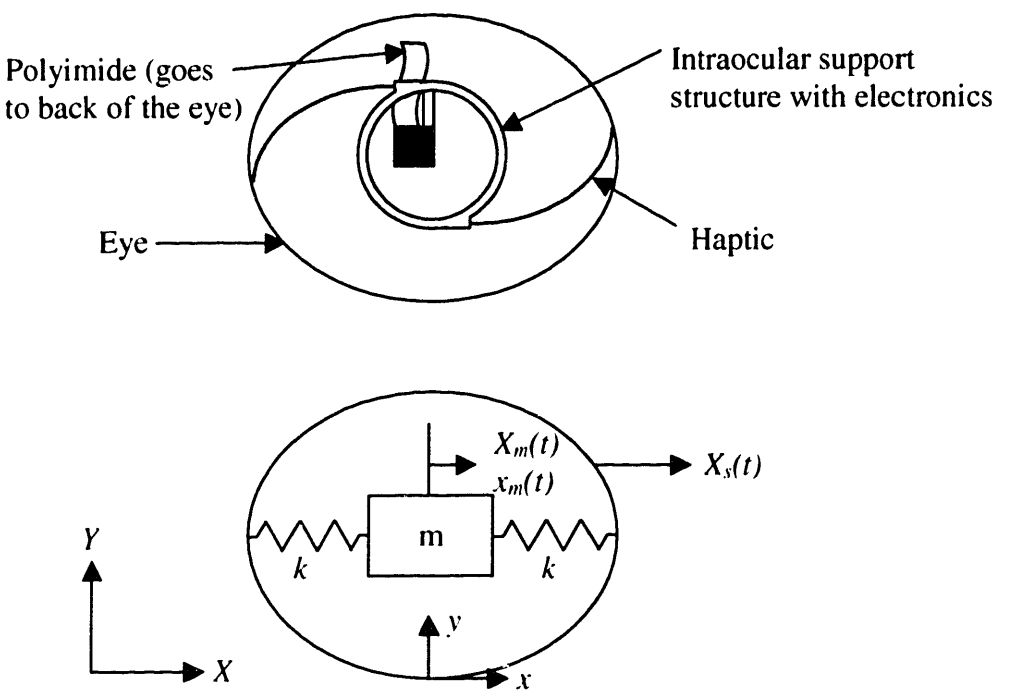

Figure 36: (top) Simplified representation of intraocular support structure supported in eye by haptics. (bottom) Corresponding model used for dynamic analysis, consisting of a mass suspended by springs inside a moving sphere. *X-Y* is the fixed global coordinate system, and *x-y* is a local coordinate system attached to the sphere.

If a static load equal to ma were applied to the mass, it would deflect $ma/2k$ with respect to the sphere. The goal is to compare this deflection to the maximum deflection caused by transient acceleration of the sphere; in this simple undamped oscillator model, the maximum displacement of the mass is simply the overshoot of the oscillation. As indicated in Figure 36, X_m is the position of the mass in the global coordinate system and x_m is its position with respect to the sphere. The position of the sphere is represented by X_s.

With the sphere accelerating, the force on the mass is equal to $m\ddot{X}_m$. The force on the mass due to the stretching and compressing of the springs equals $2k(X_s - X_m)$. Therefore:

$$m\ddot{X}_m + 2k(X_m - X_s) = 0 \tag{3.1}$$

However, noting that x_m equals $(X_m - X_s)$, equation 3.1 can be rewritten in terms of the motion of the mass in the local coordinate system (relative to the sphere):

$$\ddot{X}_m = \ddot{X}_s + \ddot{x}_m \tag{3.2}$$

$$m(\ddot{X}_s + \ddot{x}_m) + 2kx_m = 0 \tag{3.3}$$

$$\ddot{x}_m + \frac{2k}{m}x_m = -\ddot{X}_s \tag{3.4}$$

In the most basic case, $\ddot{X}_s(t)$ equals zero for $t < 0$ and a constant A for $t > 0$, corresponding to constant acceleration of the sphere. The differential equation can be solved by inspection, using initial conditions $x_m, \dot{x}_m = 0$:

$$x_m = \frac{mA}{2k}\left[\cos\left(\sqrt{\frac{2k}{m}}\right)t - 1\right] \tag{3.5}$$

The maximum absolute displacement due to constant sphere acceleration can be found by setting the cosine term equal to its minimum, -1:

$$x_m = \frac{mA}{2k}[-1-1] = -\frac{mA}{k} \tag{3.6}$$

Thus, when sphere acceleration is constant. the maximum absolute displacement of the mass with respect to the sphere equals exactly twice the displacement due to the corresponding static load on the mass. If the eye followed such a simple acceleration pattern, deflection of

the haptics could therefore be analyzed by applying a load equal to 2× the implant mass times eye acceleration.

In fact, the eye follows a more complex velocity profile than constant acceleration. Equation 3.4 was solved numerically for several of these more complex profiles, shown in Figure 37. Angular velocity of the eye peaks at approximately 900 degrees/second for humans, and the eye travels for a few hundred milliseconds during a saccade [29]. Using anatomical data from G. Wyszecki [30], a tangential velocity was derived; the maximum velocity used was 0.11 meters per second, travel time was 0.500 seconds, and the mass of the implanted structure was measured to be 0.0274 grams. Each velocity profile followed these general parameters.

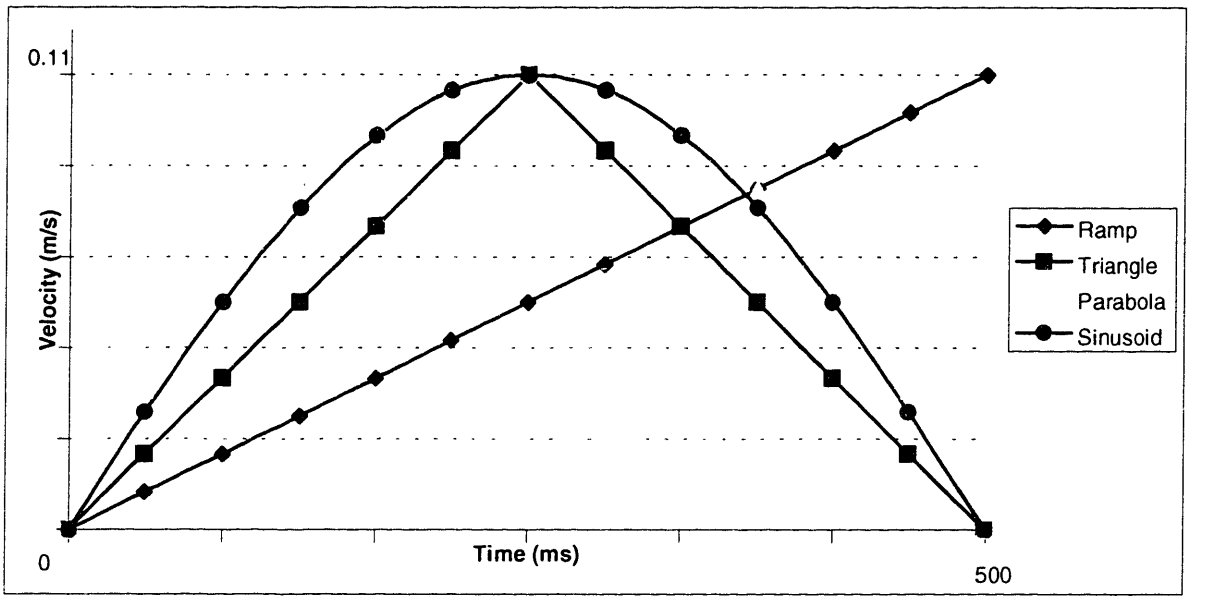

Figure 37: Velocity profiles for which the differential equation of mass motion was solved. Each profile had the same maximum velocity and total time of motion.

The solutions for maximum displacement corresponding to each of the profiles were calculated for a range of potential spring constants (*k*), to be discussed with the hook-shaped haptic model shortly (Equation 3.7). These maximum displacements were then compared to the displacement under a static load equal to mass times acceleration (0.22 m/s^2, calculated from the ramp profile to maintain a consistent basis of comparison); the ratios are plotted in Figure 38. It should be noted immediately that the simple ramp velocity profile yielded a ratio of 2×, as calculated explicitly above.

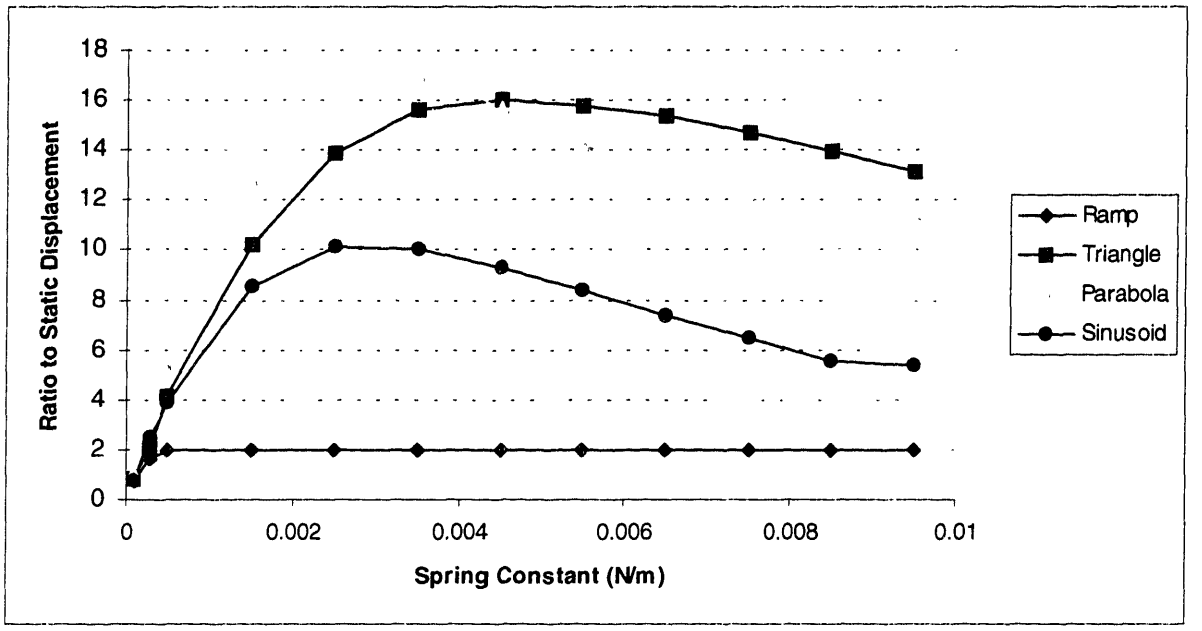

Figure 38: Ratio of maximum displacement (due to corresponding velocity profile in Figure 37) to static displacement (under load *ma*). Note 2× ratio for ramp.

According to E. Kandel, the eye follows a sinusoidal angular velocity profile. It can be seen in Figure 38 that the maximum displacement due to a sinusoidal velocity profile may reach 10 times that of the static displacement. Therefore, as a safety factor, finite element analysis of the haptics use a loading condition of 10 times the mass of the implant times the simplified acceleration (0.22 m/s^2). This force equals (10 × 0.22 m/s^2 × 0.0000274 kg) = 6.028×10^{-5} N, or the force of about 6.1 mg under gravity.

Corresponding to the springs in the mass-spring model, each haptic will carry half of the applied load, or 3.014×10^{-5} N (3.05 mg under gravity). As noted earlier, this loading condition requires the assumption that the rubber annulus acts as a rigid body once implanted; this assumption will be tested later in the section. The haptics were first modeled as three dimensional cylinders with a point load applied at the tip, normal to the long axis of the haptic. Results for four different models are shown in Table 1. These models differed in the number and type of elements used, and the results for each were compared to those predicted by beam theory before a more realistic model of the haptic shape was made. The results improve and begin to converge as more elements and more nodes are used. However, the cost in terms of computing time also increases significantly.

Table 1: Results of three-dimensional modeling of simple beam type haptic

Model Number	*Number and type of elements*	*Maximum Deflection*	*Solution Time*
1	20 (20-node)	-1.444×10^{-3} m	0.41 sec
2	80 (20-node)	-1.607×10^{-3} m	2.26 sec
3	320 (20-node)	-1.666×10^{-3} m	13.75 sec
4	320 (27-node)	-1.672×10^{-3} m	29.92 sec

The 80 node model was chosen to be modified for the realistic haptic model; the maximum deflection for this model was close to the apparent convergence deflection of approximately 1.675×10^{-3} m (extrapolated from Table 1), and the necessary computing time was only 2.26 seconds. Figure 39 shows the behavior of the 80-node beam model, and its deflection is compared with that predicted by beam theory in Figure 40.

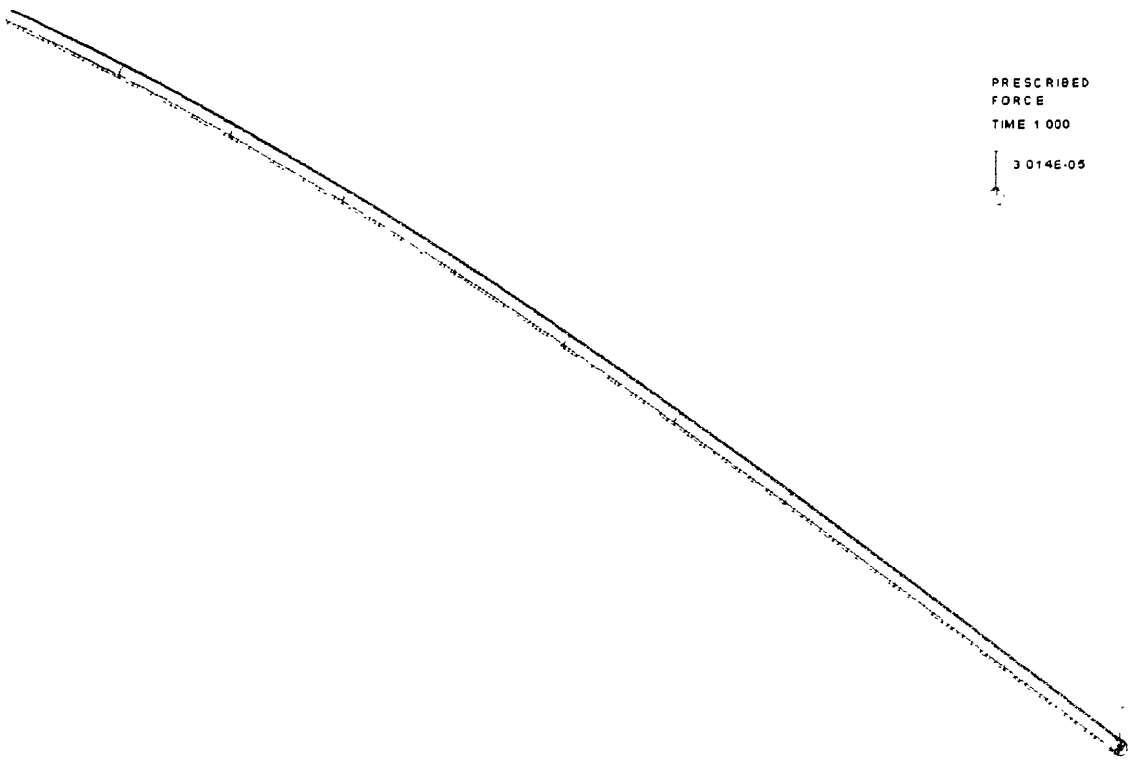

Figure 39: Simple beam under tip load modeled with 80 elements (force in Newtons)

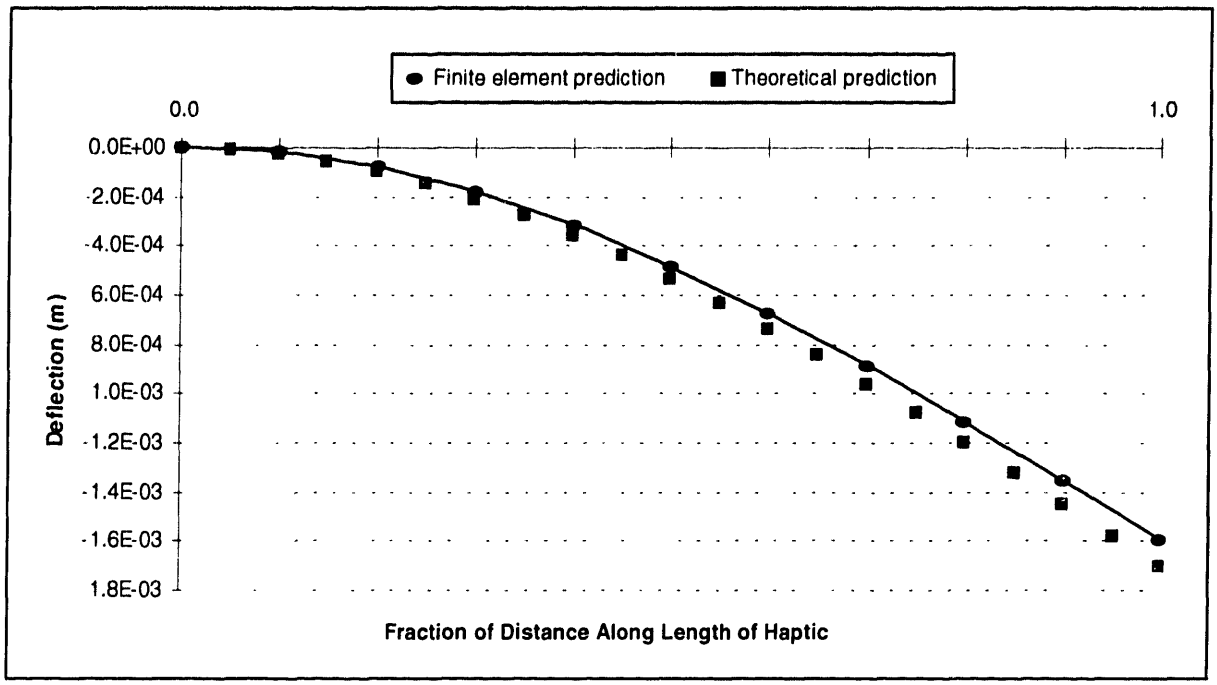

Figure 40: Deflection of simple haptic compared with beam theory prediction

The actual hook-shaped haptic was modeled using the same concepts as the successful simple deflection. The new model is diagramed in Figure 41.

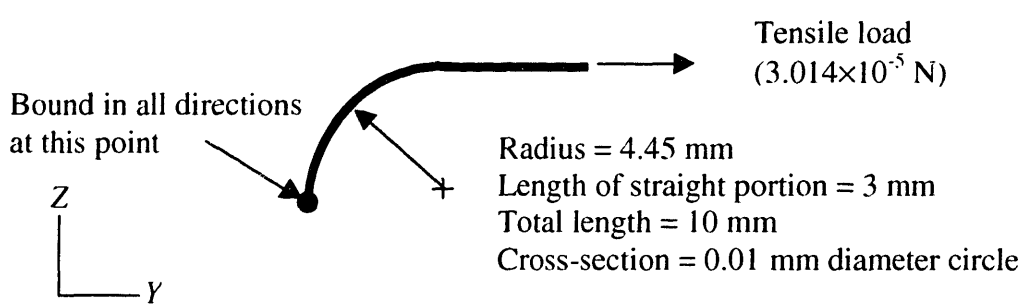

Figure 41: Schematic of hook-shaped haptic input model (represents the left haptic in the top portion of Figure 36; the point in contact with the inside edge of the eye is considered bound in all directions)

Assuming momentarily that the hook-shaped haptic in Figure 41 behaves like a linear spring and the tensile load stretches it completely straight, its equivalent linear spring constant can be calculated; this value was used as the upper range of spring constants plotted in Figure 38:

$$\frac{3.014\times10^{-5}N}{(10-7.45)mm} = 0.000012\frac{N}{mm} = 0.012\frac{N}{m} \qquad (3.7)$$

Several models of the hook-shaped haptic were tried; unfortunately, the 80 element model did not seem sufficient. Significant data from the analyses are shown in Table 2, and Figure 42 shows the behavior of model 2 as an example.

Table 2: Results for three-dimensional modeling of hook-shaped haptic

Model #	*Number of Elements*	*Load*	*Max. Y-Deflection*	*Max Z-Deflection*	*Run Time*
1	80	Tensile	7.803×10^{-5} m	-1.975×10^{-4} m	1.36 sec
2	320	Tensile	1.263×10^{-4} m	-3.116×10^{-4} m	6.58 sec
3	320	Compress	-1.263×10^{-4} m	3.116×10^{-4} m	6.56 sec
4	1280	Tensile	1.326×10^{-4} m	-3.250×10^{-4} m	56.82 sec

Again, the results appear to converge with higher numbers of elements, but at an exponentially increasing cost of computing time. The relevant data were found, however, and seem qualitatively reasonable: under the load imposed by the accelerating support structure mass, the haptics each deflect less than half of one millimeter in both the horizontal (*Y*) and vertical (*Z*) directions. Such a deflection is highly unlikely to dislodge the implant from its position behind the pupil and is therefore within the constraints of the design.

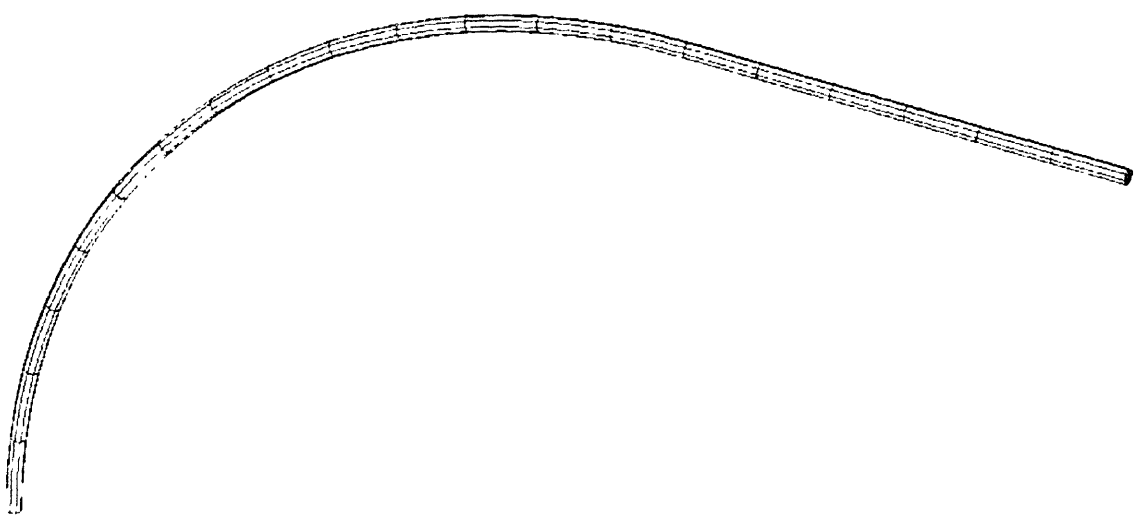

Figure 42: Hook-shaped haptic under tensile load modeled with 320 3-D elements

The assumptions made in analyzing this problem automatically took several safety factors into account. First, damping due to the viscous fluid in the eye was not considered and would in fact decrease the deflection even more. Second, as discussed above, a sinusoidal velocity profile will not necessarily cause a 10× static deflection; that was only the maximum possible as determined by the differential equation of motion. It is interesting to note that the maximum *Y*-deflection observed in the hook-shaped haptic corresponds to a linear spring constant of 0.227 N/m (assuming that the haptic behaves like a linear spring, as was assumed for Equation 3.7). This spring constant is much stiffer than those considered in Figure 38; judging by the trends of those plots, a 10× safety factor was indeed overcautious.

The other major contributor to stability of the implanted electronics is the support tray. Deflection of the tray away from the plane of the rest of the support structure could interrupt communication with the external laser. To determine the rigidity of the tray in design IOS14, it was modeled with three dimensional rubber elements and subjected to gravity loading. In the model, a silicon chip was attached to the tray where the photodiode array would be attached in an actual implant. The chip was assigned material properties equivalent to elemental silicon (ρ = 2.33 g/cm^3 , E = 131 GPa, ν = 0.266) and dimensions equal to those of an actual dummy chip used for prototyping [31].

For simplicity, the tray was modeled with only the section of the annulus it attaches to. The sides of this section were fixed in all directions of motion. The model is shown in Figure 43. A dynamic analysis was performed: gravity loading was applied incrementally in 10 steps over the course of one second to achieve the large strains and displacements expected for the rubber. Several different 20-node element configurations were attempted, from 40 total elements to 2752 total elements. Too few elements yielded unstable results, while too many elements exceeded the memory limitations of the workstations being used. However, a 376 element model produced reasonable results that closely matched experimental results with early prototypes. The maximum amount of tray deflection for this model, shown in Figure 44, was 0.92575 mm. Compared to the 4 mm total length of the support tray, this deflection was rather large. The modeling conditions serve as a safety factor in the analysis; the actual implant would be submerged in a viscous fluid in the eye, not held in a vacuum in a plane perpendicular to gravity. However, the analysis still reveals a mechanical risk in the surgically ideal design IOS14.

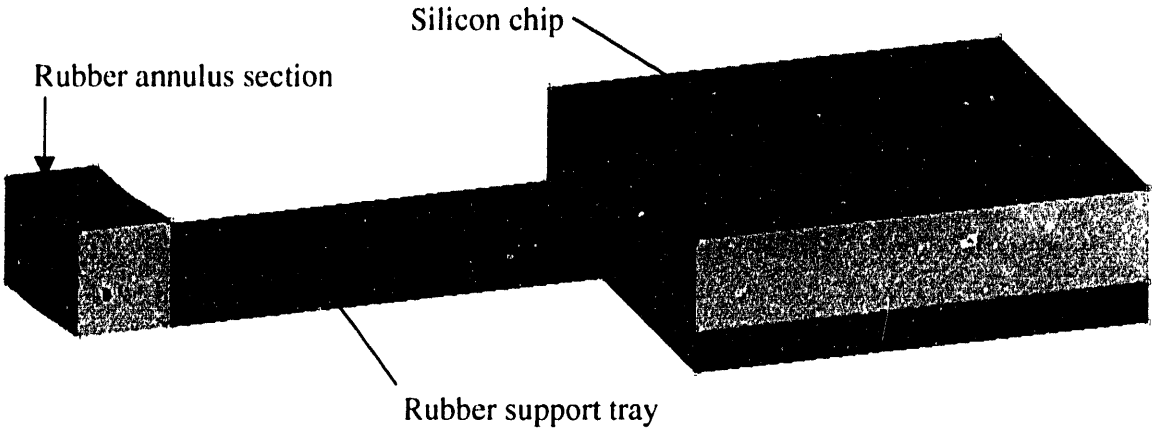

Figure 43: Finite element model of IOS14 support tray with silicon chip under gravity loading (individual elements not pictured)

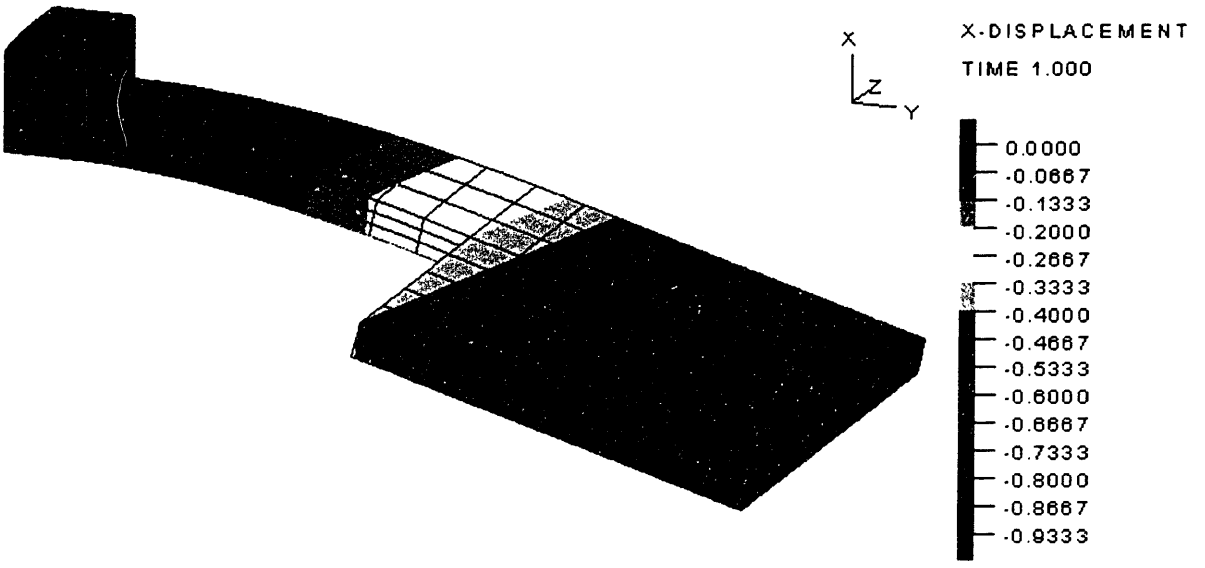

Figure 44: Tray deflection results for 376 element model (scale in millimeters)

Additional support arms for the electronics tray, as incorporated in design IOS05 (Figure 32), were likely to improve the mechanical design Therefore, a sample analysis was performed on IOS05 tray for reference. An element configuration similar to that of the successful IOS14 finite element model was used, resulting in a total of 416 elements. The model is shown in Figure 45, and the deflection results are shown in Figure 46.

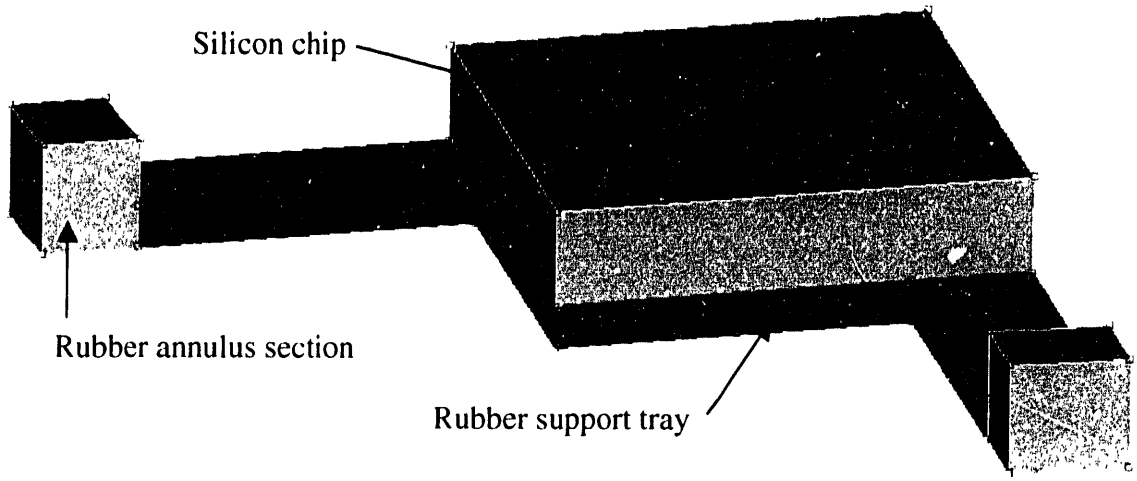

Figure 45: Finite element model of IOS05 support tray with silicon chip

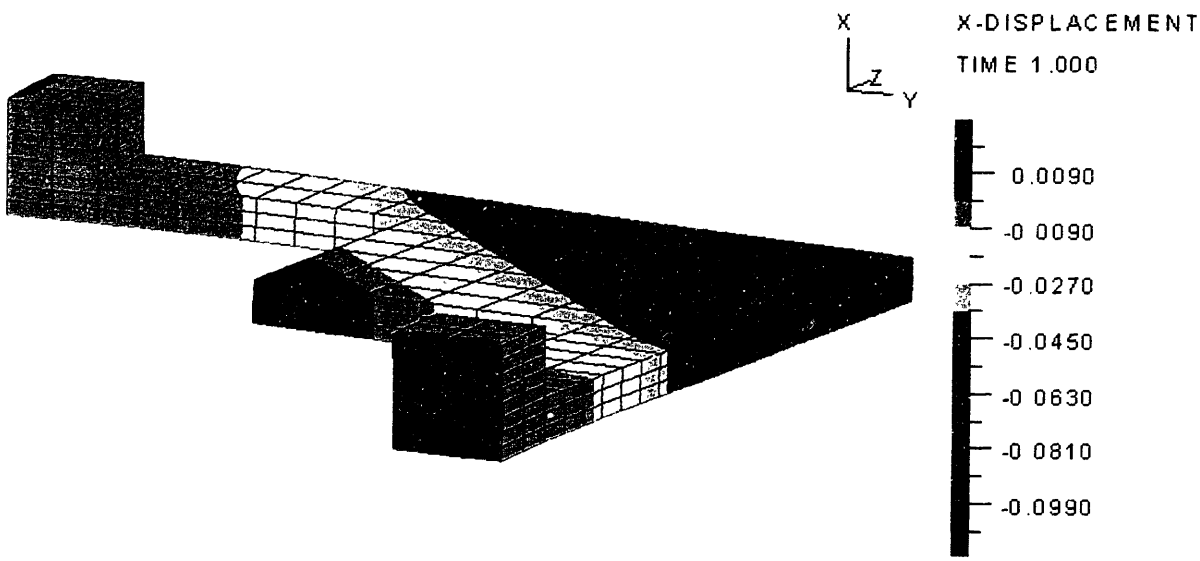

Figure 46: Tray deflection results for 416 element model (scale in millimeters)

The maximum tray deflection in this model was 0.113615 mm, a vast improvement over design IOS14. It was concluded that design IOS14 could be injection molded from the biocompatible silicone rubber for surgical testing, during which tray deflection would be carefully observed. The mold could then be easily modified to produce IOS14 with more tray support arms, a less ideal configuration from a surgical perspective, if necessary.

As discussed earlier, modeling of support structure movement with eye acceleration relied upon the assumption of annulus rigidity relative to the haptics. This assumption was tested by applying a force on an annulus model equivalent to that applied to the haptic models. With the support tray left out for simplicity, a three dimensional model of the annulus was developed. One haptic notch of the ring was held fixed, and a pressure of 60.28 Pa (0.45 mmHg) was applied to the other haptic notch in the positive *Y* direction. This pressure corresponds to a force of 3.014×10^{-5} N (equal to the force applied to the haptic, 5×0.22 m/s^2 $\times$ 0.0000274 kg, discussed above) applied over the area of the notch, 0.5 mm^2. The resulting displacement of the annulus in the *Y* direction is shown in Figure 47, and displacement in the *Z* direction is shown in Figure 48.

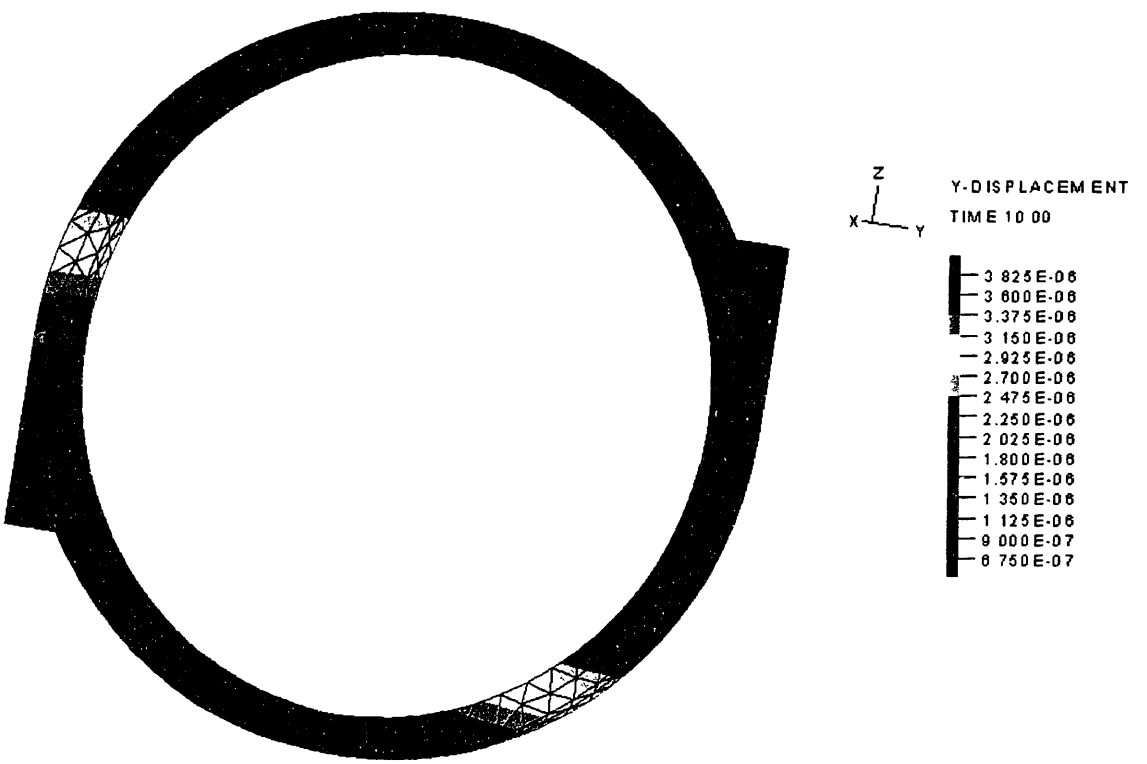

Figure 47: Y-displacement of the annulus under load on the left haptic notch (scale in meters)

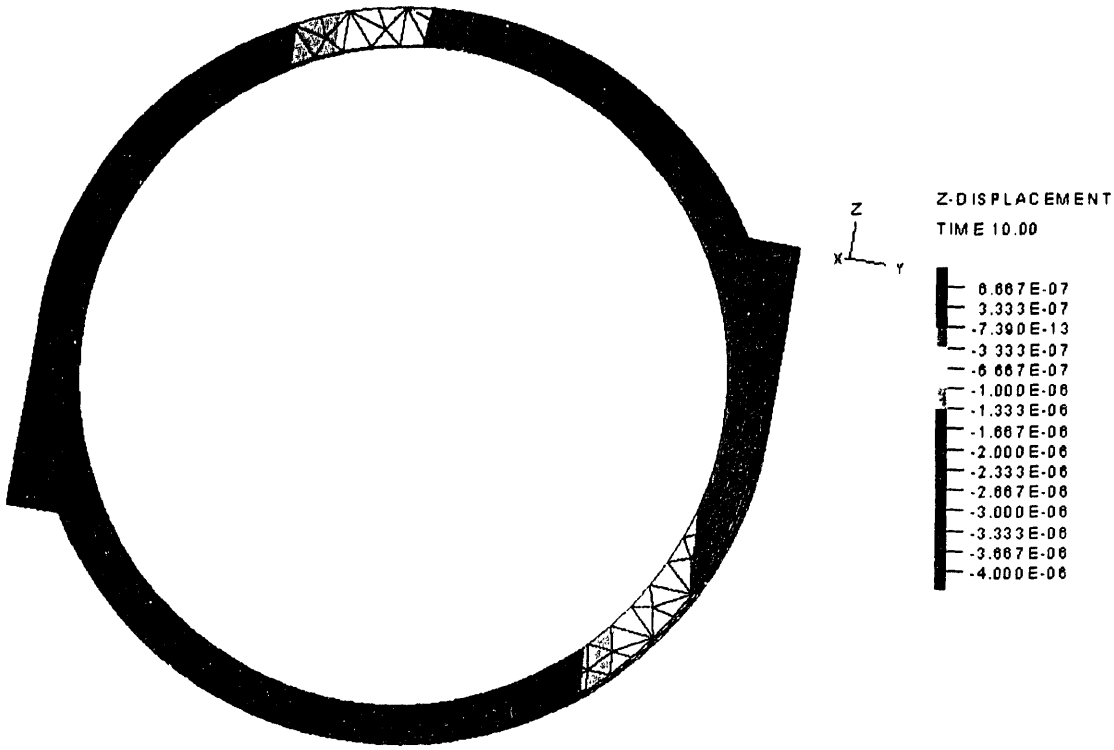

Figure 48: Z-displacement of the annulus under load on the left haptic notch (scale in meters)

These results reveal that the rubber annulus does in fact behave similarly to a rigid body under the calculated loading condition. The assumption used earlier to confine structure stability to haptic deflection is thus valid.

The final analysis accomplished with finite elements involved squeezing the rubber annulus. Normally, an IOL is inserted through the sclera incision and the pupil by grasping it on one edge and gently pushing it through. It seemed likely, however, that a rubber structure would deform under such manipulation. An alternative method for implantation would therefore be to squeeze the annulus by positioning surgical tweezers on the two haptic notches. The annulus has an outer diameter of 7.7 millimeters, approximately equal to the maximum diameter of the pupil [30]. With the annulus significantly compressed, both it and the surgical instrument could be easily accommodated by the incision and pupil. Therefore, stresses within the annulus were analyzed as it underwent large, nonlinear compression.

For this analysis, the annulus was first modeled using two dimensional, 9-node plane stress elements. One notch was fixed in all directions, as if it were on one tip of a tweezers, and a 1.7 millimeter compressive displacement was imposed on the other notch. This compression represents a greater than 20 percent reduction in the horizontal diameter of the annulus, allowing it to slip more easily through the sclera incision and pupil. For all models, 10 time steps of 1.0 seconds each were used in the large strain analysis, with a variety of element sizes. Table 3 shows the significant data for each of three models attempted.

Table 3: Results of two-dimensional modeling of annulus

Model #	*Mesh Size*	*Number of Elements*	*Left haptic notch boundary*	*Run Time*
1	0.4 mm	82	Constrained to move in *Y*-direction	6.1 sec
2	0.2 mm	318		25.1 sec
3	0.1 mm	1170		102.3 sec

All three models showed very similar responses for both *Y* and *Z* tensile stresses, and results for model 1 are shown in Figures 49 and 50. Features of these plots and others not shown were used to improve the structure design. For example, stress concentrations near the haptic notches suggested that some filleting (rounding of sharp corners) was necessary, and the injection mold incorporated such fillets. The maximum tensile stresses were predictably observed at the top and bottom of the annulus. At approximately 80 KPa, these stresses are well within the tensile strength of the MED-4940 silicone rubber used for molding: approximately 8.3 MPa, according to NuSil Technology [25].

Several three-dimensional finite element models of the support structure were also analyzed with similar boundary and loading conditions. Various mesh sizes and time step sequences were tested, revealing slightly higher stresses that were still well within the mechanical limits of the rubber. It was concluded that the two dimensional model was sufficient for compression analysis.

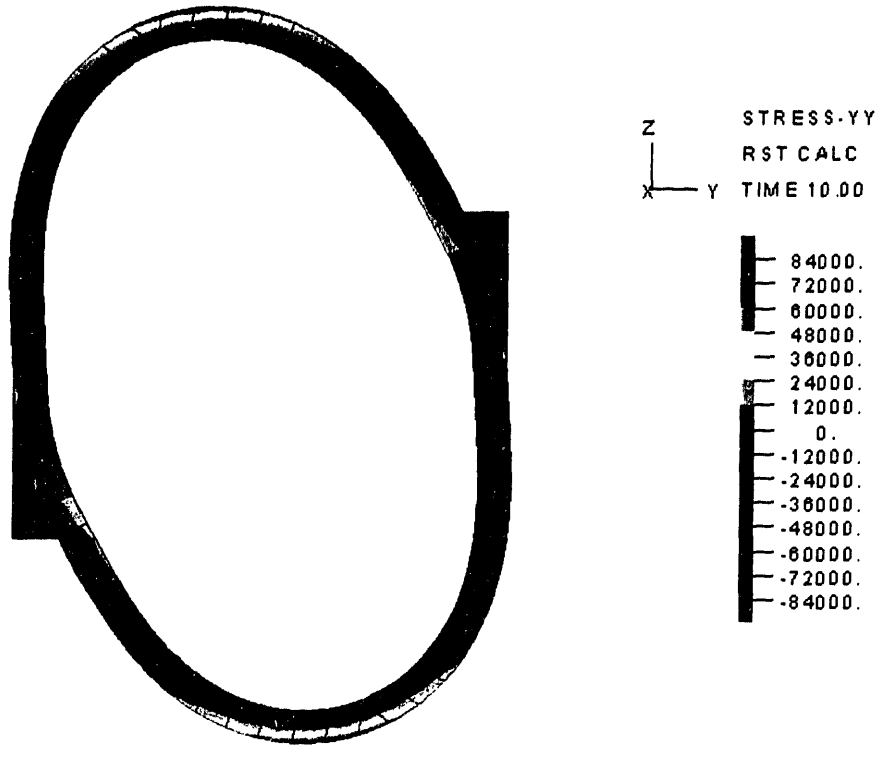

Figure 49: *Y*-direction stresses in 82 element annulus model under compression load (scale in N/m^2)

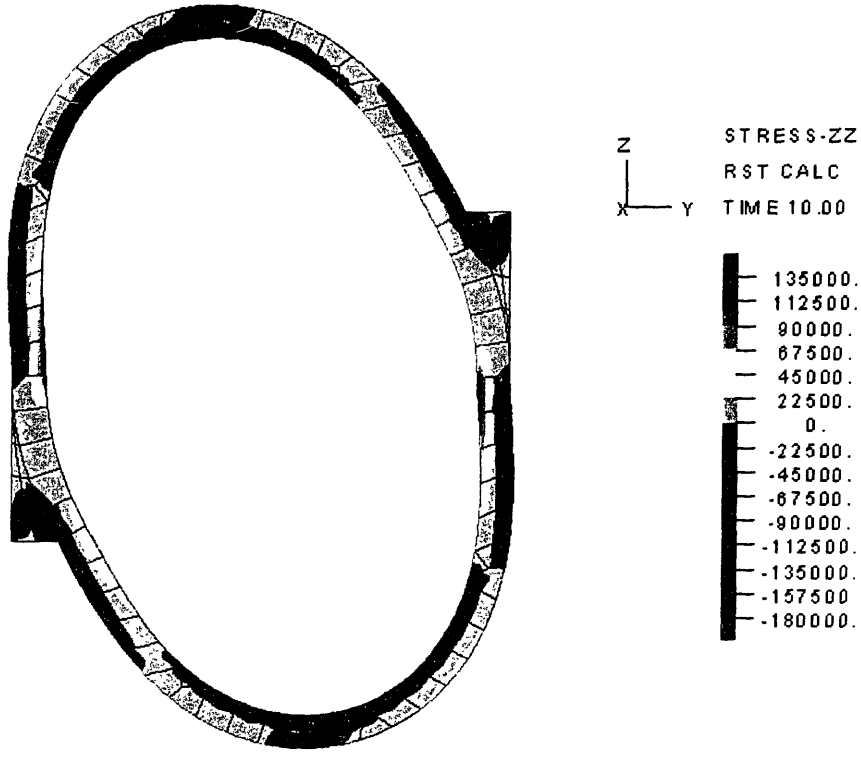

Figure 50: *Z*-direction stresses in 82 element annulus model under compression load (scaleinN/m^2)

3.4 Results and Discussion of Surgical Testing

The annulus and tray portions of design IOS14 were injection molded with silicone rubber (NuSil MED-4940). Small holes, approximately 1 to 2 mm deep, were hand drilled in the haptic notches, and haptics from a commercially available IOL were inserted and secured with silicone. The simple device, without any electronics, was then implanted in an animal as if it were an IOL.

A small incision was made in the sclera near the cornea. Next, the nucleus and cortex of the lens were broken up by ultrasound, a process known as phacoemulsification, and removed by suction. The scleral incision was sutured closed slightly but left large enough to accommodate the entire support structure. In Figure 51, the structure is shown resting on top of the eye just prior to insertion.

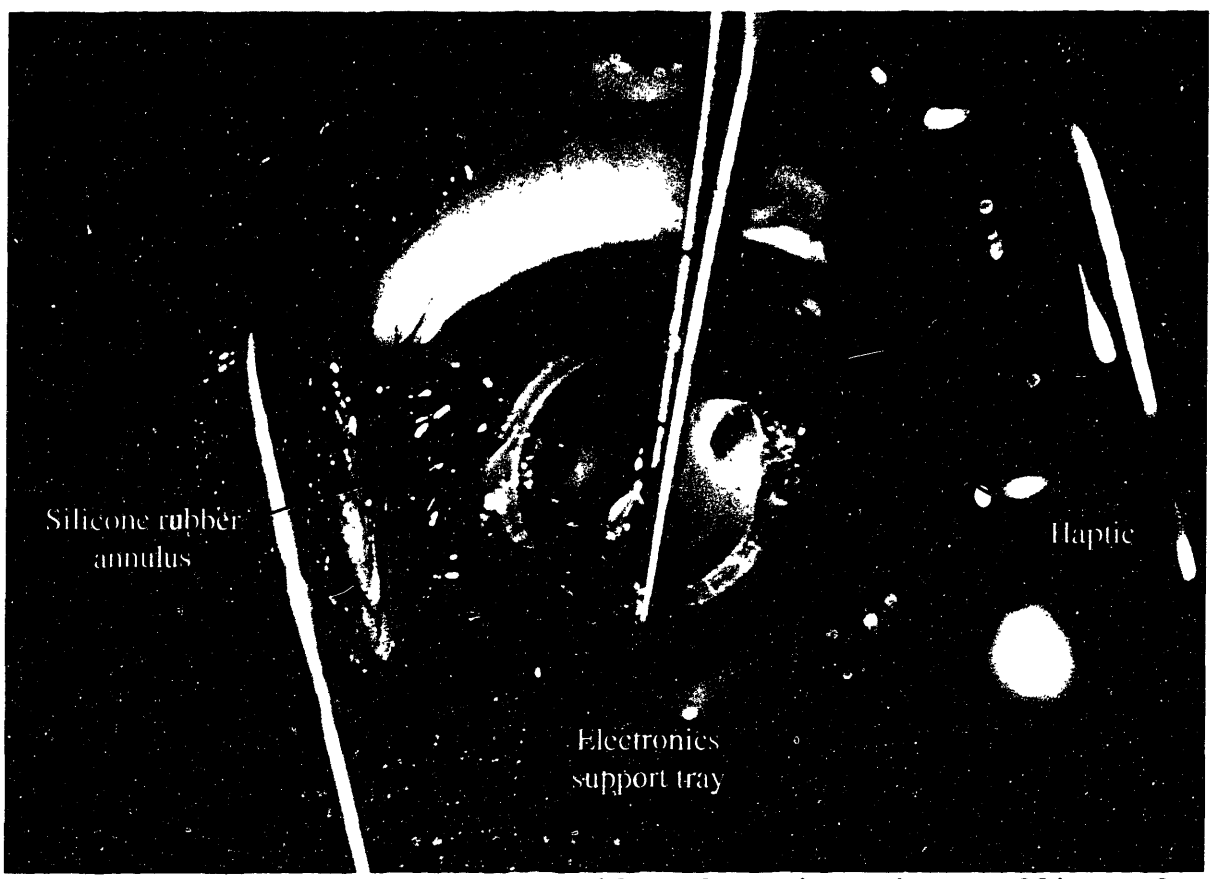

Figure 51: Intraocular support structure with no electronics resting on rabbit eye after phacoemulsification and removal of the lens

After injection of artificial viscoelastic fluid in the anterior chamber, one haptic was held with forceps and inserted. By pushing this leading haptic deeper into the eye, the rest of

the structure was pulled through the incision. The normal technique for inserting an IOL is to first insert the leading haptic and then to push the remainder of the structure through the incision by holding the rigid plastic lens. The surgeon found the pulling technique slightly more difficult than the normal pushing method, but the structure was successfully drawn through the incision without any tissue damage. After the pupil was constricted slightly with medication, the lead haptic was inserted through it. The soft structure could not be rotated easily, but it could be pulled into place behind the iris without damage to itself or the eye. At this point, only the electronics tray of the structure was fully visible in the pupil, and the remaining pupil area was clear for viewing to the posterior portion of the eye. The implanted support structure is shown in Figure 52.

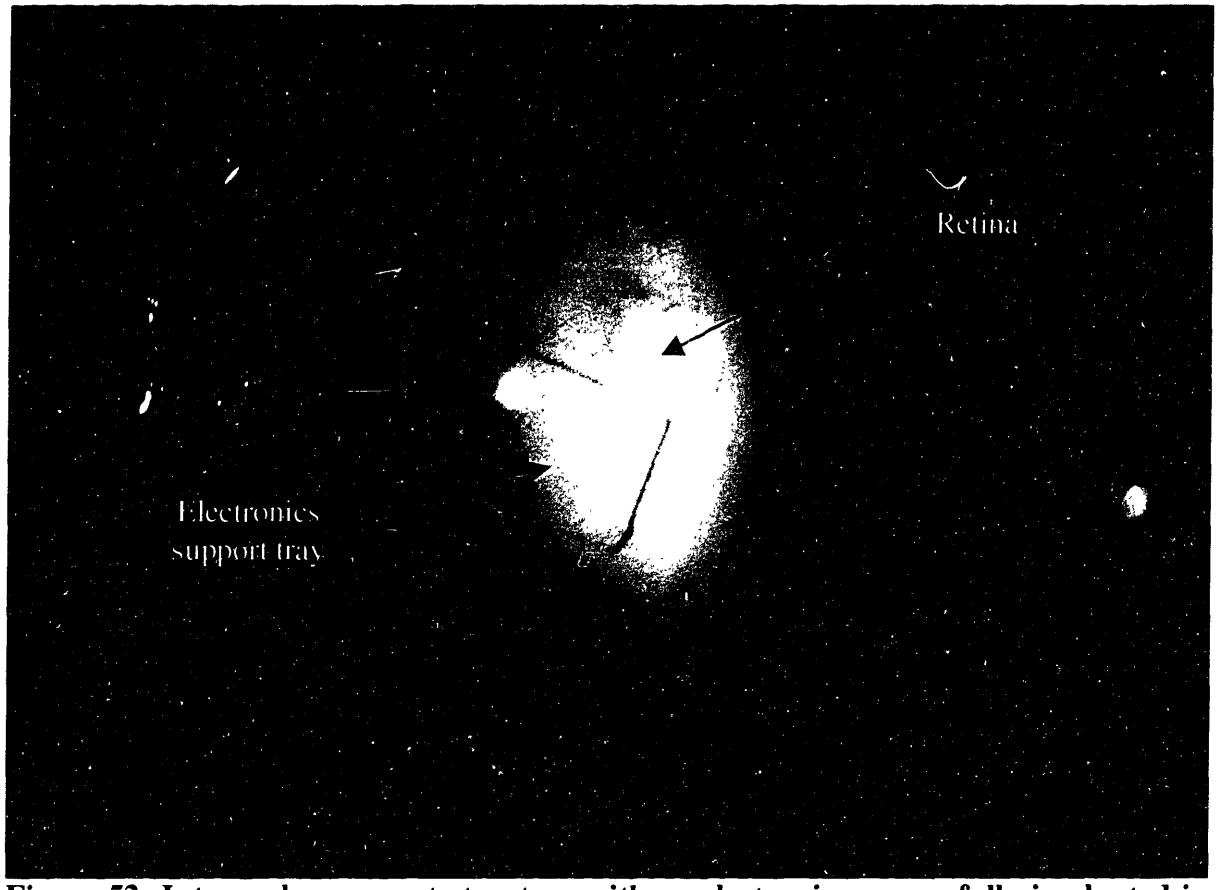

Figure 52: Intraocular support structure with no electronics successfully implanted in rabbit eye

The electronics tray maintained the correct configuration with no visible deflection after implantation, partly due to the viscous nature of the fluid in which it was submerged. However, the surgeon felt that it could be potentially unstable in a fully assembled implant,

and the mechanical relief it might offer when an electrode array is attached would not be beneficial enough to outweigh the disadvantages. The finite element results for a two-arm support tray, as incorporated in design IOS05, were discussed, and a suitable modification to design IOS14 was determined. A very narrow strip could be added across the annulus to create two additional support arms for the electronics tray, as shown in Figure 53.

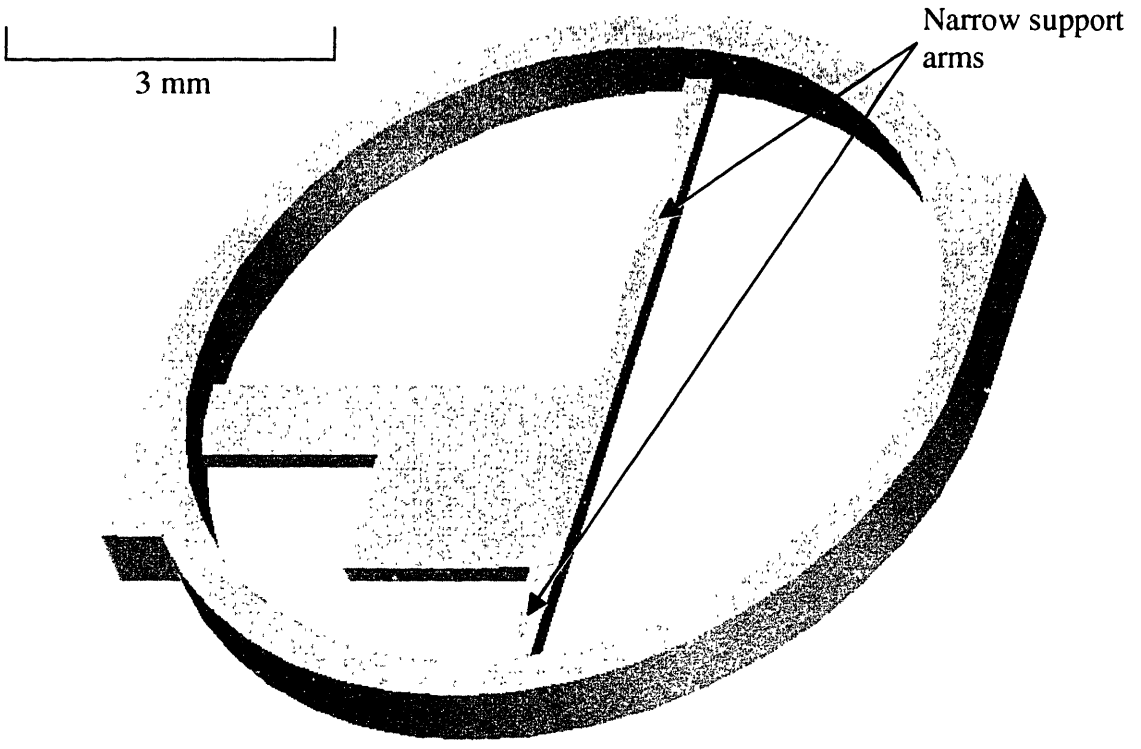

Figure 53: Modified final design (IOS14a) for intraocular support structure

Unlike most of the iterative designs discussed in Section 2.2, the modified IOS14a design will have tray components in more than one quadrant of the circular structure. However, because these additional arms are very narrow, they will not significantly degrade visibility through the structure. In addition, modification of the existing IOS14 injection mold is straightforward, requiring only one additional groove to be cut.

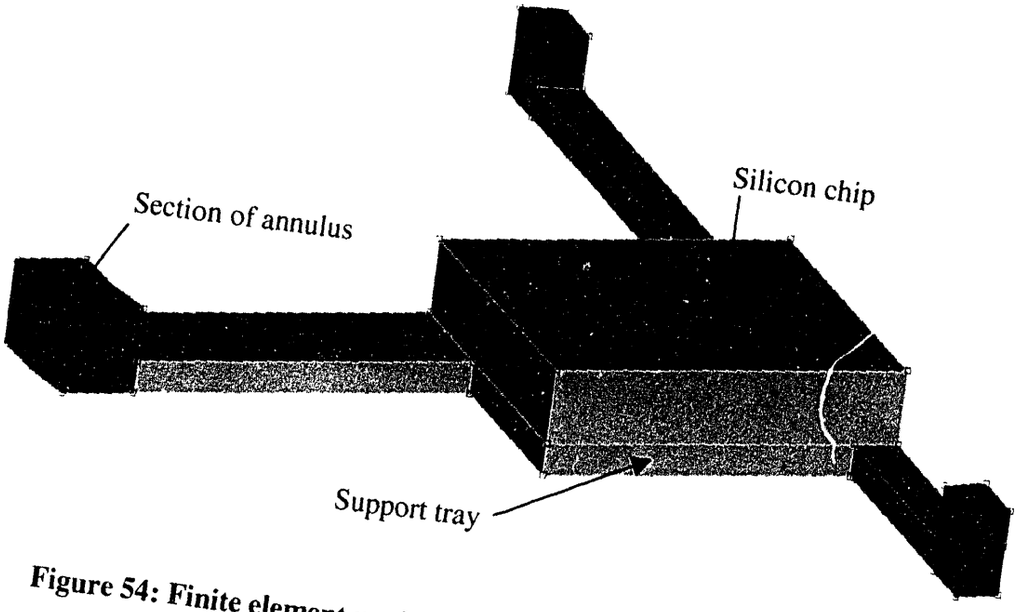

Figure 54: Finite element model of IOS14a support tray with silicon chip

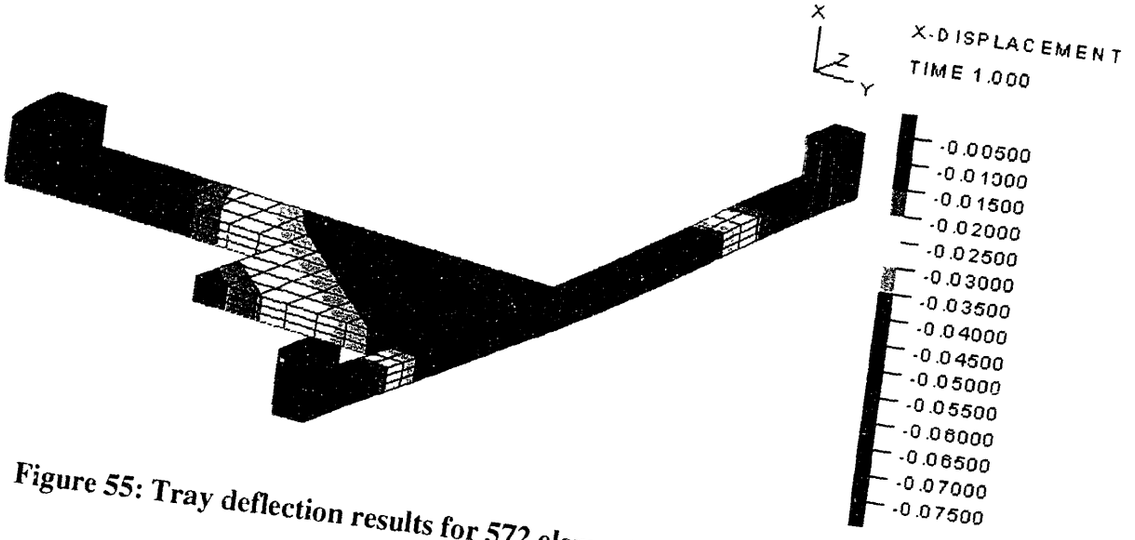

Figure 55: Tray deflection results for 572 element model (scale in millimeters)

The design was tested after the surgery with finite element analysis. Tray deflection under gravity loading of a silicon chip was determined using a similar model and element configuration as previous analyses (Figures 43-46). The model is shown in Figure 54, and

the deflection results are shown in Figure 55. The results are very promising: the maximum tray deflection was only 0.0775526 mm, even smaller than the deflection observed in design IOS05. The silicone will still offer mechanical relief to the tray supports, but the tray will be significantly more rigid without sacrificing too much crucial open space.

3.5 Conclusions and Future Directions

Using criteria developed for both surgical and mechanical advantages, a unique intraocular support structure was iteratively designed. Each iteration was quickly prototyped by stereolithography to give surgeons a more accessible means of participating in the design process, a technique that proved highly successful. The final design met all requirements except biocompatibility when fabricated from hard SLA epoxy.

The final iteration was analyzed using finite element methods as if fabricated from biocompatible silicone rubber. Stability of the structure during movement of the eye was confirmed with static analysis of the haptics, and the assumption of relative rigidity of the annulus was confirmed with large strain analysis. However, results for tray deflection caused some concern about the ability to maintain photodiode array orientation in the proper plane. These results prompted additional analysis for a potential alternative tray design, which proved to be much more stable. An injection mold for the original design in question was created, and the structure was fabricated with silicone rubber for surgical testing.

Surgical results were positive, but concern was expressed about the stability of the electronics tray. In addition, the elastic nature of the silicone structure made implantation slightly more difficult compared to the procedure for a normal, rigid IOL. The promising finite element results for alternative tray designs were discussed, and an appropriate modification was determined. The modified design was similarly analyzed with finite element methods, and it proved to be very stable.

With the support structure design complete, only small tasks remain in improving its production. The current mold requires minor modifications to incorporate the added tray support arms. The mold might also be improved by adding a port for vacuum attachment. Although the silicone is degassed by centrifugation before injection, microscopic air bubbles can form as it squeezes around the small corners. These air bubbles then expand when

heated during the curing process. By drawing air out of the mold with a vacuum as the silicone is injected, bubble formation may be prevented.

In addition, a technique for fabricating haptics from plain suture material will be devised. Currently, haptics are removed from expired intraocular lenses and then inserted into the injection molded annulus. However, limitations on the supply of expired IOLs precludes the use of this method indefinitely. Polypropylene, a thermoplastic, can be melted and re-solidified in different shapes by heating. Therefore, the haptics may be incorporated directly in the intraocular support structure mold or molded separately and installed.

Finally, new materials may be used in future incarnations of the support structure. The NuSil MED-4940 was selected for its molding applicability and the accuracy with which it could be modeled with finite element methods. In addition, its material properties approach the maximum hardness that can be injection molded by hand. Harder, non-elastomeric materials would likely require a more complicated molding procedure, but they may offer increased rigidity to behave more like a normal IOL during surgical implantation.

Chapter 4
Summary and Conclusions

The preceding chapters describe accomplishments that will help the Retinal Implant Project progress towards an important milestone: chronic animal testing of a completely implantable prosthesis.

4.1 Hermetic Encapsulation Testing

Several important achievements were detailed in Chapter 2. First, a reliable model of a prototype implant, duplicating the salient dimensions and materials, was developed. The materials primarily tested were silicone, polyimide, and platinum, but the model is flexible enough to allow measurement of fluid leakage at almost any choice of material interfaces. In addition, the models can be fabricated quickly, inexpensively, and reproducibly, preserving valuable microelectronics for implantation.

A robust, sensitive current measurement apparatus was designed and built for testing the implant models. The setup can detect leakage currents as low as 10^{-15} amps and presently supports up to nine models simultaneously in a 37°C saline bath. The setup is highly automated and capable of acquiring data over a wide variety of user-defined intervals. It currently requires only weekly maintenance, and it can be easily expanded to support more models. In addition, the entire apparatus is now shielded from ambient electromagnetic fields by a large Faraday cage, further stabilizing the low current measurements.

After many trials with the models and test apparatus, it was determined that both silicone-polyimide and silicone-platinum interfaces are highly susceptible to fluid leakage, putting the microelectronics of a prototype implant at risk. However, the protocols and devices developed over the course of this thesis provide a relatively fast and inexpensive tool for testing a wide variety of encapsulation techniques. Indeed, early quantitative and qualitative results obtained with a silicone-silicon interface and epoxies indicate a high potential for eventual success with polymer encapsulation. If such success can be attained, the results will benefit both the Retinal Implant Project and medical device design in general.

4.2 Intraocular Support Structure

Using stereolithography as a tool for rapid prototyping, a custom support structure for holding the implanted microelectronics in the front of the eye was designed and fabricated. The goal was to move all implanted electronics except the electrode array, which is fabricated on a very thin strip of polyimide, off of the retina. The resulting reduction in mechanical burden on the retina will likely improve the overall biocompatiblity of the device.

As described in Chapter 3, the structure was designed in an iterative fashion, using feedback from eye surgeons as well as analysis of mechanical properties. The final design incorporates the same type of haptics as commercially available intraocular lenses. In addition, it holds the photodiode array in place behind the pupil while not obstructing the surgeons view of the retina in the back of the eye. Successful animal surgeries were performed with the hard epoxy version produced by stereolithography.

To determine the feasibility of a silicone rubber version of the final design, several finite element analyses were performed. Stability of the entire structure during eye movement was confirmed, and its potential for non-destructive deformation during implant surgery was investigated. In addition, deflection of the electronics support tray under the weight of the implanted electronics was analyzed, revealing potentially problematic results. A test structure was molded from a hard silicone rubber and implanted in an animal eye with no electronics. The surgeon found implantation of the rubber structure to be slightly more difficult than the procedure for a more rigid structure. However, once implanted, the structure appeared to be stable and correctly positioned. The floppy nature of the electronics support tray was noted as a potential problem, confirming the finite element analysis. Therefore, minor design modifications for correction of the problem were discussed and later analyzed, yielding promising results. The current mold for the silicone structure will be modified to stabilize the soft structure, and fabrication from harder materials will also be attempted. Additional animal surgeries will be performed within the next several months to test the new structures. It may also be possible to combine the support structure fabrication with the microelectronics encapsulation. A one-piece structure, made from a single material, would thus support and protect the implanted electronics.

References

[1] J. F. Rizzo and J. Wyatt, "Prospects for a visual prosthesis," *The Neuroscientist*, vol. 3, pp. 251-262, 1997.

[2] E. L. Berson, "Retinitis pigmentosa. The Friedenwald lecture," *Investigative Ophthalmology & Visual Science*, vol. 34, pp. 1659-1676, 1993.

[3] C. A. Curcio, N. E. Medeiros, and C. L. Millican, "Photoreceptor loss in age-related macular degeneration," *Investigative Ophthalmology & Visual Science*, vol. 37, pp. 1236-1249, 1996.

[4] J. L. Wyatt and J. F. Rizzo, "Ocular implants for the blind," *IEEE Spectrum*, vol. 33, pp. 47-53, 1996.

[5] J. L. Wyatt, J. Mann, D. J. Edell, J. Raffel, and J. F. Rizzo, "Development of a silicon retinal implant: demonstration of microelectronic system for optic transmission of signal and power," *Investigative Ophthalmology & Visual Science*, vol. 35, pp. 1380, 1994.

[6] B. K. Wagner, "Electrodes, leads, and biocompatibility," in *Design of Cardiac Pacemakers*, J. G. Webster, Ed. New York: Institute of Electrical and Electronics Engineers, 1995.

[7] P. P. Tarjan and R. D. Gold, "Implantable medical electrical devices," in *Handbook of Biomedical Engineering*, J. Kline, Ed. New York: Academic Press, 1988.

[8] D. J. Edell, J. W. Heller, and D. Petraitis, "Cochlear implant technology," presented at 18th Annual International Conference of the IEEE Engineering in Medicine and Biology Society, Amsterdam, 1996.

[9] B. Smith, P. H. Peckham, M. W. Keith, and D. D. Roscoe, "An externally powered, multichannel, implantable stimulator for versatile control of paralyzed muscle," *IEEE Transactions on Biomedical Engineering*, vol. BME-34, pp. 499-508, 1987.

[10] W. W. Dawson and N. D. Radtke, "Evaluation of microelectronics chronically implanted on the retina," *Documenta Ophthalmologica*, vol. 12, pp. 357-362, 1977.

[11] D. J. Edell, "Insulating Biomaterials," NIH-NINDS Neural Prosthesis Program Contract NO1-NS-3-2301, 1993-1996.

[12] D. J. Edell, "Insulating Biomaterials," NIH-NINDS Neural Prosthesis Program Contract NO1-NS-6-2350, 1996-1999.

[13] P. E. K. Donaldson, "Aspects of silicone rubber as an encapsulant for neurological prostheses. Part 1: Osmosis," *Medical & Biological Engineering & Computing*, vol. 29, pp. 34-39, 1991.

[14] "Request for Proposals: Insulating Biomaterials," in *http://www.ninds.nih.gov/npp/default.htm#RFP*: National Institutes of Health-National Institute of Neurological Disorders and Stroke, 1999.

[15] D. F. Lovely, M. B. Olive, and R. N. Scott, "Epoxy moulding system for the encapsulation of microelectronic devices suitable for implantation," *Medical & Biological Engineering & Computing*, vol. 24, pp. 206-208, 1986.

[16] M. F. Nichols and A. W. Hahn, "Electrical insulation of implantable devices by composite polymer coatings," *ISA Transactions*, vol. 26, pp. 15-18, 1987.

[17] M. Sawan, F. Duval, J.-S. Li, M. Hassouna, and M. M. Elhilali, "A new bladder stimulator--hand-held controller and miniaturized implant: preliminary results in dogs," *Biomedical Instrumentation & Technology*, vol. 27, pp. 143-149, 1993.

[18] L. Bowman and J. D. Meindl, "The packaging of implantable integrated sensors," *IEEE Transactions on Biomedical Engineering*, vol. BME-33, pp. 248-255, 1986.

[19] J. Loewenstein, J. F. Rizzo, M. Shahin, and A. Coury, "Novel retinal adhesive used to attach electrode array to retina," *Investigative Ophthalmology & Visual Science*, vol. 40, pp. 3874, 1999.

[20] P. E. K. Donaldson and B. J. Aylett, "Aspects of silicone rubber as an encapsulant for neurological prostheses. Part 2: Adhesion to binary oxides," *Medical & Biological Engineering & Computing*, vol. 33, pp. 285-292, 1995.

[21] K. Najafi, "Hermetic Packages and Feedthroughs for Neural Prostheses," NIH-NINDS Neural Prosthesis Program Contract N01-NS-4-2319, 1994-1998.

[22] P. E. K. Donaldson, "Aspects of silicone rubber as an encapsulant for neurological prostheses. Part 3: Adhesion to mixed oxides," *Medical & Biological Engineering & Computing*, vol. 33, pp. 725-727, 1995.

[23] P. E. K. Donaldson, "Aspects of silicone rubber as an encapsulant for neurological prostheses. Part 4: Two-part rubbers," *Medical & Biological Engineering & Computing*, vol. 35, pp. 283-286, 1997.

[24] E. M. Arruda and M. C. Boyce, "A three-dimensional constitutive model for the large stretch behavior of rubber elastic materials," *Journal of the Mechanics and Physics of Solids*, vol. 41, pp. 389-412, 1993.

[25] "Product Profile: MED-4940 Liquid Silicone Rubber," NuSil Technology, Carpintera, CA, 1999.

[26] "Product Data Sheet: COHRlastic Silicone Solid Rubber," Greene Rubber Company, Inc., Woburn, MA, 1998.

[27] Z. Guoxing and W. Shoumei, "New constitutive relationship of incompressible hyperelasticity," *Chinese Journal of Aeronautics*, vol. 11, 1998.

[28] D. Roylance, "Table of Mechanical Properties," in *http://www.mit.edu/courses/3.041/props.txt*: MIT Course 3.041, 1998.

[29] E. R. Kandel, J. H. Schwartz, and T. M. Jessell, *Principles of Neural Science*, Third ed. Norwalk, Connecticut: Appleton & Lange, 1991.

[30] G. Wyszecki and W. S. Stiles, *Color Science: Concepts and Methods, Quantitative Data and Formulae*. New York: John Wiley and Sons, 1982.

[31] R. C. Weast, "Handbook of Chemistry and Physics," 55th ed. Cleveland: CRC Press, 1975.

[32] "LabVIEW drivers kei617b.llb, kei7001.llb," in *ftp://ftp.keithley.com/pub/instr/drivers/labview*: Keithley Instruments, Inc., 1998.

[33] M. C. Boyce, "Overview of Rubber Elasticity," Lecture notes, Course 2.305: Massachusetts Institute of Technology, Cambridge, MA, October 1997.

[34] R. S. Rivlin, "A note on the torsion of an incompressible highly-elastic cylinder," *Proceedings of the Cambridge Philosophical Society: mathematical and physical sciences*, vol. 45, pp. 485-487, 1949.

[35] "ADINA Theory and Modeling Guide, Volume I: ADINA," Report ARD 97-7: ADINA R&D, Inc., Watertown, MA, November 1997.

Appendix A
Test Model Fabrication Procedures

A.1 Silicone-Polyimide Interface Leakage Detection Component

Materials:

Polyimide: 1.5 in.×0.125 in.×10 μm

Aluminum foil: 0.75 in.×0.25 in.

Platinum wire, bare: 2.5 in.×0.003 in. diameter

Preparation of Materials:

Polyimide:

1) Using a sharp scalpel blade, create a 1/16 in. long slit across the polyimide strip approximately 3/8 in. from one end.

Aluminum foil:

1) Cut notches such that half the length is slightly less than 1/16 in. wide.

2) Cut the narrow end to a point.

Platinum wire:

1) Bend approximately 1/4 in. of the wire back on itself.

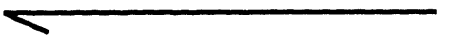

Fabrication:

1) Insert the narrow end of the aluminum foil through the slit in the polyimide.

2) Insert the bent end of the wire through the slit in the polyimide, keeping it underneath the wide portion of aluminum foil.

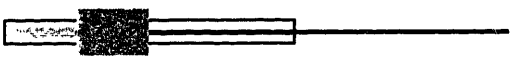

3) Turn the assembly over and pull the wire so it hooks around the slit in the polyimide.

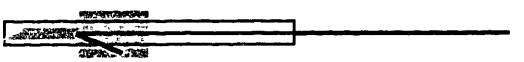

4) Position the short portion of the platinum wire as close to the midline of the polyimide strip as possible and bend the narrow end of the aluminum foil over it.

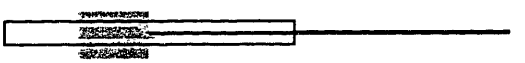

5) Fold the overhanging portions of the aluminum foil over the sides of the polyimide strip.

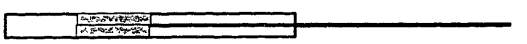

6) Turn the assembly over and squeeze the aluminum foil around the platinum wire with sharp forceps. Use an multimeter to confirm electrical connection between the wire and foil.

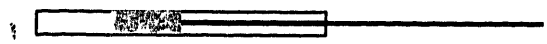

Simplified Representation:

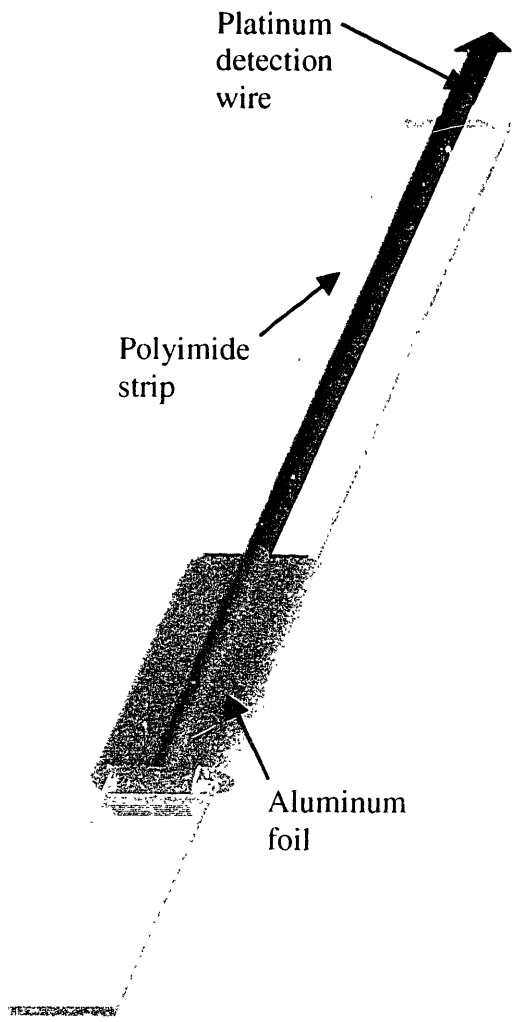

A.2 Silicone-Platinum Interface Leakage Detection Component

Materials:

Platinum wire, bare: 2.25 in.×0.003 in. diameter

1.5 in.×0.003 in. diameter

Silicone tube: 3/16 in.×0.020 in. inner diameter×0.037 in. outer diameter

White filter paper: 3.0 in.×0.75 in.×~0.005 in.

Silicone rubber: NuSil MED4-4220

Preparation of Materials:

Platinum wire:

1) Bend approximately 1/16 in. of each wire back on itself.

Filter paper:

1) Using a sharp scissors, shave a long strip of paper from the edge. The starting end should come nearly to a point, and the other end should be no wider than 1/8 in.

2) Cut the thin end to ensure there is no fraying.

Fabrication:

1) Insert the filter paper into the silicone tube and carefully pull it through until the width of the paper slightly deforms the cross-section of the tube.

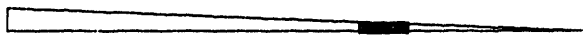

2) Cut the ends of the silicone tube such that the tube is approximately 3/16 in. long with filter paper inside the entire length.

3) Insert the platinum wires into the silicone tube such that one wire is on either side of the filter paper and the bent portions of the wires are on opposite ends.

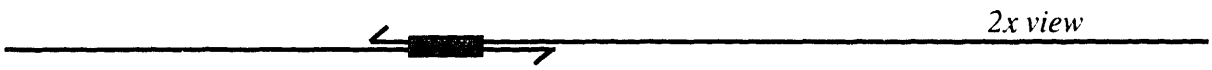

4) Pull the wires through until they hook over the edge of silicone tube and flatten the bent portions down against the tube. Use a multimeter to confirm that the two wires are *not* in electrical contact.

5) Using a drawn-out glass rod or a similar applicator with a fine, pointed tip, apply a small drop of silicone rubber to both end of the silicone tube. Cure the rubber at 100°C for 10-15 minutes. The silicone will likely be drawn into the tube by a capillary effect; the tube is only usable if both ends are sealed but at least half of its length is not filled with silicone rubber.

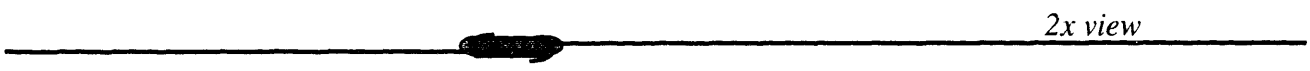

Simplified Representation (approximately 30x actual size):

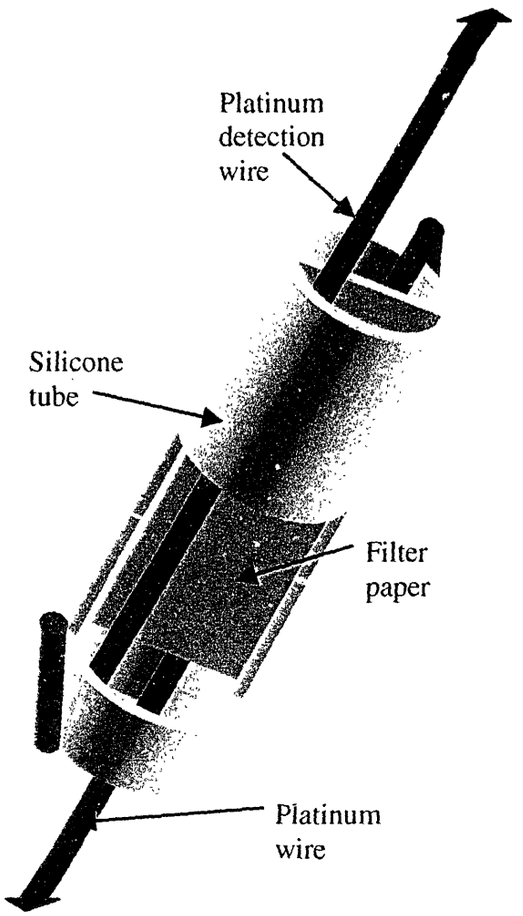

Note: Silicone end-plugs not depicted, and cutaway of tube included for clarity

A.3 Test Model 8

Materials:

Polyimide assembly (see A.1)

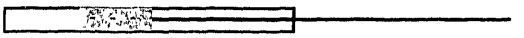

Platinum wire capsule assembly (see A.2)

Silicone rubber: NuSil MED4-4220

Teflon film: 4 pieces, approximately 3/8 in.×3/16 in.×~0.001 in. each

Clear tape: 3 pieces, approximately 1.25 in.×3/16 in. each

Black electrical tape: 2 pieces, approximately 1.25 in.×3/16 in. each

Aluminum mold (inside surfaces shown)

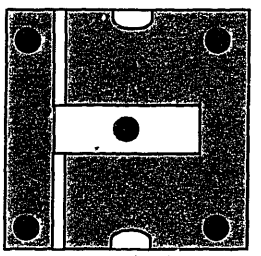

Top half

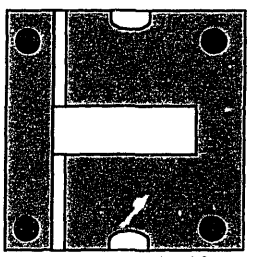

Bottom half

Mold release: McLube 1700 recommended

Flathead screwdriver: 2, 3/16 in. head

Fabrication:

1) Apply a light, even coat of mold release to the inside surfaces of both aluminum mold halves.

2) Using clear tape, tape the polyimide assembly across the inside surface of the *top* half of the mold. The tape should be applied perpendicular to the direction of the polyimide strip and should only cover about 1/16 in. of each end (left figure). Also, the platinum wire should remain over the tape, not stuck under it. The tape should then be stuck to the *side* of the mold, not on the inside surface. Position the polyimide such that the edge is about 1 mm from the side of the mold cavity and the end of the aluminum foil is about 1 mm from the end of the mold cavity (right figure).

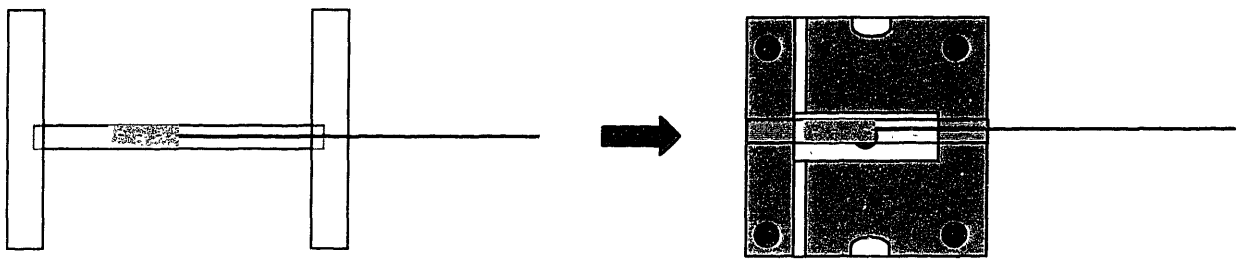

3) Using clear tape, tape the remaining platinum wire down to the side of the mold, keeping it fairly taut.

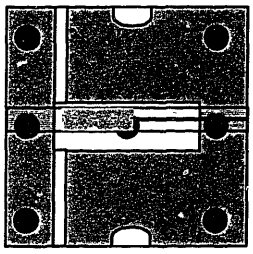

4) Using electrical tape, tape the platinum wire assembly across the inside surface of the *top* half of the mold. The wire should be positioned about 1 mm from the side edge of the mold cavity and the silicone tube capsule should be about 1 mm from the end of the mold cavity. Pull gently on both wires in the silicone tube to make them fairly taut. The silicone tube capsule and aluminum foil should *not* touch.

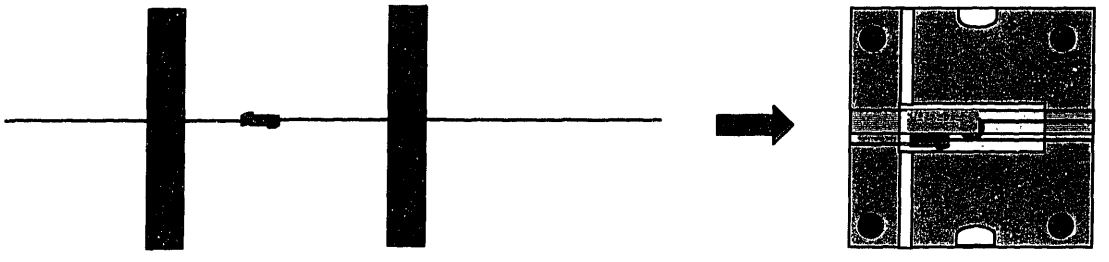

5) Place pieces of Teflon film above and below the portions of polyimide in contact with the inside surface of the mold. The pieces below the polyimide should also go below the platinum wires of the platinum wire capsule assembly. The pieces above the polyimide should go below all platinum wires as well.

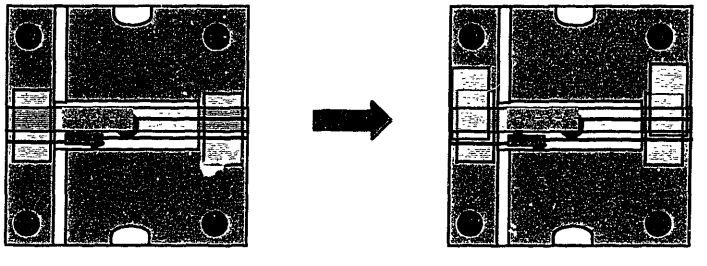

6) Put the bottom half of the mold onto the top half and secure the mold assembly with four screws.

7) Inject silicone rubber until it overflows from the side canals and the injection port of the mold. Cure for 10 to 15 minutes at 100°C.

8) Remove excess cured silicone rubber from the mold. Carefully remove all tape on the sides of the mold and all screws.

9) Using flathead screwdrivers, *slowly* pry the mold open using the slots on either side. Ensure that the polyimide is not sticking to the aluminum anywhere.

10) Starting with the end farthest from the aluminum foil and silicone tube capsule, carefully pry the model out of the mold. A flat-nosed forceps works well in this situation. Clean off excess silicone, cut off excess polyimide, and double-check the entire assembly under a microscope.

Simplified Representation:

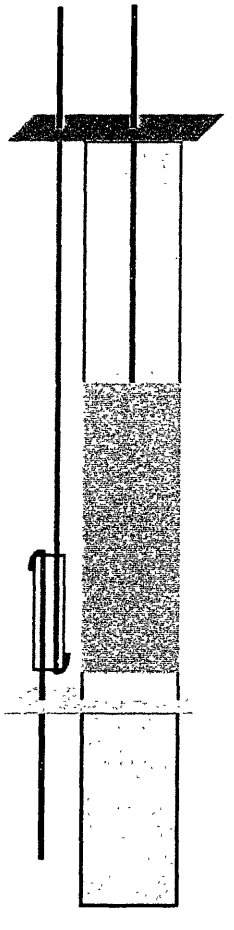

Appendix B

LabVIEW Data Acquisition Virtual Instrument (VI)

The following pages show the diagram assembled in LabVIEW to create a data acquisition virtual instrument (VI) . The diagram is divided into six portions, or pages, numbered 0 through 5; together, these pages illustrate the procedure for analyzing an individual test model. All six portions are contained in a loop, which allows continuous measurement of multiple models as long as the user desires. A brief description of the function of each portion is also included. The electrometer and switch system subVIs were obtained from Keithley Instruments, Inc. via the World Wide Web [32].

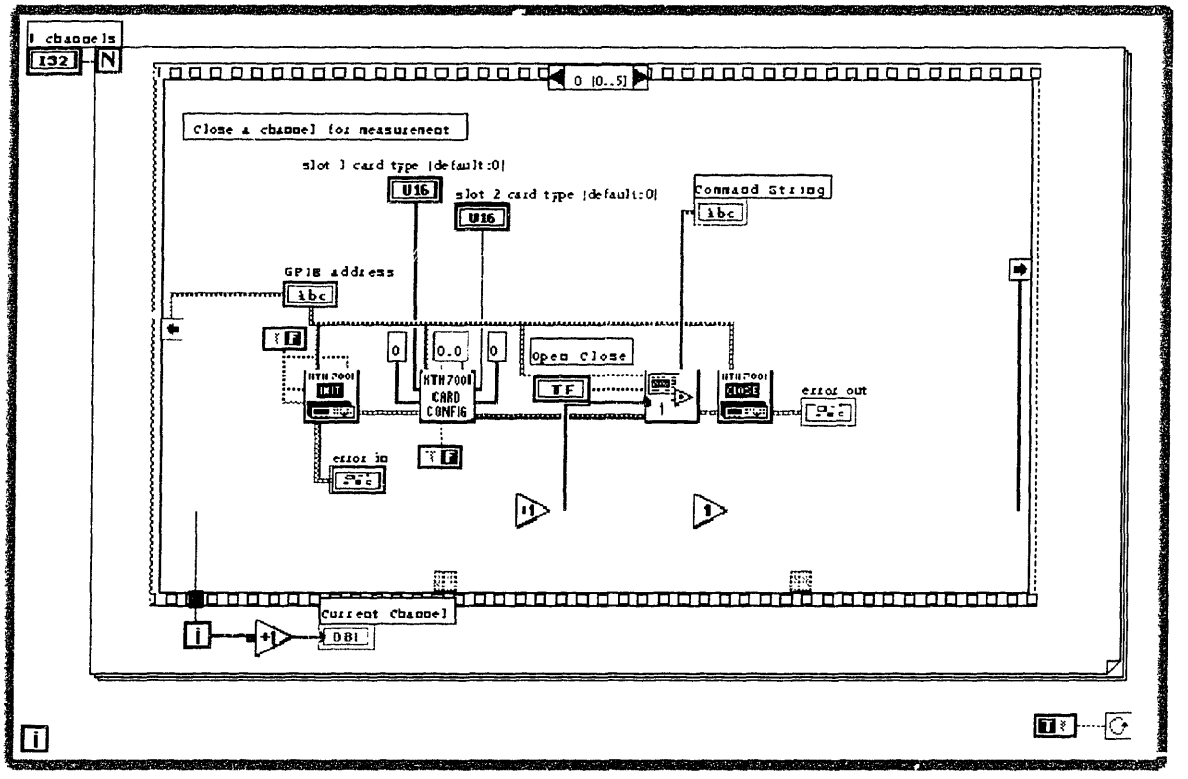

Figure B1: Page 0 of LabVIEW data acquisition virtual instrument (VI)

Figure B1 shows page zero (indicated as 0 [0..5] at the top) of the VI. In this stage of the program, one test model is selected for measurement by closing the switch for a

single test chamber (see Figures 10 and 11). The "KTH7001 Card Config" subVI and other commands for the Keithley 7001 Switch System were obtained from Keithley. The overall loop in which all six portions run can also be seen in Figure B1 as the outermost box..

Figure B2 shows page one (indicated as 1 [0..5] at the top). At this point, the two electrometers are told by LabVIEW to take 5 current readings at equal intervals; the interval time can be set by the user. These readings are displayed but not recorded; the time delay allows currents to settle rather than taking measurements immediately after voltage is applied. Also, the multiple readings allow the user to get a general idea of how quickly the currents are settling. The delay can then be modified to optimize cycling through all nine models. Again, blocks labeled 617 are commands for the Keithley 617 Programmable Electrometer, obtained from Keithley.

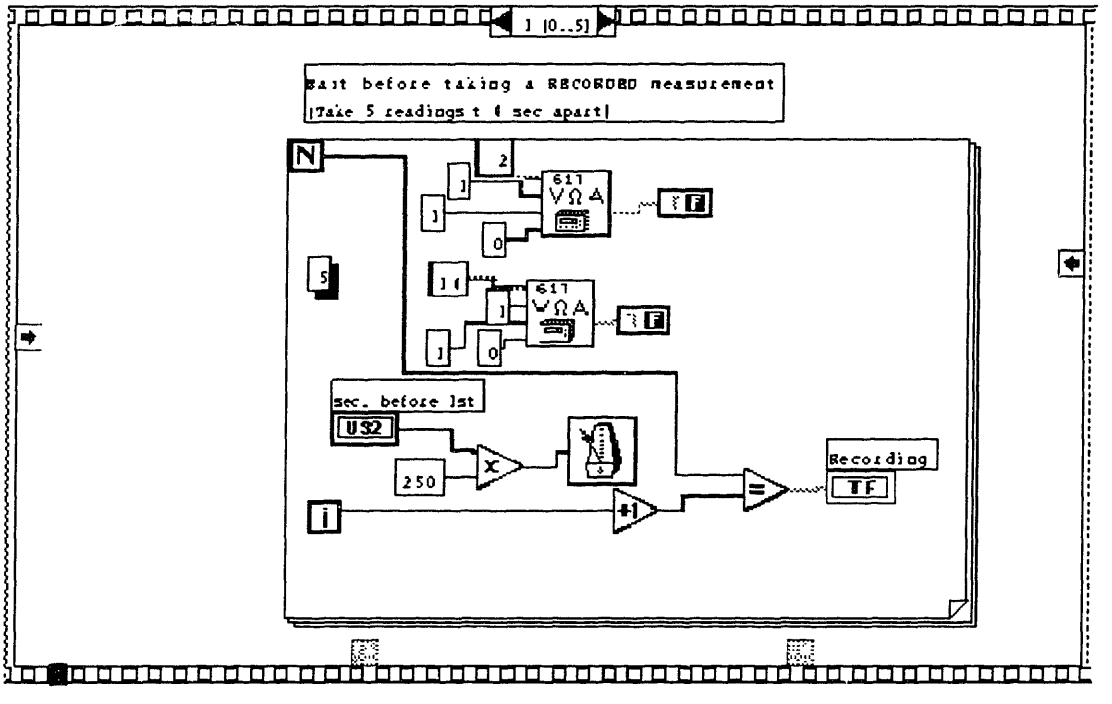

Figure B2: Page 1 of LabVIEW data acquisition virtual instrument (VI)

Page 2 is where actual current measurements are taken. The user can define any number of measurements spaced at any constant interval to be averaged and recorded. For example, during most of the data acquisition for this thesis, ten readings were taken at six

second intervals and then averaged. Measurements occur simultaneously for the two leakage paths of a given test model. Page 2 is shown in Figure B3.

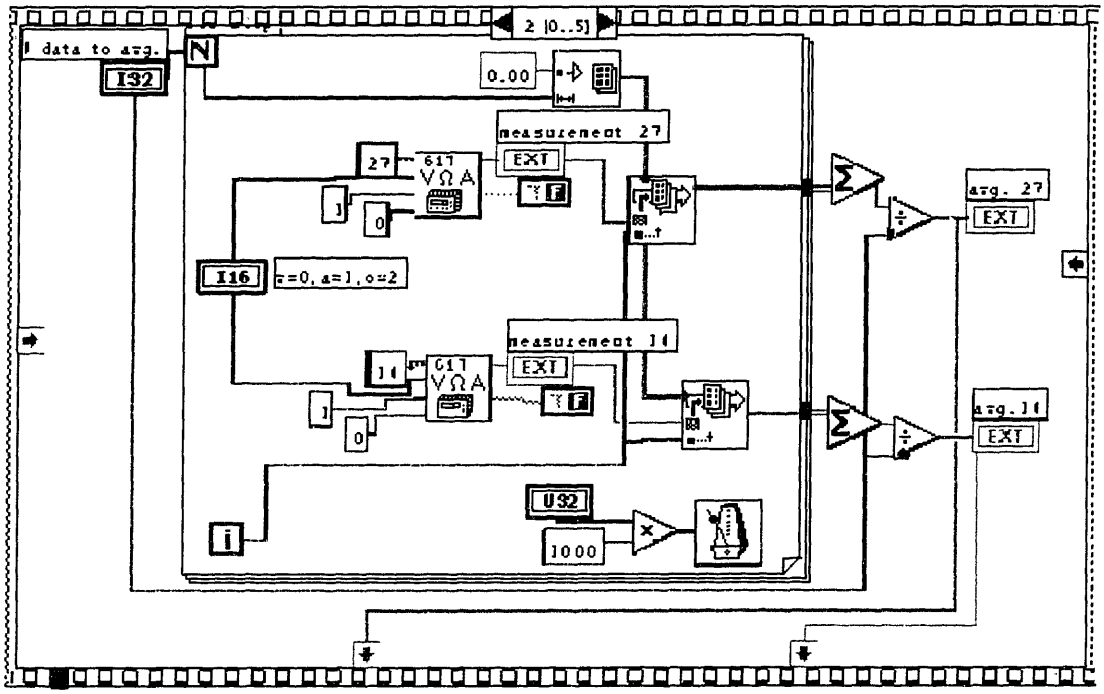

Figure B3: Page 2 of LabVIEW data acquisition virtual instrument (VI)

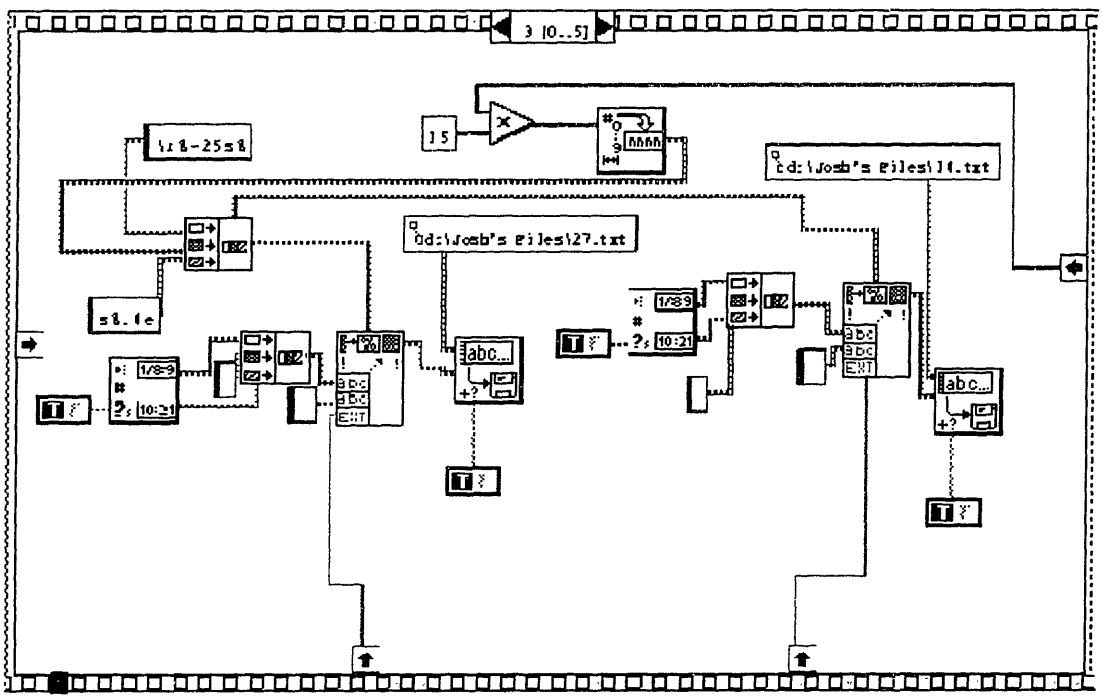

Figure B4: Page 3 of LabVIEW data acquisition virtual instrument (VI)

The averages are sent to the portion of the VI on page 3, shown in Figure B4. They are recorded in two data files, one for each leakage path, along with the exact day and time of the measurement. The data is formatted into columns based on the chamber being tested, making later analysis and plotting a simpler task.

Normally, when one channel of the switch system (corresponding to one test chamber) is selected and closed, the previously selected channels are automatically opened. However, errors do occur, so an extra command to open all channels after testing one model is included on page 4, shown in Figure B5. This simple command prevents recording from more than one test chamber at the same time.

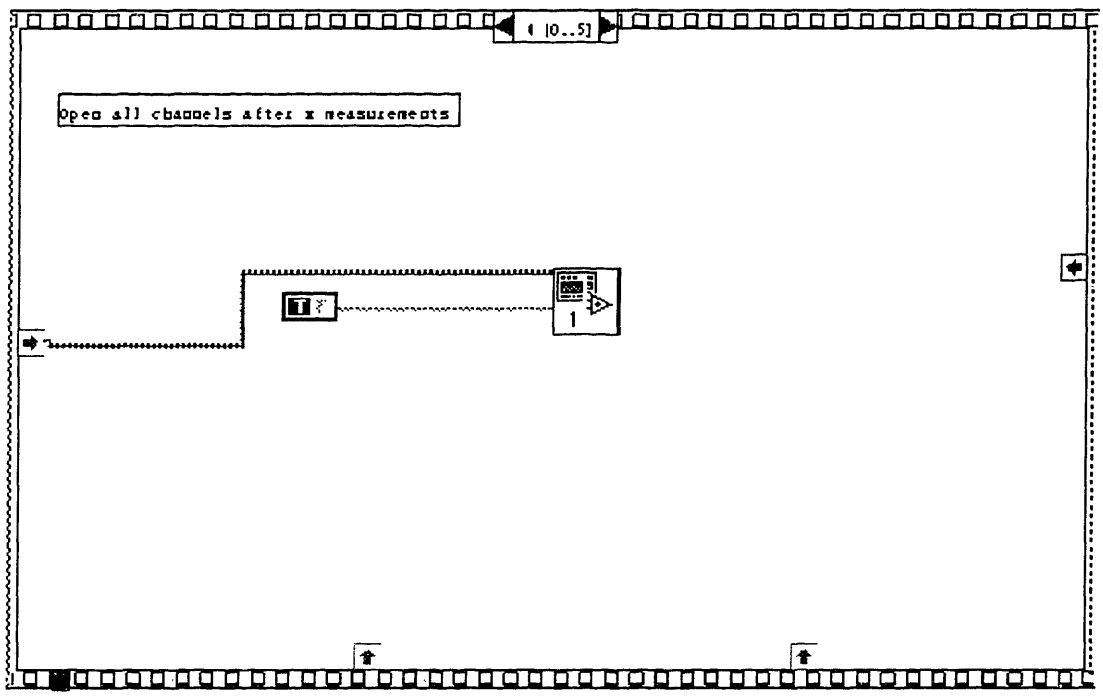

Figure B5: Page 4 of LabVIEW data acquisition virtual instrument (VI)

Figure B6 shows the final page of the VI, which is simply a delay before selecting the next test model for measurement. This delay is also user defined and was typically set to one or two minutes. It allows for more settling time and increases overall stability of the measurements. More importantly, the delay controls the time resolution of the current measurement plots shown in Section 2.3. The goal was to record data at small enough

intervals to observe behavior like the reaction to saline refilling (see Figure 21, bottom), but not so small as to create unmanageably large data files.

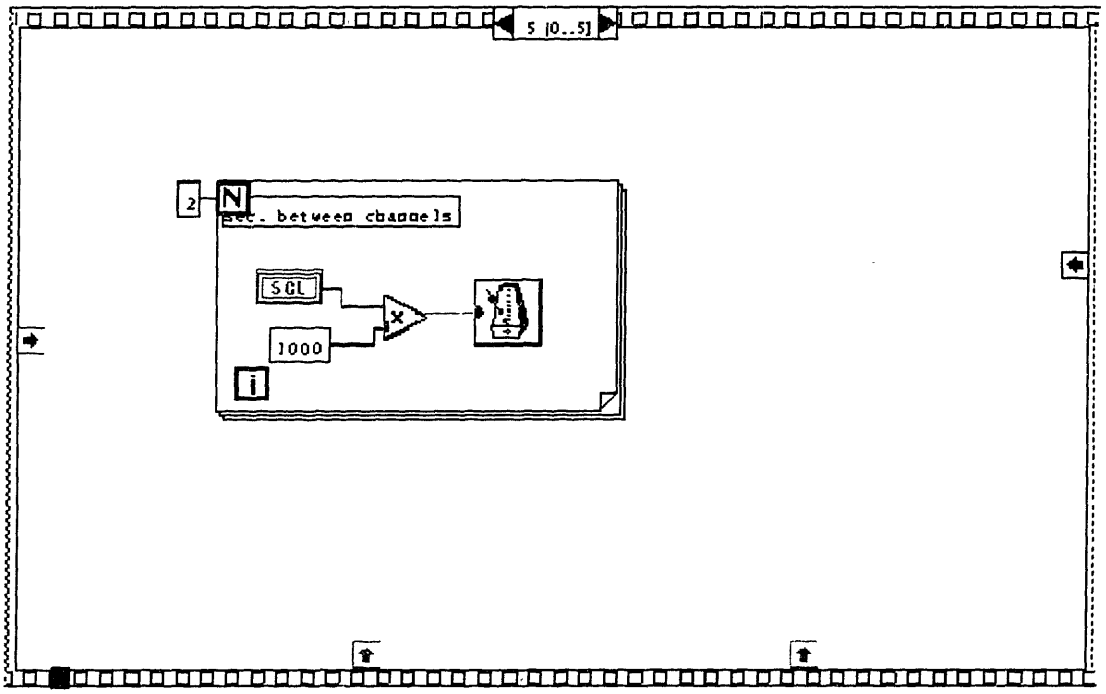

Figure B6: Page 5 of LabVIEW data acquisition virtual instrument (VI)

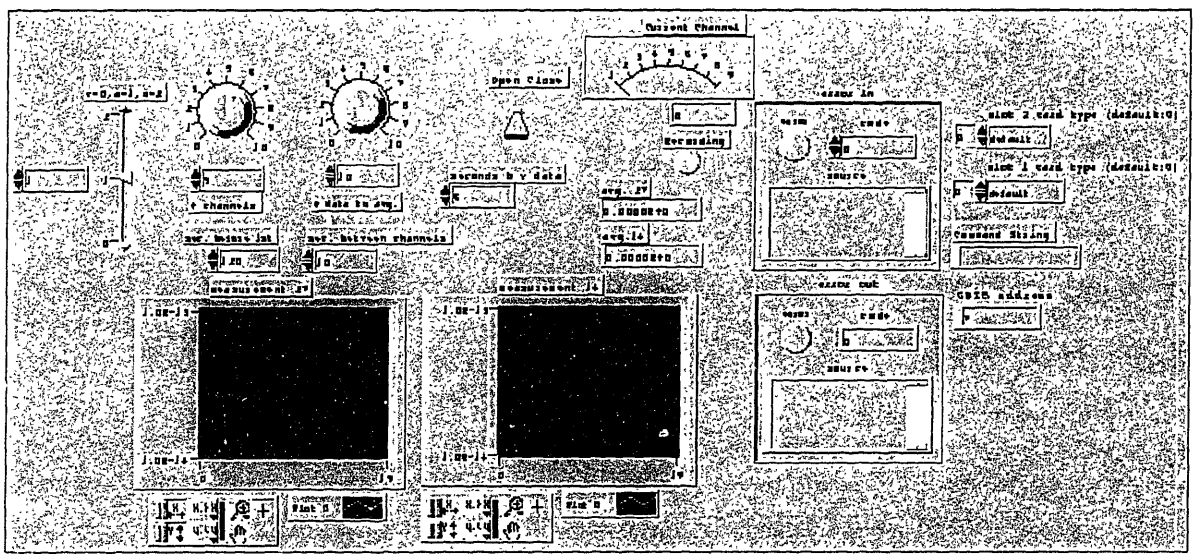

Figure B7: Front panel graphical interface for user control of data acquisition VI

The user controlled variables discussed could all be manipulated from the "front panel" automatically created for the VI by LabVIEW. This graphical interface is shown in Figure B7. The two knobs control on the upper left control the number of test models to measure from and the number of data points to average for each recording. During a test, the two windows show the current readings in a graphical format. Many additional test parameters can also be controlled from this panel.

Appendix C
Mooney-Rivlin Material Model for Rubber Elasticity

In a linear elastic material, the constitutive relationship between stress on the material and the resultant strain is a simple linear function. For illustrative purposes, the elemental case of uniaxial tension is considered:

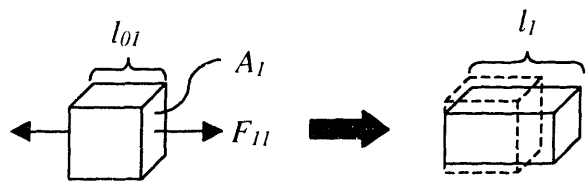

Figure C1: Uniaxial tension of a linear elastic material

$$\sigma_{11} = \frac{F_{11}}{A_1} \tag{C.1}$$

$$\varepsilon_{11} = \frac{l_1 - l_{01}}{l_{01}} \tag{C.2}$$

$$\sigma_{11} = E\varepsilon_{11} \tag{C.3}$$

In equation C.1, σ_{11} represents the stress in the indicated direction on the material, and it is related to the resultant strain ε_{11} by the elastic modulus of the material, E. This relationship is based on the assumptions of both small strain and linear elasticity. Because the strains in rubber elastic materials are typically large and nonlinear, stretch is more often considered. Again, for uniaxial tension:

$$\lambda_1 = \frac{l_1}{l_{01}} \tag{C.4}$$

In equation C.4, λ_1 represents stretch in the indicated direction, defined as the ratio of current length to original length. Since rubber elastic materials are essentially incompressible—total volume does not change when the material is loaded—a relationship between the stretches of the material in all three directions can be easily derived:

$$V_0 = l_{01} l_{02} l_{03} = \text{original volume} \tag{C.5}$$

$$V = l_1 l_2 l_3 = \text{current volume} \tag{C.6}$$

$$V = V_0 \tag{C.7}$$

$$l_1 l_2 l_3 = l_{01} l_{02} l_{03} \tag{C.8}$$

$$\frac{l_1}{l_{01}} \frac{l_2}{l_{02}} \frac{l_3}{l_{03}} = 1 \tag{C.9}$$

$$\lambda_1 \lambda_2 \lambda_3 = 1 \tag{C.10}$$

The principal stretches $(\lambda_1, \lambda_2, \lambda_3)$ can be combined into three quantities which are independent of the both coordinate system and choice of material, known as invariants:

$$I_1 = \lambda_1^2 + \lambda_2^2 + \lambda_3^2 \tag{C.11}$$

$$I_2 = \lambda_1^2 \lambda_2^2 + \lambda_1^2 \lambda_3^2 + \lambda_2^2 \lambda_3^2 \tag{C.12}$$

$$I_3 = \lambda_1^2 \lambda_2^2 \lambda_3^2 \tag{C.13}$$

The complex stress-stretch relationship for a rubber elastic material is typically given in terms of strain energy function rather than the simple linear function shown in equation C.3. Strain energy is a measure of the potential energy stored in a body by virtue of its elastic deformation. Therefore, strain energy can also be considered the amount of work that must be done to produce this deformation, consisting of both normal and shear strains, and will be designated *W*. For uniaxial tension of a linear elastic material (see Figure C1), strain energy is simply the area under the stress-strain curve, shown in Figure C2.

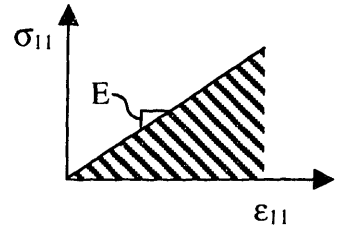

Figure C2: Illustration of strain energy for uniaxial tension of a linear elastic material

In addition to this pictorial calculation, the strain energy can also be easily calculated directly from any of the second order tensors (stress, strain, stretch) as long as a constitutive relationship, such as elastic modulus (E), is known:

$$W = \int \sigma_{11} d\varepsilon_{11} \tag{C.14}$$

$$W = \int E\varepsilon_{11} d\varepsilon_{11} \tag{C.15}$$

$$W = \frac{1}{2} E\varepsilon_{11}^2 \tag{C.16}$$

In equations C.14 through C.16, strain energy for the linear elastic material under uniaxial tension was calculated based on strain: $W = f(\varepsilon_{11})$. The strain energy function for a rubber elastic material is typically based on stretch or stretch invariants: $W = f(\lambda_1, \lambda_2, \lambda_3)$ or $W = f(I_1, I_2, I_3)$. Based on equation C.10, it can be easily shown that for incompressible solids, such as rubber elastic materials, $I_3 = 1$. Therefore, the complex constitutive relationships between the strain energy and the two remaining invariants are necessary. A general form for W based on I_1 and I_2 consists of a doubly infinite power series:

$$W = \sum_{m=0,n=0}^{\infty} C_{mn} (I_1 - 3)^m (I_2 - 3)^n \tag{C.17}$$

In equation C.17, C_{00} is defined as zero. It should also be noted that when $\lambda_1 = \lambda_2 = \lambda_3 = 1$, $I_1 = 3$ and $I_2 = 3$. Equation C.17 therefore becomes $W = 0$, logically corresponding to no stretching and thus no strain energy.

The stress-stretch behavior of a rubber elastic material can be modeled by experimentally determining the constants (C_{mn}) in equation C.17. The Mooney-Rivlin relationship for strain energy is based on the first two constants, with all other constants set to zero:

$$W = C_{10}(I_1 - 3) + C_{01}(I_2 - 3) \tag{C.18}$$

However, the Mooney-Rivlin material definition can be generalized to a higher order model in ADINA, using up to the first nine constants of equation C.17:

$$\begin{aligned} C_{10} &\equiv C_1 \\ C_{01} &\equiv C_2 \\ C_{20} &\equiv C_3 \\ C_{11} &\equiv C_4 \\ C_{02} &\equiv C_5 \\ C_{30} &\equiv C_6 \\ C_{21} &\equiv C_7 \\ C_{12} &\equiv C_8 \\ C_{03} &\equiv C_9 \end{aligned} \tag{C.19}$$

As discussed in Section 3.3, the first seven constants for the rubber of interest were derived by Z. Guoxing and W. Shoumei. Therefore, the strain energy function was entered into the finite element program as equation C.20:

$$\begin{aligned} W = {} & 0.330531(I_1 - 3) + 0.006516(I_2 - 3) - 0.06707375(I_1 - 3)^2 + \\ & 0.02860645(I_1 - 3)(I_2 - 3) - 0.0159820625(I_2 - 3)^2 - \\ & 0.000697375(I_1 - 3)^3 + 0.003609875(I_1 - 3)^2(I_2 - 3) \end{aligned} \tag{C.20}$$

All constants in equation C.20 are in units of N/mm^2. Other material parameters entered were density (1.12 g/cm^3) and bulk modulus, which is the ratio of average normal stress to

volumetric strain. Bulk modulus was chosen to be consistent with a nearly incompressible material ($\nu = 0.499$):

$$\kappa = \frac{2G(1+\nu)}{3(1-2\nu)} = \frac{2G(1.499)}{3(1-.998)} \cong 500G \tag{C.21}$$

In equation C.21, G equals the small strain shear modulus, which can be estimated from the Mooney-Rivlin constants:

$$G = 2(C_1 + C_2) \tag{C.22}$$

$$\kappa = 1000(C_1 + C_2) = 0.337047 \text{ GPa} \tag{C.23}$$

The majority of the material presented in Appendix C was taken from the lecture notes from Course 2.305 at MIT, with a brief reference to one publication on the subject by R. Rivlin [33, 34]. Equations C.21 and C.22, as well as the proper use of equation C.17 in ADINA, were taken from documentation for the software [35].

THESIS PROCESSING SLIP

FIXED FIELD: ill. _____ name _____

index _____ biblio _____

► COPIES: (Archives) Aero Dewey (Eng) Hum

Lindgren Music Rotch Science

TITLE VARIES: ► ☐ _____

NAME VARIES: ► ☑ David.

IMPRINT: (COPYRIGHT) _____

► COLLATION: 113 p

► ADD: DEGREE: _____ ► DEPT.: _____

SUPERVISORS: _____

NOTES:

cat'r: date:

page:

► DEPT: M.E. ► J140

► YEAR: 1999 ► DEGREE: S.M.

► NAME: MOSS, Joshua D.